ABSTRACT

Title of dissertation: DISORDERED GAUGE FIELDS WITH ATOMIC BOSE GASES

Alina M. Piñeiro Escalera
Doctor of Philosophy, 2025

Dissertation directed by: Dr. Ian Spielman
Department of Physics.
University of Maryland, College Park,
Joint Quantum Institute, and
National Institute of Standards and Technology

This thesis highlights the versatility of ultracold atoms as quantum simulators by utilizing Bose gases and engineered light-induced Hamiltonians to investigate quantum phenomena across multiple areas of physics. As a high-energy simulator, an analog experiment simulating particle–antiparticle pair creation from the quantum vacuum, emulated these strong-field effects at energy scales accessible in the laboratory. The Dirac picture of particle-antiparticle vacuum and the concept of optical lattice band theory was the foundation of our approach. In this framework, we readily measured pair creation and demonstrated that this high-field phenomenon is well-characterized by Landau-Zener tunneling. Within condensed matter physics, ultracold atoms were employed to study topological dynamics of periodically driven Floquet systems. Using a Floquet "switching" protocol in a one-dimensional bipartite magnetic lattice, we realized a periodically driven Su–Schrieffer–Heeger model that maps onto a massless Dirac Hamiltonian. By alternating between two lat-

tice configurations with near-optimal timing, we observed spin–momentum–locked transport characterized by well-defined drift velocities and with spatial displacement linearly increasing over many Floquet periods, establishing a platform for exploring topological band dynamics.

The culminating focus of this thesis is localization physics in ^{87}Rb Bose-Einstein condensates subjected to disordered artificial gauge fields over a range of energy and time scales, in both equilibrium and out-of-equilibrium settings. The effective Hamiltonian was implemented by driving two-photon Raman transitions with laser fields, while disordered vector potential landscapes were independently generated using tunable intensity patterns projected by a digital micromirror device (DMD). By varying the experimental protocols—including the turn on times of the Raman coupling and disorder, as well as the disorder strength—we obtained insight into quantum dynamics in the presence of disordered gauge fields. The resulting dynamics revealed rich behavior: including spatially inhomogeneous magnetization for high-energy dynamics and increases in the condensate width after time-of-flight for pulsed disorder in lower energy and near-equilibrium conditions; lastly, signatures of localization, in the form of damped oscillations, were observed as the system was driven out-of-equilibrium.

Disordered Gauge Fields with Atomic Bose Gases

by

Alina M. Piñeiro Escalera

Dissertation submitted to the Faculty of the Graduate School of the
University of Maryland, College Park in partial fulfillment
of the requirements for the degree of
Doctor of Philosophy
2025

Advisory Committee:
Professor Steven Rolston, Chair
Professor Ian Spielman, Advisor, Co-Chair
Professor Yu Liu
Professor Justyna Zwolak
Professor Edo Waks, Dean's Representative

© Alina M. Piñeiro Escalera, 2025

For Cyrus and Lucas.

Lucas and Cyrus,

with equal dedication,

and to J.G.!

Table of Contents

1 Introduction 1
1.1 Thesis Overview . . . 4

2 Rubidium-87: From One Atom to Many 12
2.1 Electronic Structure of Rubidium . . . 12
2.2 Interaction with Magnetic Fields . . . 15
2.3 Coherent Manipulation . . . 18
2.4 Near-Resonant Light-Atom Interactions . . . 20
2.5 Quantum Gases . . . 22
2.5.1 Identical Particles and Exchange Symmetry . . . 23
2.6 Bose-Einstein Condensation . . . 24
2.6.1 Ideal Gas . . . 25
2.6.2 Temperature . . . 28
2.6.3 Estimating Temperature Using Maxwell-Boltzmann . . . 29
2.7 Scattering in Ultracold Bosonic Gases . . . 30
2.7.1 s-Wave Scattering of Identical Bosons . . . 31
2.7.2 Scattering Between Different Internal States . . . 33
2.8 Gross-Pitaevskii Equation . . . 34
2.8.1 Thomas–Fermi Approximation for BECs in a Harmonic Trap . 36
2.9 Numerical Simulations of GPE . . . 38
2.9.1 Vector Potentials & Gauge Criterion - Symmetric to Landau . 40
2.9.2 Verification of Hermiticity . . . 44
2.9.3 Total Energy & Conservation of Energy Test . . . 46

3 Experimental Setup and Measurement Techniques 49
3.1 Towards Quantum Degeneracy . . . 50
3.2 Bose–Einstein Condensate Production . . . 52
3.2.1 Evaporation and State Transfer . . . 54
3.2.2 Trapping in the Presence of Gravity and Magnetic Gradients . 55
3.3 Experiment Overview . . . 60
3.3.1 Control System . . . 63
3.4 Laser Systems . . . 64
3.5 Magnetic Field Systems . . . 66
3.5.1 Magnetic Field Stabilization and Calibration . . . 68
3.5.2 RF Signal Generation . . . 70
3.6 Raman Optical System . . . 70
3.7 Imaging Systems . . . 73

3.7.1 XY Imaging Systems . . . 74
3.7.2 XZ Imaging System . . . 77
3.8 Digital Micromirror Device System . . . 78
3.9 TEM_{01} System – Aka: Sheet Trap . . . 82
3.9.1 Anti-Trapping From Zero-Point Energy . . . 85
3.9.2 Optical System . . . 87
3.9.3 Performance . . . 88
3.10 Measurement . . . 90
3.10.1 Absorption Imaging with Doppler Correction . . . 91
3.10.2 Partial-Transfer Absorption Imaging . . . 92

4 Ultracold Atoms in Optical Lattice Potentials 94
4.1 Optical Lattice Potentials . . . 94
4.2 Single Particle Hamiltonian . . . 95
4.2.1 Bloch Bands . . . 99
4.2.2 Wannier Functions . . . 101
4.3 Hellmann-Feynman Theorem . . . 102
4.4 Experimental Characterization of Bose-Einstein Condensates in a Periodic Lattice Potential . . . 103
4.4.1 Adiabatic Loading of a BEC into a Lattice Potential . . . 104
4.4.2 Lattice Alignment . . . 105
4.4.3 Lattice Depth Calibrations . . . 106
4.4.4 Mapping Crystal Momentum to Free Particle Momentum . . . 107
4.4.5 Bloch Oscillations & Landau-Zener Tunneling . . . 108
4.5 Conclusions and Outlook . . . 109

5 Sauter-Schwinger Effect with Bose-Einstein Condensates 110
5.1 1d Dirac Hamiltonian . . . 112
5.2 Atomic System: 1d Optical Lattice Model . . . 113
5.2.1 Bare Eigen-Energies and the Free Particle . . . 114
5.3 Landau-Zener Diabatic Transition Probability . . . 116
5.4 Relation Between Force & Γ Parameter . . . 117
5.4.1 Critical Force from Schwinger's Limit . . . 118
5.5 Experimental Characterization . . . 120
5.5.1 Emulated Electric Forces . . . 122
5.6 Pair Creation From a Single Occupied State . . . 123
5.7 Uniformly Filled Quantum Electrodynamic Vacuum . . . 126
5.8 Conclusion and Outlook . . . 128

6 Floquet Engineering 130
6.1 1d Bipartite Magnetic Lattice . . . 130
6.1.1 Corresponding Adiabatic Potential . . . 134
6.1.2 Magnetizations . . . 135
6.2 Experimental Characterization . . . 136
6.3 Dirac Floquet . . . 140

6.4 Conclusions and Outlook . . . 142

7 Induction of Artificial Gauge Fields 143
7.1 Effective Single-Particle Hamiltonian with Artificial Gauge Field . . . 144
7.2 New Dog, Old Tricks: DMD Generated Optical Fields . . . 151
7.2.1 Experimental Characterization . . . 151
7.2.2 Uniform Vector Potential . . . 154
7.2.3 Vortex-Nucleation Transition in BECs . . . 155
7.2.3.1 Critical Cyclotron Frequency . . . 156
7.2.3.2 Flux Quanta in a BEC . . . 157
7.2.3.3 Shearing Parameter . . . 159
7.3 Conclusions and Outlook . . . 161

8 Disordered Gauge Fields with Bose Gases 162
8.1 Effective Hamiltonian for Disordered Gauge Fields . . . 163
8.2 Experimental Characterization . . . 165
8.3 Signatures of Synthetic Disordered Gauge Fields . . . 169
8.3.1 High-Energy, Out-Of-Equilibrium . . . 170
8.3.2 Low-Energy, Near Equilibrium . . . 172
8.3.3 Low-Energy, Driving System Out-Of-Equilibrium . . . 177
8.4 Conclusions and Outlook . . . 179

9 Conclusion and Outlook 181

Bibliography 182

Chapter 1: Introduction

Quantum simulation is a powerful approach for studying complex quantum physics, by utilizing the behavior of one system to model, and thereby understand, features of another–otherwise inaccessible–system. Ultracold atomic gases as *quantum simulators* have become a central platform for engineering analog quantum systems in experimentally accessible environments. These ultracold atomic systems have helped address long-standing questions in physics, including quantum phase transitions, strongly interacting bosons and fermions [1], and extreme systems such as quark-gluon plasmas and neutron stars [2]. They have also revealed unexpected dynamical phenomena in quantum many-body systems that do not follow conventional thermodynamic laws [3], and made it possible to realize systems without natural analogs, such as synthetic dimensions [4,5]. Because many of these systems are beyond the reach of exact classical computer simulation, quantum simulators are considered a form of computational "quantum advantage."

Quantum simulators are classified in a range of platforms [6]. At one end are *special-purpose analog simulators*, designed to realize a specific Hamiltonian with high precision but little flexibility. In the middle of this spectrum are *tunable analog simulators*, which allow control over parameters such as geometry, dimensionality, and interaction strength [7], enabling study of a broader variety of models. At the most flexible end are *hybrid architectures*, that combine analog dynamics with dig-

itally programmable controls [8], extending the accessible Hamiltonians [9–11] and moving toward the universality of digital quantum computation [12].

Although all atoms consist of fundamental fermionic particles, their overall quantum statistics—that is, how they populate quantum states—are determined by their total intrinsic spin [13–16]. Fermions obey the Pauli exclusion principle, which forbids multiple occupancy of the same quantum state, whereas bosons can share a state without restriction. As a result, neutral atoms can behave as either composite fermions or composite bosons. The combination of bosonic statistics, laser cooling and trapping [17, 18], and evaporative cooling [19, 20] made it possible to produce a Bose–Einstein condensate [21, 22], in which all constituent particles share a single quantum state, forming a coherent matter wave with a well-defined global phase. Shortly thereafter, experiments succeeded in cooling fermionic atoms to reach quantum degeneracy [23–26]. These breakthroughs established the foundation for employing ultracold atomic gases as quantum simulators.

Ultracold atomic gases span from *special-purpose analog simulators* to *tunable analog simulators*. Their advantages include engineering single-particle Hamiltonians and artificial gauge fields to controlling interparticle interactions, the ability to resolve and address single atoms [27] and recently, the control of generated intensity fields as potentials via digital mirrored devices (DMD) [28–30].

This thesis highlights the versatility of ultracold atoms as quantum simulators, focusing on Bose gases and the engineering of light-induced Hamiltonians to investigate quantum phenomena across multiple areas of physics. At high energies, we realized an analog simulation of the Sauter-Schwinger effect [31–35] that predicts

the creation of particle-antiparticle pairs from the quantum vacuum via tunneling when a large electric field is present. These strong-field effects were emulated at energy scales accessible in the laboratory. The Dirac picture of particle-antiparticle vacuum and the concept of optical lattice band theory was the foundation of our approach. In this framework, we readily measured pair creation and demonstrated that this high-field phenomenon is well-characterized by Landau-Zener tunneling.

Within condensed matter physics, ultracold atoms were used to explore topological dynamics of periodically driven Floquet systems. By implementing a Floquet "switching" protocol in a 1d bipartite magnetic lattice, a periodically driven Su–Schrieffer–Heeger model was realized that maps onto a massless Dirac Hamiltonian. By alternating between two lattice configurations with near-optimal timing, we demonstrated spin-momentum-locked transport with well-defined drift velocities and with spatial displacement linearly increasing over many Floquet periods. Our measurements of magnetization, group velocity, and atomic displacement were in good agreement with numerical modeling, while also revealing small deviations from the ideal SSH limit due to finite ramp times, residual tunneling during switching, and weak additional lattice potentials.

The culminating focus of this work, however, is the study of localization physics in ^{87}Rb Bose–Einstein condensates subjected to disordered gauge fields, across a range of energy and time scales, in both equilibrium and out-of-equilibrium regimes. The simulated effective Hamiltonian was implemented by driving two-photon Raman transitions with laser fields, combined with tunable intensity patterns from a digital micromirror device (DMD) that generated disordered vector potential landscapes.

By varying the turn-on protocols—including the timescales for applying the Raman coupling and disorder, as well as the disorder strength—we obtained insight into quantum dynamics in the presence of disordered gauge fields. The resulting dynamics revealed rich behavior: including spatially inhomogeneous magnetization for high-energy dynamics and increases in the condensate width after time-of-flight for pulsed disorder in lower energy and near-equilibrium conditions; lastly, signatures of localization, in the form of damped oscillations, were observed as the system was driven out-of-equilibrium.

1.1 Thesis Overview

This thesis presents relevant physics background, experimental control and measurement techniques, an overview of the RbK experimental apparatus, and experimental results, along with new methods developed in our laboratory for engineering disordered gauge fields to study localization physics.

Chapter 2 introduces fundamental concepts from atomic physics that are essential for understanding ultracold ^{8}7Rb systems and the work presented throughout this thesis, from internal state structure and atom–light interactions to quantum statistics and Bose–Einstein condensation. It concludes with an introduction to the Gross–Pitaevskii equation and numerical simulations relevant to artificial gauge field experiments. My contributions include writing all of the code for the concepts and simulations, with guidance from I. Spielman for the simulation work.

Chapter 3 provides an overview of the experimental apparatus, experimental tech-

niques and describes the relevant modifications and upgrades to the apparatus. This includes the LuxBeam DMD and sheet trap details, implementations, and xy imaging system modification. It concludes with a discussion of the imaging systems that form the foundation of all measurement techniques used in this work. My contributions entail completing 3 experimental upgrades: 1) Modifying the xy imaging system, with assistance from E. Mercado Gutierrez in measuring magnification and installing the new Zaber translation stage for the xy0 in situ path. I wrote the experimental control scripts, collected the imaging system characterization data, and wrote the associated data analysis scripts by following developed methods to plot power spectral densities utilizing principal component analysis. 2) The design and implementation of the LuxBeam DMD system and the first versions of the disorder functions. G. Reid contributed by completing all the work necessary to purchase the DMD and wrote the initial communication code. E. Mercado Gutierrez assisted with implementation—particularly in resolving issues with the dichroic optics, triggering via computer controls, associated code and the LuxBeam DMD optical system schematic. E. Gvozdiovas contributed to the development of new and improved versions of the disorder functions and the recent implementation with labscript. 3) The design and implementation of the TEM_{01} System, aka: Sheet Trap. Credit for the first bench version of the sheet trap and phase plate production goes to M. Beeler. In order to implement the sheet trap on the experimental apparatus, I redesigned the optical setup, and completed a number of modifications to officially trap atoms. I am grateful for contributions from E. Mercado Gutierrez that led to the sheet trap characterization, finding the maximum trapping potential,

and helping with trapping atoms in the sheet trap plus box potential. I wrote all of the applicable code and completed all of the calculations. In addition, I also replaced and modified the Verdi mirrors in the Ti:Sapphire laser system, including re-coupling the sapphire crystal and restoring lasing. A necessary repair that had been causing issues with power stability at an alarming rate. Once the laser reached operating power suitable for experiments, additional improvements were made by E. Mercado Gutierrez, who consistently managed to extract a bit more power from the system. While the original LightCrafter DMD system was initially set up by A. Fritsch, the system was later completely rebuilt through joint efforts between E. Mercado Gutierrez and myself. This system was used to generate the box potential and potentials for soliton experiments. Over the course of my time in the RbK lab, many people have contributed to maintaining and upgrading the apparatus. Credit goes to the following team for getting the experiment operating and running Labscript: M. Lu, D. Genkina, A. Pineiro, G. Reid and C. Billington – with guidance and support from I. Spielman. In the past 3 years, numerous systems and hardware components required repairs, replacements, or modifications. These efforts were carried out primarily by E. Mercado Gutierrez and myself, with additional contributions from E. Gvozdiovas.

Chapter 4 provides a theoretical and experimental overview of ultracold atoms in optical lattice potentials. It begins by introducing the single-particle physics of atoms in a one-dimensional periodic potential, where interference of counter-propagating laser beams gives rise to a tunable lattice structure and associated energy bands described by Bloch's theorem. The emergence of Bloch and Wannier states, band

dispersion, and group velocity are examined, with particular emphasis on the use of the Hellmann–Feynman theorem to relate the lattice band slope to atomic motion. The chapter then transitions to experimental realizations, detailing the adiabatic loading of a Bose–Einstein condensate into an optical lattice, alignment and calibration procedures, and methods for mapping crystal momentum to free-particle momentum. Together, these discussions establish the foundation for understanding lattice-based simulations of relativistic field phenomena presented in the following chapter. My contributions encompass all aspects of this chapter, including the theoretical overview, single-particle simulations, and all associated experimental work. Chapter 5 This chapter presents an experiment utilizing BECs to quantum simulate the Sauter-Schwinger effect–the creation of particle-antiparticle pairs from the quantum vacuum when a large electric field is present. Additionally, this chapter is a reprint of my previous work published in Ref. [36] with additional material. This chapter covers the mapping of an approximated 1d optical lattice Hamiltonian at the edge of the Brilloiun zone to the 1d Dirac Hamiltonian describing relativistic particles. We present experiments showing that particle-antiparticle creation in an analog cold atom systen can be understood as a quantum tunneling process. My contributions include experimental sequence writing and implementation, all data collection and all analysis. Experiment ideas and guidance are credited to I. Spielman. I am grateful for contributions made by D. Genkina which include getting the displaced ODT protocol set up for the emulated electric force, overall guidance and help with the project. I am also grateful for contributions made by M. Lu which include assistance with the alignment of the 1064 nm optical lattice retro-reflected

laser beam.

Chapter 6 explores Floquet engineering in a 1d bipartite magnetic lattice, providing the theoretical background and experimental realization to study controlled, time-periodic dynamics. The chapter outlines some of the published work presented in [37] and begins by describing the Raman–rf lattice Hamiltonian and the resulting adiabatic potentials that form a bipartite structure with spin-textured sublattice sites. The chapter presents the mapping of this Raman–rf Hamiltonian system onto a driven Su–Schrieffer–Heeger (SSH) model, the implementation of a Floquet "switching" protocol, and the observation of spin-momentum-locked transport corresponding to a massless Dirac Hamiltonian. This experiment was led M. Wu with guidance from I. Spielman and contributions were made by G. Reid and A. Fritsch. My direct contributions include identifying a major issue plaguing the experiment, i.e. an optical lattice forming by the ODT 1064 nm laser light retro-reflecting off of the viewport on the experimental vacuum chamber. This led to modifications and hence the experiment was able to continue. I also contributed to making a circuit for the DDS to improve trigger timing limitations, data collection, and paper writing. In addition, all relevant physics background and code was written by me with little guidance.

Chapter 7 focuses on the induction of artificial gauge fields and builds on previous work. The goal of this chapter is to provide the relevant physics background pertaining to artificial gauge fields and to demonstrate that we successfully implemented a protocol of light-induced artificial gauge fields generated via a DMD. We reproduce previous work and present data showing vortex nucleation in BECs. My

contributions entail leading the project–this includes the force behind completing the necessary modifications to the experimental apparatus–xy imaging system modification and designing and implementing the LuxBeam DMD (these contributions were discussed in Chapter 3), crucial DMD alignment, improving the Raman laser system, writing all experimental sequence code and collecting all of the data. In addition, all analysis and simulation code was completed by me unless otherwise indicated. This was all completed with guidance from I. Spielman. I am grateful for contributions made by E. Gvozdiovas, his contributions include writing various analysis code-the sheared TF profile fit, pupil function generation and simulation code, DMD functions–specifically for the gradient function, and plot generation–Fig.7.7 specifically. I am also grateful for contributions made by E. Mercado Gutierrez, which include always helping with issues in lab, whatever they may be and which occur often! In addition, his contribution with helping implement the DMD trigger and other contributions here and there that added up and helped with moving the project forward.

Chapter 8 investigates localization phenomena in BECs subjected to artificial gauge fields and controlled disorder, exploring both equilibrium and out-of-equilibrium regimes across a range of energy and time scales. Our studies begin in the high-energy, instantaneous limit, regime—where the Hamiltonian is suddenly changed—and then transition to the low-energy regime, achieved by various versions of adiabatically loading. In the high-energy regime, atoms prepared in the magnetically insensitive $|f = 1, m_f = 0\rangle$ state were suddenly exposed to Raman coupling, producing a superposition of $|f = 1, m_f = 0, \pm 1\rangle$ states in the presence of disorder.

The subsequent unitary evolution revealed shot-to-shot statistical variations in the spin-state populations, highlighting the role of disorder-induced fluctuations. In the low-energy regime, where the Raman coupling was adiabatically applied, the dressed states followed the ground-state dispersion $E(k_x)$, enabling controlled studies of the system's response in the presence of disorder for two experiments: (1) near equilibrium, where disorder was ramped on over 3 ms and condensate width was measured as a function of hold time, and (2) in a driven, out-of-equilibrium regime, where disorder was introduced over 40 ms and dipole oscillations were induced. In this regime, we present the damping rate and frequency dependence on disorder strength. We observe an increase in the damping rate with increased disorder strength and also observe that the frequency deviates from a damped harmonic oscillator. We illustrate the different energy regimes and their corresponding experimental timing diagrams and demonstrate that by varying the loading protocols—including the timescales for applying the Raman coupling and disorder, as well as the disorder strength—we gain insight into how artificial gauge fields behave in the presence of disorder. My contributions entail leading the project–this includes writing all experimental sequence code, collecting all of the data, analysis code and numerous calibrations. I. Spielman proposed the project and I am grateful for his guidance, problem-sovling, attention to detail, and unwavering support throughout this project. I am grateful for contributions made by E. Gvozdiovas, his contributions include writing various analysis code–that helped tremendously and allowed me to focus on experimental progress and data collection–DMD and imaging system modeling (includes Fig. 8.1c), Monte Carlo simulations and generation of Fig. 8.4,

DMD functions–specifically new improved disorder functions and others for future data collection, calibration help and for being interested and present during my project. I am also grateful for contributions made by E. Mercado Gutierrez, which include initial help with VLS calibrations, alignment and tuning contributions.

Publications

The following articles have been published or drafted during the context of this thesis. The articls most relevant for this thesis are marked in bold font.

- A. M. Piñeiro, E. Gvozdiovas, E.D. Mercado-Gutierrez, I.B. Spielman, ***Disordered gauge fields with Bose gases***, (Anticipated submission 2026)
- E.D. Mercado-Gutierrez, E. Gvozdiovas, A. M. Piñeiro, I.B. Spielman, *Near-perfect absorption in a non-Hermitian synthetic lattice*, (Anticipated submission 2026)
- E. Gvozdiovas, A. M. Piñeiro, E.D. Mercado-Gutierrez, I.B. Spielman, *In situ magnetic-field stabilization for quantum-gas experiments*, (Anticipated submission 2026)
- A.R. Fritsch, A. M. Piñeiro, E.D. Mercado-Gutierrez, G.H. Reid, I.B. Spielman, *Dynamics of solitonic vortices, velocities, and disorder*, (Anticipated submission 2026)
- G.H. Reid, M. Lu, A.R. Fritsch, A. M. Piñeiro, I.B. Spielman, *Dynamically Induced Symmetry Breaking and Out-of-Equilibrium Topology in a 1D Quantum System*, Physical Review Letters 129 (12), 123202 (2022)
- M. Lu, G.H. Reid, A.R. Fritsch, A. M. Piñeiro, I.B. Spielman, ***Floquet Engineering Topological Dirac Bands***, Physical Review Letters 129, 040402 (2022)
- A.R. Fritsch, M. Lu, G.H. Reid, A. M. Piñeiro, I.B. Spielman, *Creating solitons with controllable and near-zero velocity in Bose-Einstein condensates*, Physical Review A 101 (5), 053629 (2020)
- A. M. Piñeiro, D. Genkina, M. Lu, I.B. Spielman, ***Sauter-Schwinger effect with a quantum gas***, New Journal of Physics 21 (8), 083035 (2019)
- D. Genkina, L.M. Aycock, H. Lu, A. M. Piñeiro, M. Lu, I.B. Spielman, *Imaging topology of Hofstadter Ribbons*, New Journal of Physics 21 (5), 053021 (2019)

Chapter 2: Rubidium-87: From One Atom to Many

This chapter introduces foundational concepts from atomic physics essential for understanding the experiments presented in this thesis. It begins with the electronic structure of Rubidium-87, which defines the internal state space used throughout. The interaction of atoms with external magnetic fields is then discussed, followed by coherent control through Rabi oscillations and near-resonant light–matter interactions, which enable precise state manipulation and imaging. Core ideas from quantum statistics are reviewed, including the behavior of degenerate gases, indistinguishability of particles, and exchange symmetry—providing a natural lead-in to Bose–Einstein condensation. Estimating the temperature of ultracold atomic clouds and the role of scattering in bosonic systems are also discussed. The chapter concludes with a brief overview of the Gross–Pitaevskii equation and a numerical simulation that illustrates its application, along with theoretical elements relevant to the artificial gauge fields, a central focus of this work. These concepts, together with laser cooling and trapping methods, form the essential toolbox for engineering and probing ultracold atomic systems for quantum simulation.

2.1 Electronic Structure of Rubidium

Ultracold atom experiments typically use alkali metals because their hydrogen-like structure provides the simplest electronic configuration. These elements, which

make up Group 1 of the periodic table, each have a single valence electron outside a closed-shell core. This gives them a straightforward electronic structure compared to atoms with multiple valence electrons. All of the experiments in this thesis use rubidium (Rb), a representative alkali atom. For excited states of alkali atoms, the relevant angular momentum operators—orbital angular momentum $\hat{L}$ and spin angular momentum $\hat{S}$—act solely on this lone valence electron.

The state of the valence electron is described by four quantum numbers. Its orbital motion is specified by the principal quantum number n, the orbital angular momentum quantum number l, and the magnetic quantum number m_L, which represents the projection of $\hat{L}$ onto a chosen quantization axis. The electron's intrinsic spin $s = \frac{1}{2}$ adds the spin projection $m_S = \pm\frac{1}{2}$. For each l, m_L takes integer values from $-l$ to $+l$. Orbital states are conventionally labeled with spectroscopic notation [38]: $S, P, D, F, \ldots$ for $l = 0, 1, 2, 3, \ldots$. Spin multiplicity, $2S+1$, equals 2 for alkali atoms and is typically omitted since it is constant.

Rubidium's electron configuration consists of four filled inner shells with a single valence electron occupying the $5S$ orbital. Figure 2.1 illustrates the energy levels of the $5S$ ground state, the first excited state $5P$ and illustrates splittings from fine structure and hyperfine structure.

Fine structure arises from relativistic corrections to the electron's motion, including changes to the kinetic energy and spin-orbit coupling, described by a term proportional to $\hat{L} \cdot \hat{S}$. Diagonalizing the Hamiltonian including this term produces eigenstates characterized by total electronic angular momentum $\hat{J} = \hat{L} + \hat{S}$, with quantum numbers j and m_J. These states are labeled using nL_j notation.

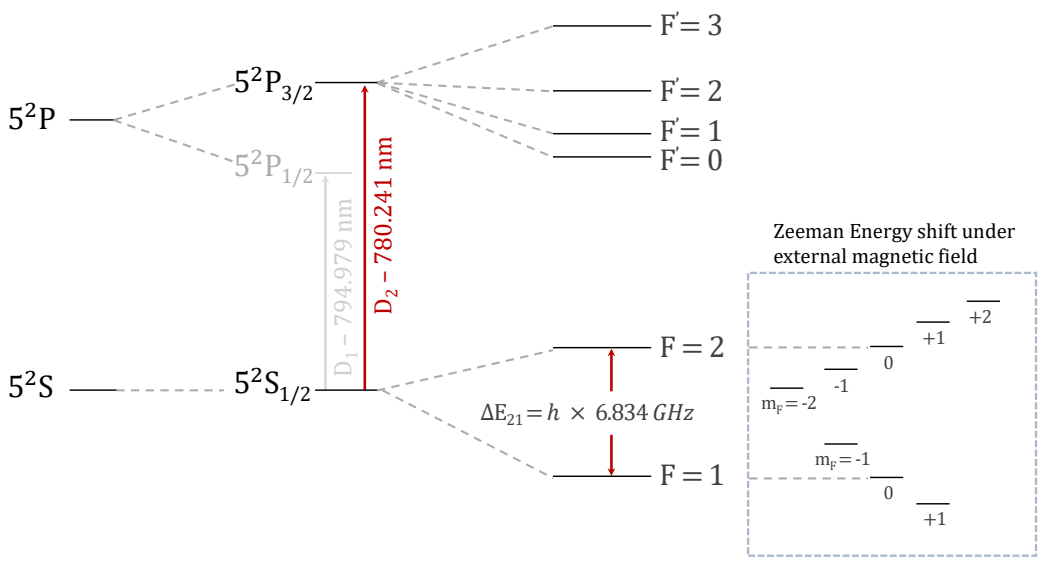

Figure 2.1: Electronic structure of ^{87}Rb. D1, $5^2P_{1/2} \rightarrow 5^2S_{1/2}$ (gray arrow), and D2, $5^2P_{3/2} \rightarrow 5^2S_{1/2}$ (red arrow). Coupling to the nuclear spin further splits the fine structure levels into hyperfine states (not shown for $5^2P_{1/2}$). The ground-state splitting ΔE_{21} between $F = 1$ and $F = 2$ is set by the magnetic dipole constant, $A_{\text{hfs}} = h \times 3.417$ GHz. Values for wavelengths and frequency differences are given in Ref. [39].

For ^{87}Rb, the $5S_{1/2}$ ground state has $l = 0$ and $j = 1/2$, so it exhibits no fine structure splitting. In contrast, the $5P$ state has $l = 1$, combining with $s = 1/2$ to give $j = 1/2$ and $j = 3/2$, resulting in fine structure levels $5P_{1/2}$ and $5P_{3/2}$. Optical transitions from $5S_{1/2}$ to these levels produce the D-lines [39]:

$$5S_{1/2} \rightarrow 5P_{1/2} \quad (\text{D}_1 \text{ line}), \quad \lambda_{\text{D1}} = 794.98 \text{ nm}, \quad f_{\text{D1}} = 377.11 \text{ THz},$$

$$5S_{1/2} \rightarrow 5P_{3/2} \quad (\text{D}_2 \text{ line}), \quad \lambda_{\text{D2}} = 780.24 \text{ nm}, \quad f_{\text{D2}} = 384.23 \text{ THz}.$$

The fine structure splitting is then $\Delta E_{\text{FS}} = h(f_{\text{D2}} - f_{\text{D1}}) = h \times 7.12$ THz. Beyond fine structure, hyperfine interactions arise from the coupling of the nuclear magnetic moment—which is proportional to the nuclear spin operator $\hat{I}$—to the magnetic field

produced by the electrons [40, 41], and is represented in the Hamiltonian by a term proportional to $\hat{I} \cdot \hat{J}$, where $\hat{J}$ is the total electronic angular momentum. For ^{87}Rb, $I = 3/2$, giving total atomic angular momentum $\hat{F} = \hat{J} + \hat{I}$ with quantum numbers f and m_F. The ground state, $5S_{1/2}$, then splits into hyperfine levels $F = 1$ and $F = 2$, separated by $h \times 6.8347$ GHz, as illustrated in Fig. 2.1.

2.2 Interaction with Magnetic Fields

Magnetic fields are essential for defining and manipulating atomic spin states, as well as for creating magnetic confinement. Each atom carries an intrinsic magnetic moment arising from the motion and spin of its charged constituents. These magnetic moments are directly associated with the electronic orbital, electronic spin, and nuclear angular momenta, which together determine the total magnetic moment operator:

$$\hat{\boldsymbol{\mu}} = -\frac{\mu_B}{\hbar}\left(g_S\hat{\boldsymbol{S}} + g_L\hat{\boldsymbol{L}} + g_I\hat{\boldsymbol{I}}\right), \tag{2.1}$$

where μ_B is the Bohr magneton, and g_S, g_L, and g_I are the Landé g-factors associated with the spin, orbital, and nuclear angular momentum, respectively.

When an atom is placed in an external magnetic field $\mathbf{B}$, these magnetic moments interact with the field through the Zeeman effect, producing energy shifts proportional to $-\hat{\boldsymbol{\mu}} \cdot \mathbf{B}$. In the regime where this Zeeman interaction is small compared to the hyperfine coupling, the total angular momentum $\hat{\boldsymbol{F}} = \hat{\boldsymbol{I}} + \hat{\boldsymbol{J}}$ remains well-defined,

and the interaction Hamiltonian can be written as:

$$\hat{H}_{\text{int}} = \frac{\mu_B g_F}{\hbar} \hat{\boldsymbol{F}} \cdot \mathbf{B}, \tag{2.2}$$

where g_F is the hyperfine Landé g-factor, expressed in terms of the electronic and nuclear contributions as:

$$g_F = g_J \frac{F(F+1) - I(I+1) + J(J+1)}{2F(F+1)} + g_I \frac{F(F+1) + I(I+1) - J(J+1)}{2F(F+1)}, \tag{2.3}$$

with

$$g_J = 1 + \frac{J(J+1) + S(S+1) - L(L+1)}{2J(J+1)} \tag{2.4}$$

being the Landé factor associated with the total electronic angular momentum $\hat{\boldsymbol{J}} = \hat{\boldsymbol{L}} + \hat{\boldsymbol{S}}$. The approximate values $g_S \simeq 2$ and $g_L \simeq 1$ are well known for alkali atoms, while g_I is much smaller and must be measured experimentally. For ^{87}Rb, $g_I = -0.0009951$ [39, 42]. Owing to its small magnitude, nuclear contributions are typically negligible in comparison to the electronic terms.

The energy structure of atoms in magnetic fields can be analyzed in two limiting regimes. At low fields—often called the *anomalous Zeeman* regime—the internal coupling between the electronic and nuclear spins dominates over the interaction with the external field. In this case, F remains a good quantum number, and the eigenstates are labeled by $|F, m_F\rangle$. As the magnetic field increases, the Zeeman term becomes comparable to or larger than the hyperfine coupling, eventually leading to the *Paschen–Back regime*, where the relevant eigenstates are more accurately

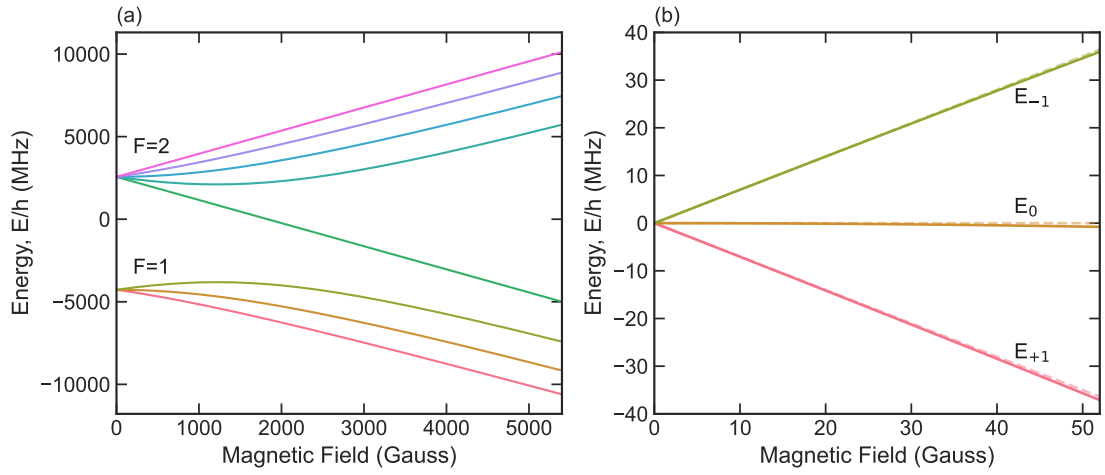

Figure 2.2: Zeeman splitting of the $5^2S_{1/2}$ ground-state manifold of ^{87}Rb. (a) Magnetic sublevels as a function of magnetic field strength, showing the transition from the low-field (linear Zeeman) to high-field (Paschen–Back) regimes. (b) Detail of the $F = 1$ manifold, comparing the linear approximation (dashed) with the exact Breit–Rabi solutions (solid), where their difference corresponds to the quadratic Zeeman correction.

described by $|m_J, m_I\rangle$.

For alkali atoms with $S = 1/2$, such as rubidium, the energy levels as a function of magnetic field strength can be computed analytically using the Breit–Rabi formula [43]:

$$E = \frac{\Delta E_{\mathrm{HFS}}}{2(2I+1)} + g_I \mu_B (m_I \pm m_J) B \pm \frac{\Delta E_{\mathrm{HFS}}}{2} \sqrt{1 + \frac{4(m_I \pm m_J)x}{2I+1} + x^2}, \tag{2.3}$$

where

$$x = \frac{\mu_B B (g_I - g_J)}{\Delta E_{\mathrm{HFS}}}. \tag{2.4}$$

For ^{87}Rb, the combinations $m_I \pm m_J$ take values from -2 to 2.

In our experiments, we primarily operate in the low-field regime where the Zeeman

shift is nearly linear in field strength:

$$\Delta E \approx g_F m_F \mu_B B. \tag{2.5}$$

Although the $|m_F = 0\rangle$ states do not experience a first-order shift near $B = 0$, they do exhibit a second-order, quadratic Zeeman effect given by:

$$\Delta E_q = \frac{(g_i - g_j)^2 \mu_B^2 B^2}{\hbar \Delta E_{\mathrm{HFS}}}. \tag{2.5}$$

This small correction means that the m_F levels are not equally spaced in energy. In typical operating conditions, the Zeeman splitting in our apparatus is $\Delta E \approx 1$ MHz, corresponding to a quadratic shift $\Delta E_q/h \approx 150$ Hz.

The magnetic interaction $-\hat{\boldsymbol{\mu}} \cdot \mathbf{B}$ also provides a means of generating magnetic trapping potentials for neutral atoms. In the low-field regime relevant to ^{87}Rb, $|F = 1, m_F = -1\rangle$ and $|F = 2, m_F = 1, 2\rangle$ define the low-field-seeking magnetic sublevels that are trappable and form the initial states from which our experiments begin.

2.3 Coherent Manipulation

Rabi oscillations describe the coherent population transfer between two quantum states under the influence of a near-resonant driving field. They form the fundamental framework for controlling internal states in atomic physics, enabling precise preparation, manipulation, and measurement of atomic populations. Under

the rotating wave approximation (RWA), rapidly oscillating terms proportional to $e^{-i(\omega+\omega_{ge})t}$ are neglected, assuming $\omega + \omega_{ge} \gg \omega - \omega_{ge}$. The effective Hamiltonian for a two-level system then becomes

$$\hat{H}_{\mathrm{RWA}} = \frac{\hbar}{2}\begin{pmatrix} -\Delta & \Omega \\ \Omega & \Delta \end{pmatrix}, \tag{2.6}$$

where $\Delta = \omega - \omega_{ge}$ is the detuning and Ω is the coupling strength. The eigenenergies of this Hamiltonian are

$$E_{\pm} = \pm\frac{\hbar\tilde{\Omega}}{2}, \qquad \tilde{\Omega} = \sqrt{\Omega^2 + \Delta^2}, \tag{2.7}$$

where $\tilde{\Omega}$ is the generalized Rabi frequency. If the system is initially prepared in the ground state $|g\rangle$, the excited-state population undergoes coherent Rabi oscillations:

$$|c_e(t)|^2 = \frac{\Omega^2}{\tilde{\Omega}^2}\sin^2\left(\frac{\tilde{\Omega}t}{2}\right), \tag{2.8}$$

which directly reflect the coherent dynamics induced by the drive [44].

This coherent control underlies many of the experiments presented in this thesis. For instance, in optical lattice experiments, Rabi oscillations arise from lattice-induced coupling between internal states, allowing direct measurement of the lattice Rabi frequency Ω_L. Similarly, resonant Raman pulses drive oscillations between spin-momentum states, providing a measure of the Raman coupling strength. The same principle applies to RF and microwave-driven transitions between hyperfine states,

enabling precise preparation and manipulation of atomic spin populations.

2.4 Near-Resonant Light-Atom Interactions

When near-resonant light passes through an atomic cloud, it experiences both a phase shift and attenuation due to scattering and absorption [45]. These interactions can be captured using a complex index of refraction,

$$\mathcal{N} = 1 + \mathcal{N}' + i\mathcal{N}'', \tag{2.9}$$

where the real part $\mathcal{N}'$ governs phase shifts, and the imaginary part $\mathcal{N}''$ describes amplitude loss. To avoid confusion with atomic density, we use $\mathcal{N}$ rather than n for the refractive index. The electric field of a plane wave propagating along z evolves according to

$$E(z) = E_0\, e^{i(\omega/c)z}\, e^{i\mathcal{N}'(\omega/c)z}\, e^{-\mathcal{N}''(\omega/c)z}. \tag{2.10}$$

Here, the first exponential is free-space propagation, the second captures the phase shift due to dispersion, and the third describes the attenuation caused by absorption and scattering. These effects directly determine the contrast and signal in absorption and phase-contrast imaging, which are widely used in ultracold atom experiments. For a dilute, non-magnetic atomic cloud, the index of refraction is related to the

atomic polarizability α by

$$\mathcal{N} \approx 1 + \frac{n\alpha}{2}, \quad \mathcal{N}' \approx \frac{n\,\mathrm{Re}[\alpha]}{2}, \quad \mathcal{N}'' \approx \frac{n\,\mathrm{Im}[\alpha]}{2}, \tag{2.11}$$

where n is the local atomic density, $\epsilon/\epsilon_0 \approx 1$, and $n\alpha \ll 1$. The polarizability itself arises from the dipole moment induced by the incident field, $\mathbf{d} = \alpha\mathbf{E}$. For a two-level atom driven near resonance, the polarizability is [45–47]

$$\alpha = \frac{2c}{\omega}\,\sigma\left(-\frac{\delta}{\Gamma} + i\frac{1}{2}\right), \tag{2.12}$$

where $\delta = \omega - \omega_0$ is the detuning from the atomic resonance ω_0, Γ is the natural linewidth, and σ is the effective absorption cross-section,

$$\sigma = \frac{\sigma_0}{1 + (2\delta/\Gamma)^2 + I/I_{\mathrm{sat}}}. \tag{2.13}$$

Here, $\sigma_0 = 6\pi c^2/\omega_0^2$ is the resonant cross-section, and $I_{\mathrm{sat}} = \hbar\omega_0^3\Gamma/(12\pi c^2)$ is the saturation intensity. The photon scattering rate is then

$$\gamma = \frac{\Gamma}{2}\frac{I/I_{\mathrm{sat}}}{1 + (2\delta/\Gamma)^2 + I/I_{\mathrm{sat}}}. \tag{2.14}$$

After traveling through a uniform cloud of length L, the electric field experiences a

phase shift and amplitude reduction:

$$E(L) = E_0\, e^{-in\sigma(\delta/\Gamma)L}\, e^{-n\sigma L/2}, \tag{2.15}$$

$$I_f = |E(L)|^2 = I_0\, e^{-n\sigma L}. \tag{2.16}$$

For non-uniform clouds, these quantities are calculated using integrals along the imaging axis:

$$\Delta\phi = -\int dz\, n(z)\, \sigma(z)\, \frac{\delta(z)}{\Gamma}, \tag{2.17a}$$

$$I_f = I_0 \exp\left[-\int dz\, n(z)\, \sigma(z)\right]. \tag{2.17b}$$

These expressions explicitly connect the optical response of the medium to the atomic density and form the foundation for absorption and phase-contrast imaging in ultracold atom experiments. Such imaging methods are essential for characterizing cloud density, spatial distributions, and dynamics, as well as for calibrating experimental parameters across the work presented in this thesis.

2.5 Quantum Gases

In this section, essential concepts from quantum statistics for degenerate gases are reviewed for relevance to ultracold atom experiments and to set the stage for the next few sections. A defining feature of atomic systems is that all atoms of a given species are fundamentally identical. For example, a ^{87}Rb atom, used in experiments

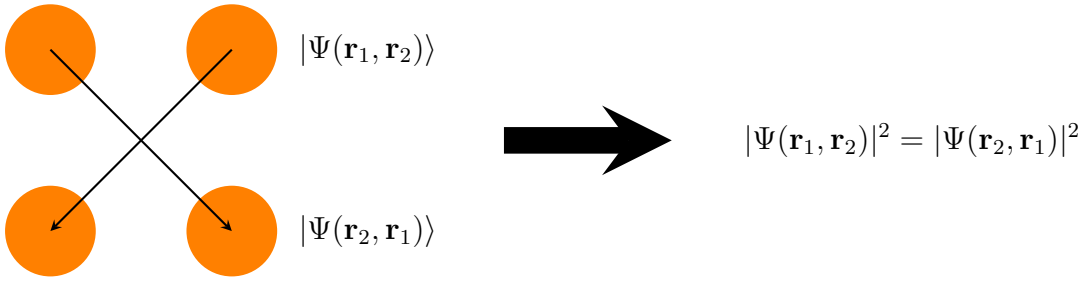

Figure 2.3: For indistinguishable particles, the probability distribution must remain unchanged under exchange.

making up this thesis, is indistinguishable from a ^{87}Rb atom in another laboratory across the world. The quantum nature of a degenerate quantum gas arises from this indistinguishability.

2.5.1 Identical Particles and Exchange Symmetry

Consider a quantum system of two identical particles, as illustrated in Fig. 2.3. Since the particles are indistinguishable, physical observables—such as the probability density—must remain unchanged under particle exchange. That is, the probability of finding particle 1 at position $\mathbf{r}_1$ and particle 2 at position $\mathbf{r}_2$ must be equal to the probability of finding particle 1 at $\mathbf{r}_2$ and particle 2 at $\mathbf{r}_1$ [48]:

$$|\psi(\mathbf{r}_1, \mathbf{r}_2)|^2 = |\psi(\mathbf{r}_2, \mathbf{r}_1)|^2. \tag{2.18}$$

When considering only single-valued wavefunctions, this leads to two possibilities

for how the wavefunction transforms under exchange:

$$\psi(\mathbf{r}_1, \mathbf{r}_2) = +\psi(\mathbf{r}_2, \mathbf{r}_1) \quad \text{(bosons, symmetric)}, \tag{2.19}$$

$$\psi(\mathbf{r}_1, \mathbf{r}_2) = -\psi(\mathbf{r}_2, \mathbf{r}_1) \quad \text{(fermions, antisymmetric)}. \tag{2.20}$$

These two symmetry classes define the two fundamental types of quantum particles—Bosons: symmetric wavefunctions, particles can occupy the same state, and Fermions: antisymmetric wavefunctions, obey the Pauli exclusion principle.

2.6 Bose-Einstein Condensation

The theoretical understanding of Bose-Einstein condensates (BECs) has evolved into a rich and active field within atomic, molecular and optical (AMO) physics [49,50]. Techniques developed to create atomic-gas condensates [51, 52] now form a crucial part of the experimental toolbox for studying phenomena that extend beyond AMO physics, using BECs as quantum simulators. The foundational concepts of Bose-Einstein condensation in an ideal, uniform, and non-interacting Bose gas in three dimensions are covered extensively in graduate-level statistical mechanics texts [53–56]. A summary of these derivations is provided in the following sections. Going beyond the ideal gas approximation, weak interactions between particles can be considered and insight into the behavior and dynamics of weakly interacting Bose systems can be studied.

2.6.1 Ideal Gas

Bose-Einstein condensation is a statistical phenomenon that emerges in a gas of identical bosons at low temperatures. It is most naturally described using temperature T and chemical potential μ as the key thermodynamic variables. The chemical potential represents the energy required to add or remove a particle from the system at fixed entropy and volume. A particularly useful way for describing Bose gases is allowing the total particle number to fluctuate while controlling the average through μ. This flexibility simplifies the treatment of phase transitions like Bose-Einstein condensation, where a macroscopic number of particles accumulate in the lowest energy state.

The Bose–Einstein distribution describes the average total number of particles at temperature T

$$\langle N \rangle = \sum_{\epsilon} \frac{1}{e^{\beta(\epsilon-\mu)} - 1}, \tag{2.21}$$

where the chemical potential must satisfy $\mu < \epsilon_0$, i.e. remain strictly below the ground state energy, ϵ denotes single-particle energy levels and $\beta = 1/(k_B T)$ is the inverse temperature.

It is often convenient to express this in terms of the fugacity $z = e^{\beta\mu}$, yielding:

$$\langle n(\epsilon) \rangle = \frac{z}{e^{\beta\epsilon} - z}. \tag{2.22}$$

The dependence of the occupation number on energy for various values of z is illustrated in Fig. 2.6.1. As $z \to 1$ (i.e., $\mu \to \epsilon_0$), the population of low-energy

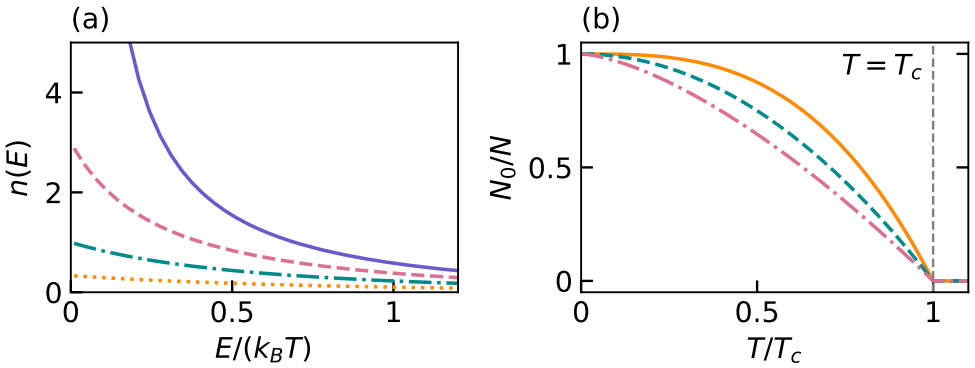

Figure 2.4: Bose–Einstein distribution. (a) Occupation number as a function of energy for fugacity $z = 0.25, 0.5, 0.75, 1$, corresponding to chemical potentials $\mu/k_BT = 1.39, 0.69, 0.29, 0$, respectively. Bose–Einstein condensation: $z = 1$ and $\mu = 0$ (solid curve). (b) Condensate fraction expressed as a function of temperature T/T_c for a non-interacting Bose gas in: a 3d harmonic trap (solid, $\alpha = 3$), a 2d harmonic trap (dashed, $\alpha = 2$), and in a 3d box (dash-dot, $\alpha = 3/2$).

states increases sharply, signaling the approach to condensation. Remarkably, this is possible for temperatures above absolute zero, and happens when the interparticle spacing becomes comparable to the thermal de Broglie wavelength

$$\lambda_T = \sqrt{\frac{2\pi\hbar^2}{Mk_BT}}. \tag{2.23}$$

In the thermodynamic limit, the sum over states can be replaced by an integral using the density of states. For a three-dimensional ideal Bose gas in a box, the density of states scales as:

$$g(\epsilon) \propto \epsilon^{1/2}. \tag{2.24}$$

The total number of particles separates into two components:

$$N = N_0 + N_{\text{exc}}, \tag{2.25}$$

where N_0 is the number of particles in the ground state and N_{exc} is the number in excited states. At high temperatures, $N_0 \approx 0$, and most particles occupy excited states. As the temperature decreases, μ approaches the ground state energy. At the critical temperature T_c, the excited states reach their maximum occupancy:

$$N_{\text{exc}} = \int_0^\infty \frac{g(\epsilon)}{e^{\beta(\epsilon-\mu)} - 1}\, d\epsilon. \tag{2.26}$$

Below T_c, any additional particles must accumulate in the ground state and the condensate fraction can be expressed as a function of temperature as

$$\frac{N_0}{N} = 1 - \left(\frac{T}{T_c}\right)^{3/2}. \tag{2.27}$$

Thus the critical temperature is given by:

$$T_c = \left(\frac{2\pi\hbar^2}{m k_B}\right)\left(\frac{n}{\zeta(3/2)}\right)^{2/3}, \tag{2.28}$$

where $n = N/V$ is the particle number density and $\zeta(\alpha)$ is the Riemann zeta function. Fig. 2.6.1 illustrates the condensate fraction expressed as a function of temperature T/T_c for a non-interacting Bose gas in: a 3d harmonic trap (solid, $\alpha = 3$), a 2d harmonic trap (dashed, $\alpha = 2$), and in a 3d box (dash-dot, $\alpha = 3/2$).

This condensation results from the indistinguishability of bosons and the statistical tendency to accumulate in the lowest energy state, and not from interparticle interactions. Bose-Einstein condensation is therefore a purely statistical phase transition marking the onset of quantum degeneracy.

2.6.2 Temperature

High-Temperature, Low-Density Regime: This regime refers to physical conditions where the gas behaves classically. It is characterized by a small phase-space density, meaning the thermal de Broglie wavelength λ_T is much smaller than the average interparticle spacing:

$$\lambda_T = \sqrt{\frac{2\pi\hbar^2}{mk_BT}} \ll n^{-1/3}. \tag{2.29}$$

In this limit, quantum effects are negligible, and the particle distribution reduces to the Maxwell-Boltzmann form:

$$f_T(\epsilon) = \exp\left[\frac{\mu - \epsilon}{k_BT}\right]. \tag{2.30}$$

In practice, in i.e., ultracold atom experiments, the Maxwell-Boltzmann distribution is often used to estimate the temperature of the gas. This is valid when the gas is sufficiently dilute and thermal, typically above the condensation temperature. By fitting the high-energy tail of the momentum or spatial distribution (where interactions are minimal and quantum effects are weak), an approximate temperature can be extracted using classical statistics.

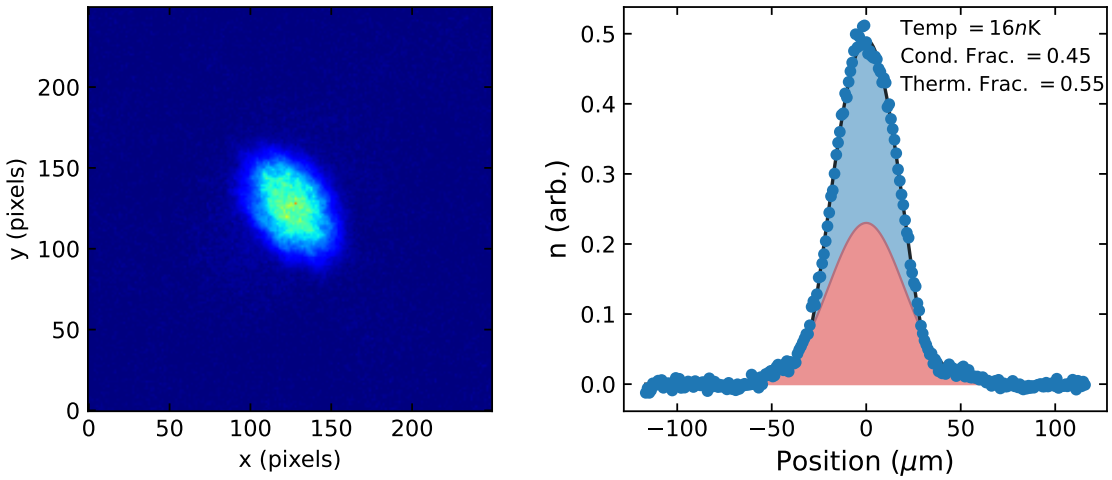

Figure 2.5: Estimating Temperature Using Maxwell-Boltzmann. Example image of a small Bose-Einstein condensate with a TF waist of 30μm, along with a fit to estimate temperture of the atomic cloud. Although the MB distribution is not valid for the condensed fraction below T_c, it remains useful for characterizing the thermal (non-condensed) component of low-density clouds.

2.6.3 Estimating Temperature Using Maxwell-Boltzmann

In the laboratory, the temperature of an ultracold atomic cloud is often estimated using the classical Maxwell-Boltzmann (MB) distribution, even when the system has reached quantum degeneracy. After time-of-flight expansion, the condensed and thermal fractions can be estimated, allowing the thermal tail to be independently analyzed. By fitting this portion of the cloud to the MB distribution, the temperature can be calculated. As a result, the MB fit remains a practical and widely used method for estimating temperature, even near or below the critical point for Bose-Einstein condensation.

The MB distribution for particle velocities in one dimension is given by

$$f(v) \propto \exp\left(-\frac{mv^2}{2k_BT}\right), \tag{2.31}$$

where m is the mass of the atoms, k_B is Boltzmann's constant, and T is the temperature. In time-of-flight experiments, atoms are released from the trap and allowed to expand freely. After a known expansion time t, an absorption image is taken. Since the atoms are non-interacting during expansion, their final positions x in the image correspond to their initial velocities via $v = x/t$. The resulting spatial distribution reflects the velocity distribution of the cloud. By fitting the absorption image to a Gaussian distribution, and comparing it with the MB form for kinetic energy,

$$\exp\left(-\frac{x^2}{2\sigma^2}\right) = \exp\left(-\frac{mx^2}{2k_BTt^2}\right), \tag{2.32}$$

one can equate the exponents and identify the relation between temperature and the measured width σ:

$$T = \frac{m\sigma^2}{k_Bt^2}. \tag{2.33}$$

Here, σ is the width of the atomic distribution and t is the time-of-flight duration. Note, that in practice, this equation will need to be modified to include applicable factors of camera pixels and magnification of the imaging system.

2.7 Scattering in Ultracold Bosonic Gases

In ultracold atomic gases, temperatures are typically on the order of nanoKelvin to microKelvin, as discussed in the previous section. At these low temperatures, the kinetic energy of atoms is extremely small: $E_{\text{kin}} \sim k_BT \ll 1\ \mu\text{eV}$. At these low energies, interactions are dominated by s-wave ($\ell = 0$) collisions, which is character-

ized by the s-wave scattering length, a. Higher partial waves (p-wave, d-wave, etc.) are suppressed. In this section, we analyze s-wave scattering for identical bosons and derive expressions for the cross section and effective interaction used in mean-field theories like the Gross–Pitaevskii equation (GPE). We then briefly introduce scattering between atoms in different internal states, focusing on the relevant spin channels for ^{87}Rb in the $F = 1$ manifold.

2.7.1 s-Wave Scattering of Identical Bosons

For two atoms with masses m_1 and m_2, the two-body problem reduces to that of a single particle of reduced mass $M = \frac{m_1 m_2}{m_1+m_2}$ moving in the relative direction. In the center-of-mass frame, the asymptotic form of the scattering wavefunction is [57]:

$$\psi(\mathbf{r}) = e^{i\mathbf{k}\cdot\mathbf{r}} + f(\theta)\frac{e^{i\mathbf{k}\mathbf{r}}}{\mathbf{r}}, \tag{2.34}$$

where $\mathbf{k}$ is the incoming wavevector and $f(\theta)$ is the scattering amplitude. At ultracold temperatures, only the s-wave ($\ell = 0$) partial wave contributes, making the amplitude isotropic:

$$f(\theta) = -a. \tag{2.35}$$

The differential cross section becomes:

$$\frac{d\sigma}{d\Omega} = |f(\theta)|^2 = a^2, \tag{2.36}$$

and integrating over the solid angle yields the total cross section:

$$\sigma = 4\pi a^2. \tag{2.37}$$

However, for identical bosons, quantum statistics require symmetrization of the wavefunction, leading to a symmetrized scattering amplitude:

$$f_B(\theta) = f(\theta) + f(\pi - \theta) = 2f(\theta) = -2a. \tag{2.38}$$

The corresponding total cross section becomes:

$$\sigma_{\text{boson}} = \int |f_B(\theta)|^2 d\Omega = 8\pi a^2. \tag{2.39}$$

This factor of 4 enhancement in cross section (compared to distinguishable particles) is fundamental in describing mean-field interactions in BECs. In contrast, identical fermions in the same spin state cannot scatter via s-wave due to antisymmetry, resulting in $\sigma = 0$ and suppressed thermalization.

The interaction potential can be replaced by a contact pseudopotential:

$$U_{\text{eff}}(\mathbf{r}) = g\delta(\mathbf{r}), \quad \text{with} \quad g = \frac{4\pi\hbar^2 a}{m}. \tag{2.40}$$

This interaction term captures short-range collisions between atoms, specifically low-energy two-body s-wave scattering, which dominate in ultracold ^{87}Rb gases. Note that short-range is with respect to other relevant length scales, such as the healing

length or trap size.

2.7.2 Scattering Between Different Internal States

For ^{87}Rb atoms in the $F = 1$ hyperfine manifold, there are only two allowed s-wave scattering channels due to Bose symmetry: $F_{\text{tot}} = 0$ and $F_{\text{tot}} = 2$. These channels correspond to symmetric two-particle spin states. The antisymmetric $F_{\text{tot}} = 1$ channel is forbidden [58–60].

Alkali atoms such as ^{87}Rb have multiple internal states arising from hyperfine splitting. In the $F = 1$ manifold, the three Zeeman sublevels ($m_F = -1,\ 0,\ +1$) form a spin-1 system. When two identical bosons interact, their total spin state must be symmetric under particle exchange due to Bose statistics. For spin-1 atoms, the two-particle spin basis decomposes into total spin channels: $F_{\text{tot}} = 0,\ 1,\ 2$.

However, only the $F_{\text{tot}} = 0$ and $F_{\text{tot}} = 2$ channels are symmetric; the $F_{\text{tot}} = 1$ channel is antisymmetric and thus forbidden. As a result, there are only two independent s-wave scattering lengths for $F = 1$ ^{87}Rb: (1) a_0 for $F_{\text{tot}} = 0$ and (2) a_2 for $F_{\text{tot}} = 2$. These two parameters govern the spinor interaction Hamiltonian and takes the form:

$$\hat{H}_{\text{int}} = \frac{c_0}{2}\hat{n}^2 + \frac{c_2}{2}\hat{\mathbf{F}}^2, \tag{2.41}$$

where

$$c_0 = \frac{4\pi\hbar^2}{m} \cdot \frac{a_0 + 2a_2}{3}, \tag{2.42}$$

$$c_2 = \frac{4\pi\hbar^2}{m} \cdot \frac{a_2 - a_0}{3}. \tag{2.43}$$

Here, $\hat{n}$ is the local density operator and $\hat{\mathbf{F}}$ is the spin density operator. The c_0

term describes spin-independent interactions, while c_2 governs spin exchange and spin-mixing dynamics. For the scope of the GPE simulations in this thesis, $c_0 = c_2$, which is effectively saying that the two s-wave scattering lengths are related in a very specific way: $a_0 = -a_2$. The above structure underlies many features of spinor condensates, including ground-state phase diagrams and non-equilibrium dynamics. A more in depth overview can be found in reference [61].

2.8 Gross-Pitaevskii Equation

The Gross–Pitaevskii equation (GPE) provides a remarkably effective mean-field framework for describing the behavior of weakly interacting Bose gases at ultracold temperatures. In the dilute limit, where the majority of atoms occupy the same quantum state, the GPE captures both the static and dynamic properties of a Bose–Einstein condensate. Despite its simplicity, this nonlinear Schrödinger-type equation successfully reproduces a wide range of experimental observations, making it one of the central tools in the study of quantum gases [49,50,62–68]. A thorough discussion of its generalizations to multicomponent or spinor condensates, including $F = 1$ systems, can be found in Ref. [69,70] and in the thesis [68]. In the Heisenberg picture, the dynamics of a bosonic field operator $\hat{\Psi}(\mathbf{r}, t)$ describing a many-body system is governed by the Heisenberg equation of motion:

$$i\hbar \frac{\partial \hat{\Psi}(\mathbf{r}, t)}{\partial t} = \left[\hat{\Psi}(\mathbf{r}, t), \hat{H}\right] = \left[-\frac{\hbar^2}{2m}\nabla^2 + V_{\text{ext}}(\mathbf{r}, t) + \int d^3r'\, \hat{\Psi}^\dagger(\mathbf{r}', t) V(\mathbf{r}' - \mathbf{r}) \hat{\Psi}(\mathbf{r}', t)\right] \hat{\Psi}(\mathbf{r}, t), \tag{2.44}$$

where $V_{\text{ext}}(\mathbf{r}, t)$ denotes the external trapping potential and $V(\mathbf{r}' - \mathbf{r})$ represents the two-body interaction potential between atoms.

At ultra low temperatures, most atoms condense into the same quantum state. Under these conditions, the operator $\hat{\Psi}$ can be replaced by a complex-valued mean-field wavefunction $\Psi_0(\mathbf{r}, t)$, which acts as the condensate order parameter. Since the range of atomic interactions is typically much smaller than the average inter-particle spacing $d \sim n^{-1/3}$, only two-body collisions contribute significantly. For such dilute gases, the two-body interaction, or rather the interatomic potential, is well-approximated by an effective contact interaction:

$$V(\mathbf{r}' - \mathbf{r}) = g\delta(\mathbf{r}' - \mathbf{r}), \quad \text{with} \quad g = \frac{4\pi\hbar^2 a}{m}, \tag{2.45}$$

where a is the s-wave scattering length. This description is valid when the diluteness condition $|a| \ll n^{-1/3}$ is satisfied, ensuring that the low-energy scattering properties are entirely captured by a. Next, substituting the contact potential, Eq. (2.45), into the Heisenberg equation, Eq. (2.44), and replacing the operator with the classical field yields the time-dependent Gross–Pitaevskii equation:

$$i\hbar\frac{\partial\Psi_0(\mathbf{r}, t)}{\partial t} = \left[-\frac{\hbar^2}{2m}\nabla^2 + V_{\text{ext}}(\mathbf{r}, t) + g|\Psi_0(\mathbf{r}, t)|^2\right]\Psi_0(\mathbf{r}, t). \tag{2.46}$$

Stationary solutions describe condensate wavefunctions whose time evolution satisfies the condition:

$$\Psi_0(\mathbf{r}, t) = \psi(\mathbf{r})e^{-i\mu t/\hbar}, \tag{2.47}$$

where μ is the chemical potential, fixed by normalizing the wavefunction to the total number of particles. Substituting this expression into the time-dependent equation, Eq. (2.46), yields the time-independent Gross–Pitaevskii equation:

$$\mu\psi(\mathbf{r}) = \left[-\frac{\hbar^2}{2m}\nabla^2 + V_{\text{ext}}(\mathbf{r}) + g|\psi(\mathbf{r})|^2\right]\psi(\mathbf{r}). \tag{2.48}$$

For a dilute Bose gas with repulsive interactions—i.e., a positive scattering length $a > 0$, as in the case of ^{87}Rb—the stationary solution of this equation corresponds to the system's ground state [67].

2.8.1 Thomas–Fermi Approximation for BECs in a Harmonic Trap

In the regime where interaction energy dominates over kinetic energy, i.e., $g|\psi(\mathbf{r})|^2 \gg \hbar\omega_j$, the kinetic term in GPE, Eq. (2.48), can be neglected. This defines the Thomas–Fermi (TF) approximation:

$$\mu = V_{\text{ext}}(\mathbf{r}) + g|\psi_{\text{TF}}(\mathbf{r})|^2, \tag{2.49}$$

yielding the TF density profile:

$$n_{\text{TF}}(\mathbf{r}) = |\psi_{\text{TF}}(\mathbf{r})|^2 = \frac{1}{g}\left(\mu - V_{\text{ext}}(\mathbf{r})\right), \tag{2.50}$$

valid where $\mu > V_{\text{ext}}(\mathbf{r})$ and zero otherwise.

In the presence of a harmonic trapping potential of the form

$$V_{\text{ext}}(\mathbf{r}) = \frac{1}{2}m \sum_{j=x,y,z} \omega_j^2 r_j^2, \tag{2.51}$$

the resulting condensate density profile takes the shape of an inverted paraboloid. The Thomas–Fermi radii along each spatial direction are given by

$$R_j = \sqrt{\frac{2\mu}{m\omega_j^2}}, \quad j = x, y, z. \tag{2.52}$$

The chemical potential μ can then be expressed as

$$\mu_{TF} = \frac{15Ng}{8\pi R_x R_y R_z} = \hbar\bar{\omega}\left(\frac{15Na}{a_{\text{ho}}}\right)^{2/5}, \tag{2.53}$$

where $\bar{\omega} = (\omega_x\omega_y\omega_z)^{1/3}$ is the geometric mean of the trap frequencies and $a_{\text{ho}} = \sqrt{\hbar/m\bar{\omega}}$ is the harmonic oscillator length. The chemical potential μ, which defines the central mean-field energy of a BEC, governs its spatial extent, i.e. size and shape, and excitation properties. In the presence of a trapping potential, μ depends on the trap geometry, where it scales with atom number, scattering length, and the geometric mean of the trap frequencies.

The Thomas–Fermi approximation fails near the condensate boundary, where the density approaches zero and the kinetic energy can no longer be neglected. In this region, the characteristic healing length becomes relevant:

$$\xi = \frac{\hbar}{\sqrt{2mgn_0}}, \quad n_0 = n_{\text{TF}}(r = 0) = \frac{\mu}{g}. \tag{2.54}$$

The healing length gives the minimum distance over which the condensate wavefunction can *heal*, effectively quantifying how rapidly the BEC wavefunction responds to variations in the external potential. For the mean-field description to remain valid, the healing length must be much smaller than any characteristic length scale in the system, such as the trap size or wavelength of excitations. It also determines the core size of quantized vortices in a superfluid—representing the distance over which the wavefunction rises from zero at the vortex center to its central-density value away from the core.

Having established the characteristic length scales governing condensate structure, we now turn to how external fields can modify condensate dynamics. In particular, artificial gauge fields introduce effective vector potentials into the system, requiring a modification of the kinetic energy term in the Gross–Pitaevskii Hamiltonian to account for the resulting synthetic electromagnetic interactions.

2.9 Numerical Simulations of GPE

Depending on the physics being studied and the experimental environment, the choice of gauge—most commonly between the Landau gauge and the symmetric gauge—plays an important role in describing the analog system. The Landau gauge is typically favored in ultracold atom experiments without axial / cylindrical symmetry, and where synthetic magnetic fields are created via light-induced couplings. For example, in vortex nucleation studies [71], it's demonstrated that the gauge does matter, and they show how the vector potential in the Landau gauge corresponds

to the exact Raman-dressed dispersion relationship (see Fig. 4 in Ref. [71]).

In contrast, the symmetric gauge is particularly relevant for systems with circular trapping geometries, such as in experiments exploring lowest Landau level physics in a rotating Bose–Einstein condensate [72]. In such setups, the circular symmetry of the trap aligns naturally with the form of the symmetric gauge vector potential, making it the clearer and more intuitive choice. Quantum Hall systems also provide a classic setting where gauge choice is essential: while both gauges are formally equivalent, the Landau gauge often simplifies calculations of edge states, while the symmetric gauge is better suited for analyzing bulk properties, especially in rotating condensates [73]. Altogether, these examples demonstrate that although physical observables remain gauge invariant, selecting between the Landau and symmetric gauge highlights different aspects of synthetic gauge fields, aligning the theoretical framework with the system's geometry and dynamics.

While single-particle physics can provide useful insight regarding Raman-dressed BECs, it does not capture the collective behavior arising from interactions in many-body quantum systems. All of the simulations conducted for this thesis begin by solving the Gross–Pitaevskii Hamiltonian in 2d. To model such effects, we use the GPE, which provides a mean-field description of the condensate and incorporates interaction-driven dynamics, such as vortex formation and collective excitations. To study artificial gauge fields and better understand the choice between Landau and symmetric gauges—alongside performing key GPE validation tests—we begin by considering the case of a spinless system. The Gross–Pitaevskii Hamiltonian

describing this environment can be written as:

$$\hat{H}_{GP} = \frac{1}{2m}\left(\hat{\boldsymbol{p}} - \boldsymbol{\mathcal{A}}\right)^2 + \frac{1}{2m}\omega_x^2 x^2 + \frac{1}{2m}\omega_y^2 y^2 + g_{2d}|\Psi|^2, \tag{2.55}$$

where $\hat{\boldsymbol{p}} = -i\hbar\boldsymbol{\nabla}$ is the momentum operator, $\boldsymbol{\mathcal{A}}$ is the artificial vector potential associated with the applied gauge field, and $\boldsymbol{\nabla}$ is the gradient operator. The terms involving ω_x and ω_y describe harmonic confinement along the x and y directions, respectively. The coefficient g_{2d} is the effective two-dimensional interaction strength, and Ψ is the condensate wavefunction normalized to the total number of particles.

2.9.1 Vector Potentials & Gauge Criterion - Symmetric to Landau

To examine gauge dependence, we solve the GPE in two dimensions for a BEC subjected to a uniform magnetic field $\boldsymbol{\mathcal{B}} = \mathcal{B}_0\hat{z}$. Because the magnetic field is constant, the system is translationally and rotationally invariant in the x-y plane, and we adopt a generalized vector potential of the form:

$$\boldsymbol{\mathcal{A}} = -y\mathcal{B}_0(1-\varepsilon)\,\hat{x} + x\mathcal{B}_0\varepsilon\,\hat{y}, \quad 0 \le \varepsilon \le 1, \tag{2.56}$$

which smoothly interpolates between Landau gauge ($\varepsilon = 0$) and symmetric gauge ($\varepsilon = 0.5$). Note that this choice ensures $\boldsymbol{\nabla}\cdot\boldsymbol{\mathcal{A}} = 0$. While both vector potentials yield the same magnetic field, they emphasize different symmetries and boundary conditions in the system. Landau gauge preserves translational symmetry along one direction, making it convenient for studying extended systems and edge effects.

Symmetric gauge, on the other hand, preserves rotational symmetry around the origin, which is particularly useful for analyzing vortex structures and angular momentum properties. By varying ε, one can systematically explore how gauge choice influences both the computational behavior of the GPE solutions and physical observables such as condensate density profiles and vortex dynamics.

Symmetric Gauge. The Gross– Pitaevskii Hamiltonian in 2d implementing the symmetric gauge is

$$\hat{H}_{GP} = \frac{1}{2m}\left[p_x\hat{x} + p_y\hat{y} + \frac{y\mathcal{B}_0}{2}\hat{x} - \frac{x\mathcal{B}_0}{2}\hat{y}\right]^2 + V(x,y) + g_{2d}|\Psi|^2 \tag{2.57}$$

$$= \underbrace{\frac{p_x^2}{2m} + \frac{\mathcal{B}_0 y p_x}{2m}}_{\mathrm{H}_{p_x y}} + \underbrace{\frac{p_y^2}{2m} - \frac{\mathcal{B}_0 x p_y}{2m}}_{\mathrm{H}_{x p_y}} + \underbrace{\frac{\mathcal{B}_0^2 y^2}{4m} + \frac{\mathcal{B}_0^2 x^2}{4m} + V(x,y) + g_{2d}|\Psi|^2}_{\mathrm{H}_{xy}}. \tag{2.58}$$

Time Evolution Operator and Symmetric Gauge. The time evolution of the wavefunction, which is gauge independent, is given by

$$\big|\Psi(\boldsymbol{r}, t+\Delta t)\big\rangle = U(t, t+\Delta t)\big|\Psi(\boldsymbol{r}, t)\big\rangle, \tag{2.59}$$

where $U(t, t+\Delta t)$ is the time evolution operator. For small Δt, the following operator forms are accurate to first and second order in Δt, respectively:

$$U_{O(\Delta t)} = e^{-\frac{i}{\hbar}\Delta t\hat{H}} = e^{-\frac{i}{\hbar}\Delta t\hat{H}_{p_x y}} e^{-\frac{i}{\hbar}\Delta t\hat{H}_{x p_y}} e^{-\frac{i}{\hbar}\Delta t\hat{H}_{xy}} + O(\Delta t^2) \tag{2.60}$$

$$U_{O(\Delta t^2)} = e^{-\frac{i}{\hbar}\frac{\Delta t}{2}\hat{H}_{p_x y}} e^{-\frac{i}{\hbar}\frac{\Delta t}{2}\hat{H}_{x p_y}} e^{-\frac{i}{\hbar}\Delta t\hat{H}_{xy}} e^{-\frac{i}{\hbar}\frac{\Delta t}{2}\hat{H}_{x p_y}} e^{-\frac{i}{\hbar}\frac{\Delta t}{2}\hat{H}_{p_x y}} + O(\Delta t^3). \tag{2.61}$$

The time evolution operator can be constructed using

$$e^{A/2}e^{B/2} \approx \exp\left[\tfrac{1}{2}(A+B) + \tfrac{1}{8}[A,B] + O(\Delta t^3) + \cdots + O(\Delta t^n)\right], \tag{2.62}$$

the Baker–Campbell–Hausdorff–Dynkin (BCHD) identity, which provides a systematic way to achieve, and/or verify, higher-order accuracy in Δt when composing noncommuting exponentials, such as in Suzuki–Trotter approximations [74,75]. The expansion can be extended to arbitrary order in Δt via nested commutators, though in practice only terms up to $O(\Delta t^n)$ are retained. For example, verifying second-order accuracy involves showing that the final expression is absent of explicit $O(\Delta t^2)$ correction terms. In particular, the five-term symmetric decomposition used for $U_{O(\Delta t^2)}$ in Eq. 2.61 is a form of Strang splitting [76], and note that the accuracy is unaffected by the ordering of exponentials, so long as the symmetric half-step structure is preserved. In practice, strategic arrangement of the sequence can reduce the number of Fourier transforms required during time evolution. Although third-order accuracy (i.e., error scaling as $O(\Delta t^4)$) can, in principle, be achieved by tuning prefactors for each exponential, the resulting solutions form a non-unique family of decompositions. In contrast, fourth-order accuracy (error scaling as $O(\Delta t^5)$) is particularly appealing as a unique set of coefficients exists, making implementation unambiguous and often more stable for long-time evolution; see, for instance, the constructions by Yoshida and Suzuki [77, 78].

Landau Gauge. We now focus on the Gross–Pitaevskii Hamiltonian in 2d expressed

in the Landau gauge

$$\hat{H}_{GP} = \frac{\hat{p}^2}{2m} + \frac{\boldsymbol{\mathcal{A}}^2}{2m} - \frac{\boldsymbol{\mathcal{A}} \cdot \hat{p}}{m} + \frac{i\hbar}{2m}\boldsymbol{\nabla} \cdot \boldsymbol{\mathcal{A}} + V(x,y) + g_{2d}|\Psi|^2 \tag{2.63}$$

$$= \frac{\hat{p_x}^2}{2m} + \frac{\hat{p_x}^2}{2m} + \frac{\mathcal{A}_x^2}{2m} - \frac{\mathcal{A}_x}{m}\hat{x} \cdot (p_x\hat{x} + p_y\hat{y}) + \frac{i\hbar}{2m}\left(\frac{\delta \mathcal{A}_x}{\delta x}\right) + V(x,y) + g_{2d}|\Psi|^2 \tag{2.64}$$

$$= \frac{\hat{p_x}^2}{2m} + \frac{\hat{p_x}^2}{2m} + \frac{\mathcal{A}_x^2}{2m} - \frac{\mathcal{A}_x p_x}{m} + \frac{i\hbar}{2m}\left(\frac{\delta \mathcal{A}_x}{\delta x}\right) + V(x,y) + g_{2d}|\Psi|^2. \tag{2.65}$$

Here, the term proportional to $\boldsymbol{\nabla} \cdot \boldsymbol{\mathcal{A}}$ arises from the commutator

$$[\hat{p}_j, \mathcal{A}_j] = -i\hbar\frac{\partial \mathcal{A}_j}{\partial x_j}, \tag{2.66}$$

which is nonzero when $\boldsymbol{\mathcal{A}}$ depends on position. Note that the parenthesis on this term in the Hamiltonian indicates that $\frac{\delta}{\delta x}$ is not an operator and applies only to $\mathcal{A}_x$.

Time evolution operator and Landau gauge. Just as we saw previously, the time evolution of the wavefunction is given by

$$\big|\Psi(\boldsymbol{r}, t + \Delta t)\big\rangle = U(t, t + \Delta t)\big|\Psi(\boldsymbol{r}, t)\big\rangle, \tag{2.67}$$

where $U(t, t + \Delta t)$ is the time evolution operator. For small Δt, with the Landau gauge, the time evolution operator

$$U = e^{-\frac{i}{\hbar}\Delta t\hat{H}} = e^{-\frac{i}{\hbar}\frac{\Delta t}{2}\hat{H}_{xy}} e^{-\frac{i}{\hbar}\frac{\Delta t}{2}\hat{H}_{p_x p_y}} e^{-\frac{i}{\hbar}\Delta t\hat{H}_{xyp_x}} e^{-\frac{i}{\hbar}\frac{\Delta t}{2}\hat{H}_{p_x p_y}} e^{-\frac{i}{\hbar}\frac{\Delta t}{2}\hat{H}_{xy}}, \tag{2.68}$$

and taking the Taylor expansion for the coupled term $e^{-\frac{i}{\hbar}\Delta t\hat{H}_{xyp_x}}$, gives

$$1 + \frac{i}{\hbar}\Delta t\frac{\mathcal{A}_x p_x}{m} - \frac{\Delta t^2}{2\hbar^2 m^2}[\mathcal{A}_x^2 p_x^2 - i\hbar\mathcal{A}_x\frac{\delta}{\delta x}\mathcal{A}_x p_x], \tag{2.69}$$

which is correct up to $O(\Delta t^3)$.

Vector potential engineering and gauge choice. We engineer our vector potential to have a single non-zero component $\boldsymbol{\mathcal{A}} = (\mathcal{A}_x, 0, 0)$ and the magnetic field follows as $\boldsymbol{\mathcal{B}} = (0, 0, \mathcal{B}_z(x, y)) = -\delta\mathcal{A}_x/\delta y$. Here, we'll utilize the magnetic field component $\mathcal{B}_z$ in its integral form and the vector potential component $\mathcal{A}_x$ can be written as

$$\mathcal{A}_x(x, y) = -\int_0^y \mathcal{B}_z(x, y)\,\mathrm{d}y, \tag{2.70}$$

where it is a function of x and y.

2.9.2 Verification of Hermiticity

All observables have to be Hermitian. If we evaluate our Hamiltonian

$$\hat{H} = \frac{1}{2m}\left(\hat{\boldsymbol{p}} - \boldsymbol{\mathcal{A}}\right)^2 = \frac{\hat{\boldsymbol{p}}^2}{2m} + \frac{\boldsymbol{\mathcal{A}}^2}{2m} - \underbrace{\frac{\boldsymbol{\mathcal{A}}\cdot\hat{\boldsymbol{p}}}{m}} + \underbrace{\frac{i\hbar}{2m}\boldsymbol{\nabla}\cdot\boldsymbol{\mathcal{A}}}, \tag{2.71}$$

we notice that the last two terms are not independently Hermitian. The last term brings this up since the derivative is only applying to $\mathcal{A}$ and is not an operator. This initially appears problematic, however it turns out that the sum of the two is

Hermitian and the proof if given below:

$$\hat{p}^\dagger = \hat{p}; \quad \mathcal{A}^\dagger = \mathcal{A}; \quad (AB)^\dagger = B^\dagger A^\dagger; \quad i^\dagger = -i; \quad \mathrm{M}^\dagger = (\mathrm{M}^{\mathrm{T}})^*$$

We now check Hermiticity:

$$\hat{H}^\dagger = \left(\frac{\hat{\boldsymbol{p}}^2}{2m}\right)^\dagger + \left(\frac{\boldsymbol{\mathcal{A}}^2}{2m}\right)^\dagger - \left(\frac{\boldsymbol{\mathcal{A}}\cdot\hat{\boldsymbol{p}}}{m}\right)^\dagger + \left(\frac{i\hbar}{2m}\boldsymbol{\nabla}\cdot\boldsymbol{\mathcal{A}}\right)^\dagger \tag{2.72}$$

$$= \frac{\hat{\boldsymbol{p}}^2}{2m} + \frac{\boldsymbol{\mathcal{A}}^2}{2m} - \frac{\hat{\boldsymbol{p}}\cdot\boldsymbol{\mathcal{A}}}{m} - \frac{i\hbar}{2m}(\boldsymbol{\nabla}\cdot\boldsymbol{\mathcal{A}}) \tag{2.73}$$

Note: $\boldsymbol{\nabla}$ here acts as a derivative operator, not as a momentum operator.

Now:

$$\hat{\boldsymbol{p}}\cdot\boldsymbol{\mathcal{A}}\,\psi = -i\hbar\boldsymbol{\nabla}\cdot(\boldsymbol{\mathcal{A}}\,\psi) \tag{2.74}$$

$$= -i\hbar\,(\boldsymbol{\nabla}\cdot\boldsymbol{\mathcal{A}})\,\psi - i\hbar\boldsymbol{\mathcal{A}}\cdot(\boldsymbol{\nabla}\psi) \tag{2.75}$$

$$= (-i\hbar(\boldsymbol{\nabla}\cdot\boldsymbol{\mathcal{A}}) + \boldsymbol{\mathcal{A}}\cdot\hat{\boldsymbol{p}})\,\psi \tag{2.76}$$

Therefore:
$$\hat{\boldsymbol{p}}\cdot\boldsymbol{\mathcal{A}} = -i\hbar(\boldsymbol{\nabla}\cdot\boldsymbol{\mathcal{A}}) + \boldsymbol{\mathcal{A}}\cdot\hat{\boldsymbol{p}} \tag{2.77}$$

Now substitute this expression back into $(\hat{H}^\dagger)$:

$$\hat{H}^\dagger = \frac{\hat{\boldsymbol{p}}^2}{2m} + \frac{\boldsymbol{\mathcal{A}}^2}{2m} - \frac{1}{m}\,(-i\hbar\boldsymbol{\nabla}\cdot\boldsymbol{\mathcal{A}} + \boldsymbol{\mathcal{A}}\cdot\hat{\boldsymbol{p}}) - \frac{i\hbar}{2m}\boldsymbol{\nabla}\cdot\boldsymbol{\mathcal{A}} \tag{2.78}$$

$$= \frac{\hat{\boldsymbol{p}}^2}{2m} + \frac{\boldsymbol{\mathcal{A}}^2}{2m} + \frac{i\hbar}{m}\boldsymbol{\nabla}\cdot\boldsymbol{\mathcal{A}} - \frac{\boldsymbol{\mathcal{A}}\cdot\hat{\boldsymbol{p}}}{m} - \frac{i\hbar}{2m}\boldsymbol{\nabla}\cdot\boldsymbol{\mathcal{A}} \tag{2.79}$$

$$= \frac{\hat{\boldsymbol{p}}^2}{2m} + \frac{\boldsymbol{\mathcal{A}}^2}{2m} - \frac{\boldsymbol{\mathcal{A}}\cdot\hat{\boldsymbol{p}}}{m} + \underbrace{\frac{i\hbar}{2m}\boldsymbol{\nabla}\cdot\boldsymbol{\mathcal{A}}} \tag{2.80}$$

Now combining:
$$\frac{2i\hbar}{2m}\boldsymbol{\nabla}\cdot\boldsymbol{\mathcal{A}} - \frac{i\hbar}{2m}\boldsymbol{\nabla}\cdot\boldsymbol{\mathcal{A}} = \frac{i\hbar}{2m}\boldsymbol{\nabla}\cdot\boldsymbol{\mathcal{A}} \tag{2.81}$$

$$\boxed{\hat{H}^\dagger = \hat{H}}$$

This confirms that $\hat{H}$ is Hermitian.

2.9.3 Total Energy & Conservation of Energy Test

Total energy and the conservation of energy test are useful tools in simulations, as they demonstrate that both imaginary time and real time evolution methods are correctly implemented and numerically stable. The total energy, where the three energy components—kinetic energy (KE), potential energy (PE), and interaction energy (IE)—are calculated separately is

$$E = \int dV \left(\frac{\hbar^2}{2m} |\nabla \Psi|^2 + V_{\text{ext}} |\Psi|^2 + \frac{g}{2} |\Psi|^4 \right), \tag{2.82}$$

where V_{ext} is the external harmonic trapping potential and g is the interaction strength. The kinetic energy term, involving $|\nabla \Psi|^2$, can be evaluated in k-space using a Fourier transform. The result is:

$$KE = \int dK \left(\frac{\hbar^2 k^2}{2m} |\tilde{\Psi}(k)|^2 \right), \tag{2.83}$$

where $\tilde{\Psi}(k)$ is the Fourier transform of $\Psi(x, y)$ in 2d and with the normalization to the total number of atoms N given by

$$\int d^2\boldsymbol{r} \, |\tilde{\Psi}(k)|^2 = N. \tag{2.84}$$

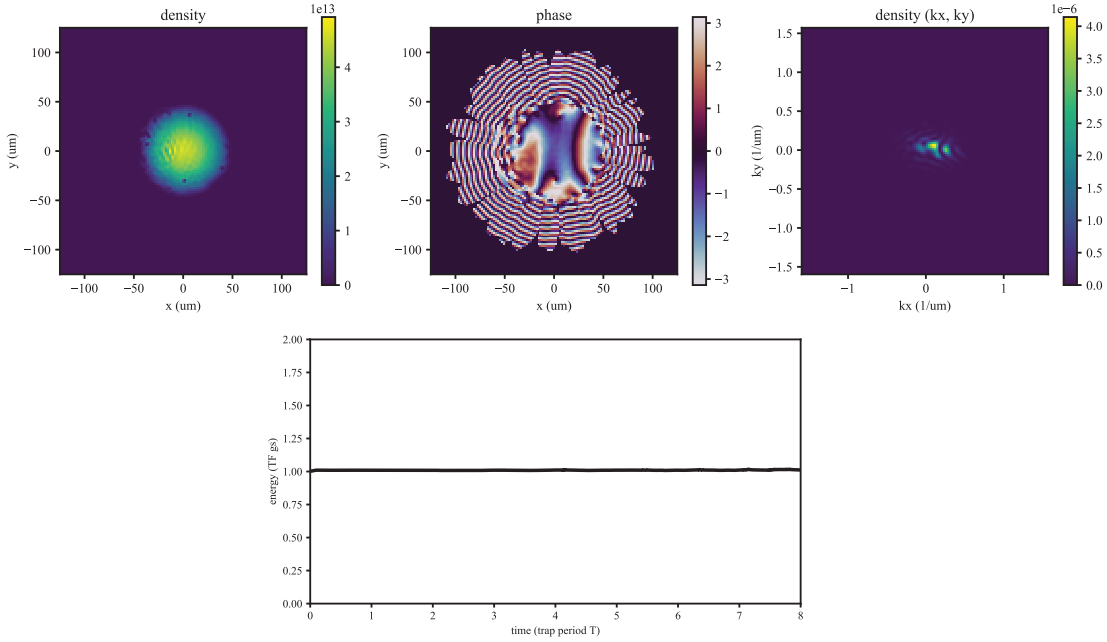

Figure 2.6: Magnetically insensitive BEC subjected to a sudden random magnetic field. The 2d density in real space, the phase profile, and the 2d density in momentum space are shown at time $t = 8T$, where T is the trap period. Here, the simulation demonstrates how vortices nucleate at the system's edge. Additionally, the total energy is plotted over the duration of the real time evolution, demonstrating energy conservation and the stability of the simulation.

Fig. 2.6 shows the 2d density in real space, momentum space, and phase profile of a magnetically insensitive BEC subjected to a sudden random magnetic field, evaluated at time $t = 8T$, where T is the trap period. Here, the simulation demonstrates how vortices nucleate at the system's edge. With continued time evolution, the vortices will fully enter to an equilibrium density. For the simulation, the wavefunction was normalized after every time step. Note that in the case of the physical system, the vortices will eventually decay along with the atom number. Additionally, the total energy is shown over the duration of the real time evolution, demonstrating energy conservation and confirming the stability of the simulation. The random magnetic field was generated using a Fourier series with periodic boundary condi-

tions. The magnetic field strength is defined as the standard deviation from the average, where $\mathcal{B}_0 = 0.0394\ mw = 0.2962\mathcal{B}_c$ and $\mathcal{B}_c = 0.1329\ mw$. Some simulation parameters include: atom number $= 1.5 \times 10^5$, trap frequencies $= 2\pi \times (10, 10, 4.8)$ kHz, chemical potential $\mu = h \times 901.9$ Hz, Thomas–Fermi radii $= 45.8\,\mu$m, healing length $= 254$ nm, interaction strength $g_{2d} = 0.17\,\hbar^2/m$, and the Kinetic energy cutoff $= 0.25\,\mu\text{m}^{-1}$. In addition, the real time evolution included cooling steps, implemented by running an imaginary time step every 50th iteration.

Chapter 3: Experimental Setup and Measurement Techniques

This chapter presents an overview of the experimental techniques used for creating, manipulating and probing BECs in the laboratory, which allows us to directly image quantum effects and perform quantum simulation experiments. Laser cooling and trapping techniques exploit the intricacies of atomic physics and light-matter interactions through a sequence of stages: cooling atomic ensembles to ultralow temperatures where Bose–Einstein condensation occurs, trapping the atoms in various potentials, and finally performing state manipulation and detection.

The chapter begins with a review of the basic principles of laser cooling and trapping, BEC production, evaporation and state transfer, harmonic trapping in the presence of gravity and magnetic fields gradients, as they are applicable for the experiments presented in the context of this thesis and from applying the atomic physics principles from the last chapter. This chapter describes recent upgrades and changes to the apparatus only in so far as they pertain to the results presented in this Thesis. The general design and operation of the system is detailed in Ref. [52] and several successive Ph.D. theses [79–82]. During the past several years, modifications have been made, in particular regarding the xy imaging system. In addition, two upgrades have been implemented into the apparatus-the sheet trap optical system and digital micromirror device (DMD) systems-that support the experiments presented in this thesis. The chapter includes a section discussing the modifications that were

made to the xy imaging system with an overview of implementation and the example characterizations of the DMD systems. The chapter continues with an overview of the sheet trap setup and its performance. Then concludes with absorption imaging and partial transfer absorption imaging (PTAI) which set the foundation for all measurement techniques.

3.1 Towards Quantum Degeneracy

Laser cooling provides the foundation for preparing ultracold atomic ensembles in our experiments. Several stages of well-established laser and magnetic field techniques are employed to reduce the temperature of bosonic ^{87}Rb atoms, forming a cold ensemble that eventually reaches Bose–Einstein condensation through evaporative cooling in an optical dipole trap.

The cooling process relies on momentum exchange between atoms and near-resonant light. Each absorption and subsequent spontaneous emission event transfers a momentum $\hbar k_0$ to the atom, leading to a change in velocity of $v_r = \hbar k_0/m$, where $k_0 = 2\pi/\lambda$ is the laser wavevector. Because of the Doppler effect, atoms moving with velocity $\mathbf{v}$ perceive a frequency shift $\omega_D = -\mathbf{k} \cdot \mathbf{v}$, meaning only a subset of atoms remain resonant with the laser field. This velocity selectivity forms the basis of Doppler cooling [47]. While a single beam provides a one-dimensional damping force, full three-dimensional cooling requires multiple counter-propagating beams that collectively produce a velocity-dependent restoring force. The repeated scattering of photons on the cycling transition $F = 2 \rightarrow F' = 3$ of the D_2 line leads to

substantial reductions in mean atomic velocity. However, each spontaneous emission imparts a random recoil, establishing a balance between cooling and heating that defines the Doppler limit [83]:

$$T_D = \frac{\hbar \Gamma_{\text{sc}}}{2k_B}, \tag{3.1}$$

where k_B is the Boltzmann constant and Γ_{sc} the scattering rate determined by the excited-state lifetime τ through $\Gamma_{\text{max}} = 1/\tau$. In practice, we use frequency-stabilized lasers with narrow linewidths and well-defined detunings.

Zeeman Slowing. A common implementation of laser cooling is where a Zeeman slower is used to decelerate atoms emitted from the oven. A counter-propagating laser beam tuned slightly below resonance exerts a continuous slowing force. As atoms lose velocity, the changing Doppler shift would normally drive them out of resonance; this is compensated by a spatially varying magnetic field that shifts the atomic transition frequency, maintaining resonance along the slower [84]. Because atoms can decay into hyperfine ground states not addressed by the cycling light, a repumping beam is added to return atoms to the cooling transition.

Optical Molasses. Beyond beam slowing, laser cooling can be applied to stationary clouds of atoms. This is achieved by a pair or three orthogonal pairs of counter-propagating laser beams, detuned below resonance of the cooling transition. The resulting light field produces a velocity-dependent scattering force analogous to viscous damping, which slows atomic motion in each respective direction. By optimizing the detuning and intensity balance of the beams, the atoms can be cooled to temperatures approaching the Doppler limit.

Sub-Doppler Cooling. Further temperature reduction is achieved using polarization-gradient cooling (PGC), which exploits both the internal spin structure of the atoms and spatial variations in light polarization [85]. In our setup, we use a $\sigma^+\sigma^-$ configuration, where circularly polarized counter-propagating beams induce optical pumping between Zeeman sublevels such that atoms are preferentially driven into states that absorb light from the beam opposing their motion, thereby enhancing the slowing effect [47].

Magneto-Optical Trap. The final stage of laser cooling combines magnetic and optical forces in a magneto-optical trap (MOT). Here, a quadrupole magnetic field generated by large anti-Helmholtz coils introduces position-dependent Zeeman shifts, while six circularly polarized beams provide restoring forces toward the trap center [86]. The MOT provides both cooling and spatial confinement, producing dense, cold atomic ensembles suitable for transfer into magnetic or optical trapping potentials.

3.2 Bose–Einstein Condensate Production

The series of stages that lead to quantum degeneracy begins with ^{87}Rb atoms emitted from a dual Rb–K oven, that then travel through a chilled cold cup and differential pumping tube to the main chamber on the experimental apparatus. The longitudinal velocities of the atoms are then reduced by a Zeeman slower operating on the $|F = 2, m_F = 2\rangle \rightarrow |F' = 3, m_F = 3\rangle$ cycling transition, driven by a counter-propagating laser beam. Repumping light, resonant with the $|F = 1\rangle \rightarrow |F' = 2\rangle$

transition, prevents optical pumping into dark states. Slower and repumper laser beams are approximately 6 mW and 2.7 mW respectively and provide a flux of atoms to the experimental vacuum chamber.

Slowed atoms are captured in a MOT where they are cooled and spatially confined. The MOT is formed by three orthogonal beam pairs and a quadrupole magnetic field generated by a pair of large coils in an anti-Helmholtz configuration providing $B_z^{'} \approx 13$ G/cm. The MOT beam pairs are slightly detuned from the cooling transition $|F = 2\rangle \rightarrow |F' = 3\rangle$, and weak repumper light is present to recycle atoms from the $F = 1$ manifold. Atoms are loaded into the MOT for 1-4s, depending on atom number and stability conditions.

Once the MOT reaches steady-state population, the magnetic fields and slowing light are switched off, and additional cooling and optical pumping of the atoms takes place via optical molasses and $\sigma^+\sigma^-$ PGC. Increasing the detuning of the cooling beams while lowering the repump intensity achieves sub-Doppler temperatures and pumps atoms predominantly into the $F = 1$ ground state. A short repump pulse then prepares atoms in the $|F = 1, m_F = -1\rangle$ Zeeman sublevel, and any residual $F = 2$ population is removed by resonant light.

The atoms are subsequently loaded into a quadrupole magnetic trap generated by the anti-Helmholtz coils. The trap current is ramped to compress the cloud and enhance collision rates, after which an optical dipole trap (ODT), formed by the intersection of two 1064 nm laser beams, is ramped on. Forced radio-frequency evaporation removes the most energetic atoms, cooling the sample further as it rethermalizes. During this stage, the quadrupole magnetic trap is gradually decom-

pressed while a small bias field shifts the magnetic-field zero toward the dipole trap center, enabling efficient transfer of atoms into the optical potential.

Final evaporative cooling is performed entirely in the ODT. The magnetic field gradient is just strong enough to counteract gravity, and the optical power is dynamically reduced to lower the trap depth and modify the confinement geometry. Completion of this evaporation sequence yields a ^{87}Rb BEC in the $|F = 1, m_F = -1\rangle$ internal state confined within the ODT.

3.2.1 Evaporation and State Transfer

For certain types of experiments—in particular, those discussed in Chapters 6–8—a BEC in the $|F = 1, m_F = 0\rangle$ internal state is desired. This state is prepared using a resonant RF pulse just before the final evaporation stage. Following this transfer, magnetic field gradients are applied to tilt the trap in a state-dependent way, such that atoms in the magnetically sensitive $|F = 1, m_F = \pm 1\rangle$ states are selectively ejected from the trap by an additional magnetic gradient *kick*. In contrast, the $|F = 1, m_F = 0\rangle$ population—being magnetically insensitive—remains stably confined. All gradients are then rapidly ramped off, marking the end of the evaporation sequence. The state-dependent ejection relies on differential forces arising from the linear Zeeman shift: $m_F = \pm 1$ states experience position-dependent potentials in the magnetic field gradient, while the $m_F = 0$ state does not. This separation mechanism enables spin filtering and removal, ensuring that only atoms in the desired internal state remain in the trap. Transfer efficiency to $|F = 1, m_F = 0\rangle$, along with

the magnetic field gradient protocol, was consistently around 70% of the total atom number in the initial $|F = 1, m_F = -1\rangle$ state. Therefore this procedure allows for a robust 20% increase in transfer on top of the 50% with the Raman pulse.

In practice, an additional hold time in the ODT follows this stage to allow residual magnetic fields to decay. For Raman-dressed experiments, this hold time was approximately 750 ms and was tuned such that residual fiels were not present when loading atoms into the Raman-dressed states.

The following section presents a simulation of the optical dipole trap, incorporating additional terms to model the effects of gravity and magnetic field gradients on the trap curvature. These additions help visualize and quantify how the trapping potential becomes spin-dependent, as shown in Fig. 3.1, and offer further insight into our state preparation method. In particular, the simulation reveals how the combination of gravitational tilt and magnetic Zeeman shifts alters both the position of the trap minimum and the trap frequency in a spin-selective way—reinforcing the mechanism by which atoms in unwanted m_F states are spatially separated and removed, while $m_F = 0$ atoms remain confined.

3.2.2 Trapping in the Presence of Gravity and Magnetic Gradients

To model the effective confinement experienced by atoms in a red-detuned optical dipole trap[1], we consider the total potential along the vertical direction z, where

[1]The sign of the dipole potential U depends on the detuning Δ of the laser relative to the atomic resonance. For red-detuned light ($\Delta = \omega - \omega_0 < 0$), the potential is attractive ($U < 0$), pulling atoms toward high-intensity regions. Conversely, blue-detuned light ($\Delta = \omega - \omega_0 > 0$) results in a repulsive potential ($U > 0$), pushing atoms toward intensity minima. These properties underlie the design of optical dipole traps.

gravity and magnetic field gradients can significantly modify the trap depth and curvature. The optical dipole potential produced by a Gaussian beam of power P and waist w_0 is given by [19]:

$$U(z) = -\frac{3\pi c^2 \Gamma}{2\omega_0^3} \left(\frac{1}{\Delta}\right) I(z), \tag{3.2}$$

where the intensity profile of the beam is

$$I(z) = \frac{2P}{\pi w_0^2} \exp\left(-\frac{2z^2}{w_0^2}\right), \tag{3.3}$$

with Δ being the detuning from atomic resonance, Γ the natural linewidth, and ω_0 the resonant frequency. Assuming harmonic confinement near the trap center, the axial trap frequency ω_z is extracted from the curvature of the potential at $z = 0$ via:

$$U(z) \approx U(0) + \frac{1}{2} m \omega_z^2 z^2 \quad \Rightarrow \quad \omega_z = \sqrt{\frac{1}{m} \left.\frac{d^2U}{dz^2}\right|_{z=0}} \tag{3.4}$$

where m is the atomic mass. In simulations, this is evaluated using a second-order central difference method where derivatives are approximated by using function values at points symmetrically around the target point. This approach was used to compute the trap frequency since it provides an accurate and stable estimate of the curvature of $U(z)$ at z_0.

To account for gravitational sag, we add the linear potential due to gravity:

$$U_g(z) = -mgz, \tag{3.5}$$

where g is the gravitational acceleration. In the presence of a magnetic field gradient B', spin-dependent potentials arise from the Zeeman effect, as was discussed in Section 2.2. Recall, for an atom in a hyperfine state with magnetic quantum number m_F, the contribution is

$$U_B(z) = \mu_B g_F m_F B' z, \tag{3.6}$$

where μ_B is the Bohr magneton, the Landé g-factor $g_F = -1/2$ and $m_F \in \{-1, 0, +1\}$. The total potential is then:

$$U(z) = U(z) - mgz + \mu_B g_F m_F B' z. \tag{3.7}$$

The direction and magnitude of the magnetic term determine whether the magnetic gradient enhances or cancels the gravitational force. In particular, gravity is exactly canceled when:

$$\mu_B g_F m_F B' = mg \quad \Rightarrow \quad B' = \frac{mg}{\mu_B g_F m_F}. \tag{3.8}$$

In practice, we apply smaller gradients to enhance their removal, not suspend them. In addition, our protocol is a bit more involved, however, this illustrates the physical basis for using spin-dependent forces to eject magnetically sensitive atoms, while retaining a well-confined $m_F = 0$ population.

Figure 3.1 visually illustrates the physical basis for these spin-dependent potentials and forces that can separate or selectively manipulate different m_F states in the trap. (a) Illustrates how gravity introduces a uniform downward tilt to the trapping

[2]The plotted power value of 5 W is significantly lower than the optical powers typically used in the experiment. This choice was made to exaggerate the effects of gravity and magnetic gradients

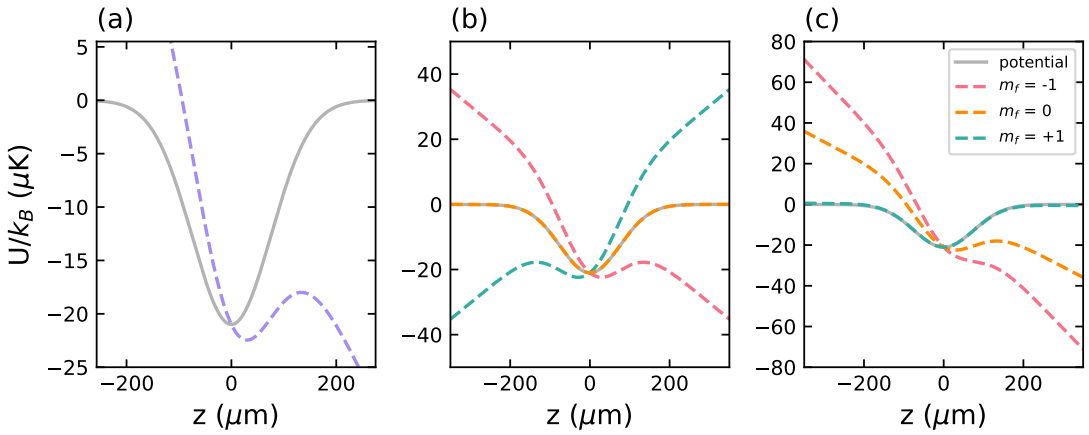

Figure 3.1: Trapping potential in the presence of gravity and magnetic field gradients. The potential is produced by a Gaussian beam with waist $w_0 = 150$ μm and power $P = 5$ W.[2] (a) Illustrates how gravity introduces a uniform downward tilt to the trapping potential and reduced confinement due to gravitational sag. Here, it's clear that the trapping potential is the solid gray curve and the potential modified by gravity is the dashed slateblue curve. (b) Trapping potential combined with a magnetic field gradient B' for atoms in magnetic sublevels $m_F = \{-1, 0, +1\}$. The gradient induces a linear potential shift in a state-dependent manner for $m_F = \pm 1$, modifying both the trap depth and curvature. (c) Illustrates the combined effect of gravity and magnetic gradients producing distinct potential minima, i.e. effectively modifying the trap center, for each spin state—leading to spatial separation, differential confinement, and modified curvature. Note: Trap frequencies are extracted from the curvature near $z = 0$.

potential, reducing confinement. (b) Demonstrates how the magnetic field gradient linearly shifts the potential in a state-dependent manner for $m_F = \pm 1$, with $m_F = 0$ experiencing no Zeeman shift. (c) Illustrates the combined effect of gravity and magnetic gradients producing distinct potential minima, i.e. effectively modifying the trap center, for each spin state—leading to spatial separation, differential confinement, and modified curvature. These differential potentials form the foundation for selectively removing unwanted spin components after state preparation, as detailed in the preceding evaporation and state transfer section.

for visual clarity and improved interpretability of the plots.

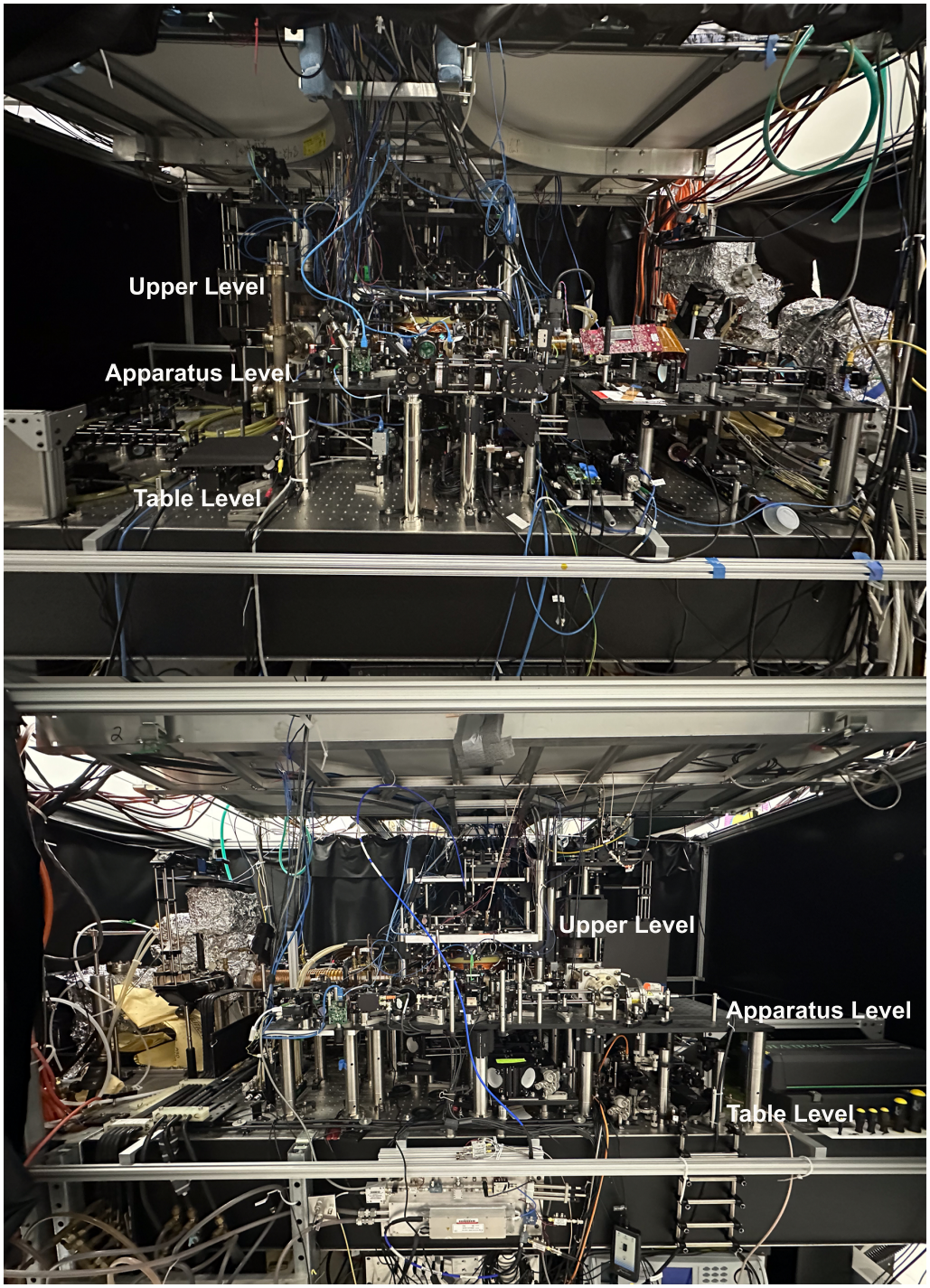

Figure 3.2: Overview of the RbK apparatus.

3.3 Experiment Overview

The RbK experimental apparatus was designed about 19 years ago and is comprised of many subsystems, performing key functions, that all operate and work together-in harmony- to form a robust experiment that has performed an amazing and diverse array of experiments by amazing Captains and ever-changing teams. To all future Captains—the essence of taking something for granted often reveals itself in its absence. Always appreciate achieving a BEC. Afterall, the laboratory is the coldest place in the universe and sometimes, *cool* things happen.

The apparatus can be conceptually grouped into the following major subsystems:

Vacuum System: The vacuum system consists of three regions: the oven chamber, the differential pumping section, and the science chamber. These are separated by two gate valves—one pneumatic and one manual—and are each maintained by independent ion pumps with local pressure monitoring. The oven chamber pressure is monitored by an ion gauge. Dual species atom sources (^{87}Rb and supposedly K) are housed in individual ovens in the oven chamber where they are thermally regulated and controlled using four PID temperature controllers. A critical component in maintaining the system is the cold cup, held between -25 C$^\circ$ and -40 C$^\circ$ by a two-stage thermoelectric cooler (TEC). Heat from the TEC is removed using a liquid recirculating chiller. Recently, we integrated an interlock circuit that ensures that the current supplying the TEC will be shut if the TEC temperature rises above

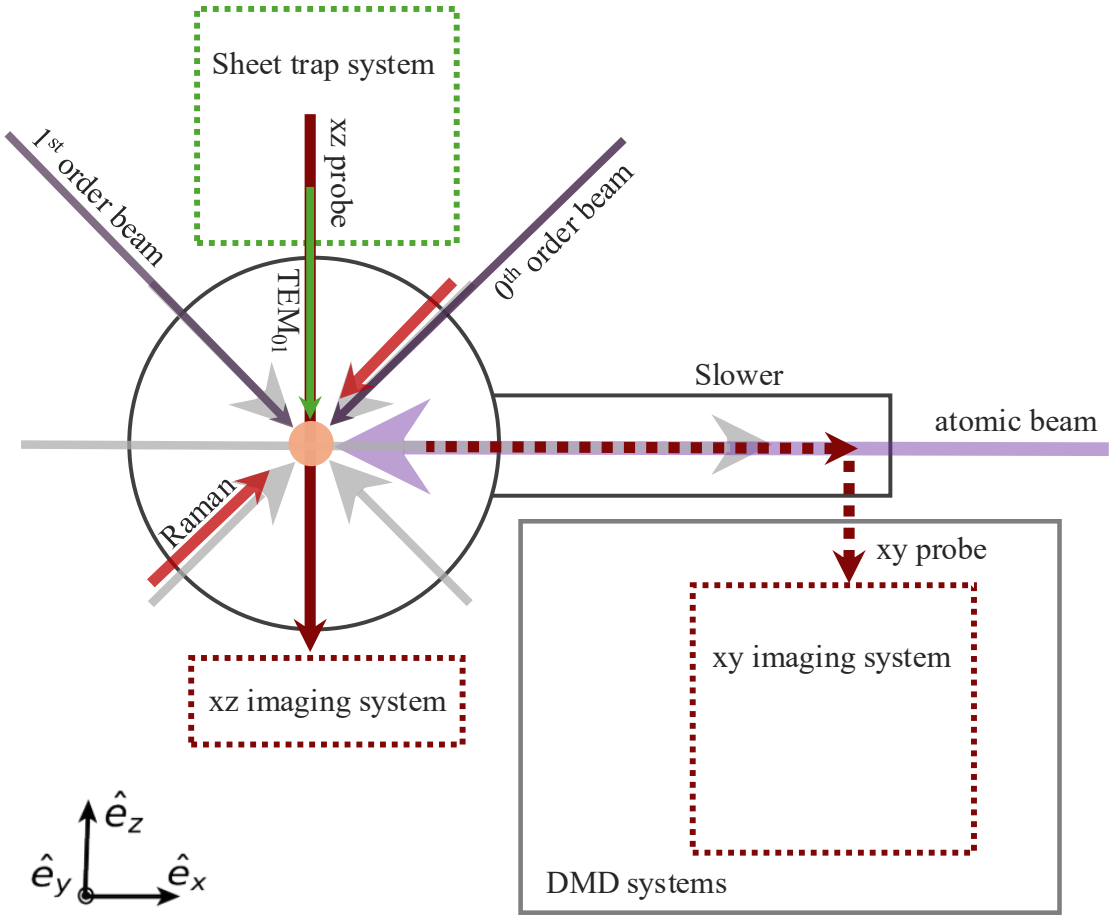

Figure 3.3: Schematic of the experimental apparatus highlighting laser and probe beam geometries, and the placement of the xy imaging, sheet trap and digital micromirror device (DMD) subsystems.

an *alarm* value. This measure was taken due to an increase in power outages all leading to catastrophe where the chiller stops cooling and the TEC overheats causing the water system to heat and melt the water hoses. Meanwhile Rb atoms heat up off the cold cup and contaminate the vacuum system. This vital cooling system is now effectively protected.

Magnetic Field Systems: The Zeeman slower magnet runs along the x-axis and is used to decelerate atomic beams. For static magnetic fields, three orthogonal pairs

of Helmholtz coils are used to generate bias (quantization) fields, while an anti-Helmholtz pair along the z-axis provides magnetic gradients for the MOT, magnetic trap, and Stern Gerlach imaging. Additional gradient cancellation coils offer fine-tuning. For dynamic field control, a pair of RF coils mounted above the chamber enables evaporative cooling and RF-driven state transitions. Microwave transitions between the $F = 1$ and $F = 2$ hyperfine levels are driven via a horn antenna. The water cooling system for all water-cooled coils has a breakout panel and pump system where the chilled water is delivered by the NIST chiller plant.

Laser Systems and Optical Delivery: Laser systems support majority of the stages of the experimental sequence. These include:

- A slowing beam and repumper aligned along the Zeeman slower.
- Six MOT beams, with corresponding mirrors on flipper mounts, intersecting in the science chamber.
- Imaging probe beams aligned along both the xy and xz planes.
- Optical dipole trap beams for trapping and lattices.
- Raman beams for driving Raman transitions.
- 790 nm and 777 nm beams for DMD applications.

Optical components for beam shaping, steering, and modulation are distributed throughout the system, and two DMD enable spatial light modulation for advanced quantum control.

Microwave Horn Antenna: A microwave horn is employed to drive transitions, between the $F = 1$ and $F = 2$ hyperfine states, via frequency pulses. The horn itself is located above the top of the science chamber and is controlled via a network of electronics and frequency generator. The power supply is located across the lab, to reduce disturbance to the experiment.

3.3.1 Control System

Experiment timing, control, and data acquisition are managed using the `labscript` suite [87], a modular control framework that allows coordinated operation of hardware distributed across multiple computers. All device actions are synchronized via pseudoclock signals, which are generated by a central digital pulse generator and trigger updates according to precompiled instructions.

Experimental sequences are defined in Python scripts, which specify the timing, parameters, and global settings for each experimental shot. Each sequence results in an HDF5 file containing the full set of control instructions. As the shot proceeds, acquired data (e.g.,images) are appended to this same file for streamlined analysis. The core timing system is based on a SpinCore PulseBlaster USB device, which generates digital timing signals (pseudoclock lines) to coordinate all subordinate devices. Analog and additional digital outputs are provided by:

- Three National Instruments PCI-6733 analog output cards,
- Two NI USB-6229 multifunction devices,
- One NI USB-6343 multifunction I/O device.

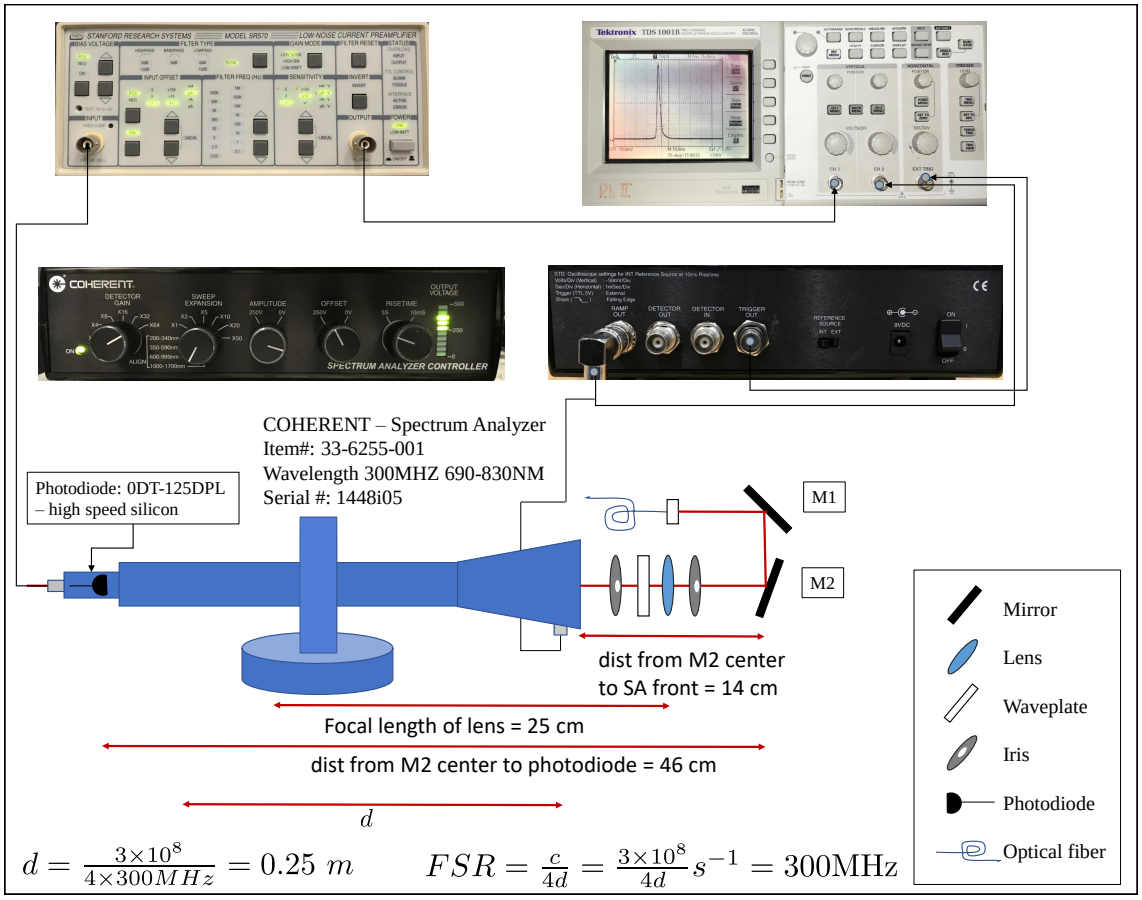

Figure 3.4: Spectrum analyzer for laser frequency monitoring and diagnostics.

3.4 Laser Systems

The RbK experiment relies on a suite of laser systems for cooling, trapping, manipulating, and imaging atomic systems. Our setup utilizes three primary lasers with tunable wavelengths centered around 780 nm, near the ^{87}Rb D_2 transition: the master, repump, and MOT/cooling lasers. The master laser, a Toptica DL Pro, is frequency-locked via saturated absorption spectroscopy to the crossover peak between the $F = 2 \rightarrow F' = 2$ and $F' = 3$ transitions. Its primary function is to provide a frequency reference for the repump and MOT/cooling lasers. The repumper, implemented with a Toptica DL 100, optically pumps atoms out of the $F = 1$ ground

state via the $F = 1 \rightarrow F' = 2$ transition, providing light for the slower repump beam, the MOT, and imaging. As of 2025, both the master and repump lasers are locked via a DigiLock setup, controlled through a computer interface. For cooling, the MOT, and imaging probe beams (xy: down-going, up-going and xz), a Toptica TA Pro tapered amplifier system is utilized and operates near the $F = 2 \rightarrow F' = 3$ transition. This laser is locked via a servo control system.

For all of the primary lasers, the Raman laser, and the miscellaneous TA 100 laser, optical pick-offs are sent to a spectrum analyzer to monitor their frequency components and allow for diagnostics. Figure 3.4 illustrates the schematic of the spectrum analyzer setup. Note: it is imperative that the BNC cable plugged into the back is not bumped and a permanent note has been placed near the location. The engineering design is flawed as the photodiode is mounted in such a way, that it's almost asking to be damaged. This documentation is added here as a reference and in completeness with the actual settings, for the next poor soul who may be on the mission of getting a signal. Also note, oftentimes a poor signal is typically due to the fiber input.

The optical dipole trap utilizes one or two fiber lasers operating at 1064 nm: an IPG YDL-10-LP, commonly referred to as the ODT laser, and an IPG YAR-10K-1064-LP-SF fiber amplifier, referred to as the lattice laser. For most experiments described in this thesis, only the ODT laser was used to create a crossed ODT configuration where an acousto-optic modulator (AOM) was used to generate the 0th and 1st order beams for the trap. However, in the magnetic lattice experiments discussed in Ch. 6, both fiber lasers were employed. This decision was motivated

by poor coatings, or lack there of, on the viewports allowing the beams to enter the science chamber on the apparatus, which caused retro-reflections of the 1064 nm light and unintentionally formed a standing-wave optical lattice. To eliminate this unwanted effect, the lattice laser, ironically, was intentionally modified to operate with a multi-mode—resolving the issue and serving as the second beam for the optical dipole trap.

The Raman beams and the LuxBeam DMD beam, are generated by a titanium-doped sapphire laser (Coherent MBR 110), which is pumped by a Verdi V10 diode-pumped solid-state Nd YAG laser. The pump laser produces a 532 nm beam through frequency doubling of the 1064 nm Nd YAG output using a nonlinear crystal. The Ti Sapphire laser offers broad wavelength tunability and was operated at approximately 790.022 nm, with power output ranging from 1-1.5W, for the experiments discussed throughout this thesis.

The sheet trap system utilizes a Verdi V10 laser, that provides enhanced confinement along the z-axis. Additionally, the DLP LightCrafter DMD, utilizes a Toptica TA 100 laser, initially acquired for use near 780 nm, but is operated at 777 nm for creating repulsive trapping, such as box traps or miscellaneous applications such as potentials for soliton experiments [88].

3.5 Magnetic Field Systems

Our experimental apparatus incorporates a comprehensive magnetic field infrastructure that supports atomic slowing, trapping, coherent state manipulation, and

imaging techniques. The system integrates multiple sets of electromagnet coils, each designed for specific field geometries and operational roles, and is complemented by servo-controlled power supplies, monitoring electronics, and water-cooling systems where applicable.

Zeeman Slower and Reverse Coils. The Zeeman slower contains dedicated coils to produce the required magnetic field profile for atomic deceleration.

Quadrupole Coils. A pair of anti-Helmholtz coils generate a quadrupole magnetic field with a zero-field center. These coils are used for the MOT, magnetic trapping, and Stern–Gerlach imaging. The anti-Helmholtz configuration consists of two identical coils separated by a distance equal to the coil radius, with equal and opposite currents producing a gradient along the central axis.

Bias Coils. Three orthogonal pairs of Helmholtz coils produce approximately uniform fields along $\hat{x} + \hat{y}$, $\hat{x} - \hat{y}$, and $\hat{z}$. Each pair consists of two identical coils separated by a distance equal to the coil radius. These fields define quantization axes, set Zeeman shifts, and stabilize resonance conditions for RF and Raman transitions.

RF Coils. A pair of coils positioned above the chamber's bucket window generates an oscillating magnetic field along $\hat{x}$, driven by RF signals for RF evaporation and coherent manipulation. Each coil is composed of two loops and is powered by a Mini-Circuits LZY-22+ amplifier.

Gradient Compensation Coils. Two additional coil sets provide fine adjustment of residual field gradients. One set controls $\partial B_z/\partial z$ and the other $\partial B_{xy}/\partial z$. These coils are held at constant current during experiments and are not ramped dynamically, i.e. they are manually controlled.

Power Supplies and Control Electronics. Each coil set is powered by an individual power supply and servo, allowing for independent adjustment of each coil set while maintaining stability during experimental sequences:

Zeeman Slower and Reverse Coils: Kepco ATE6-100M unipolar supply, 100 A.

Quadrupole Coils: Agilent 6690A unipolar supply, 440 A, with current regulated via a custom-built transistor bank and servo. Operational setting are 300 A / 15 V.

Bias Coils: Kepco BOP20-20M bipolar supplies, 20 A each, regulated with home-built current servos.

3.5.1 Magnetic Field Stabilization and Calibration

Stability of the bias magnetic field is critical in many experiments to maintain precise detuning for RF and Raman transitions. However, ambient magnetic field drifts—often caused by external activity—can shift these transitions from resonance. There are two protocols, passive or closed-loop feedback, to evaluate resonance condition of the bias field. Both protocols perform shot-by-shot calibration using partial transfer absorption imaging (which is discussed in the Imaging Section 3.10.2). Two microwave pulses, one with $\delta > 0$ and the other with $\delta < 0$, are applied on a hyperfine ground-state transition within the $F = 1 \rightarrow F = 2$

manifold, such as $|F = 1, m_F = -1\rangle \rightarrow |F = 2, m_F = -2\rangle$. While other transitions—e.g., $|F = 1, m_F = -1\rangle \rightarrow |F = 2, m_F = 0\rangle$—could be used, the stretched-state transition offers enhanced magnetic sensitivity because the initial and final states experience Zeeman shifts of opposite sign. Images are taken without repump light to measure only transferred atoms after each pulse, where the number of atoms in each image is compared. When populations are equal, the bias field is correctly calibrated. If the populations are not equal, an adjustment to the bias coil current is required for subsequent shots. If the imbalance is larger than a certain threshold, data is discarded. This protocol is the passive method and is the exact calibration scheme employed in Refs. [37, 89]. Although this scheme does not generate an error signal for closed-loop feedback, the external field is stable for certain types of experiments and on the timescale of short experimental sequences. However, many experiments require a stable magnetic field to maintain consistent physical properties between measurements [90–94], such as Raman dressed states where the magnetization and effective mass depends on the Zeeman shift [71, 95–97], and spin chains where hopping occurs between magnetically sensitive states [98]. An advantageous magnetic field drift correction method for atomic systems, i.e. closed-loop feedback protocol, was utilized in [97, 99] and a detailed description of this protocol can be found in [100].

3.5.2 RF Signal Generation

RF signals are essential for various applications in the experiment, including laser frequency control, Raman beam signal generation, and RF-driven atomic dynamics. These signals are produced using NovaTech 409-B direct digital synthesizers (DDS), each providing two dynamically updateable channels and two static channels. Only the dynamic channels are suitable for time-dependent operations such as RF evaporation or experiments requiring phase ramps. The devices support a 10 MHz external reference input, allowing cross-device phase locking—an essential requirement for magnetic lattice experiments.

3.6 Raman Optical System

The Raman laser system is designed to generate Raman beam configurations and now provides 790 nm light for the LuxBeam DMD optical setup. The laser beam originates from a Coherent MBR 110 Ti:Sapphire laser pumped by a Verdi-V10 diode-pumped solid-state laser, as described in the laser system section. Directly out of the Ti:Sapph, the beam travels through a waveplate, then polarizing beam splitter (PBS) cube, where one path is dedicated to the Raman beams and the other path is dedicated for the LuxBeam DMD optical setup. For the Raman beams, it employs two counter-propagating beams (Raman-A and Raman-C) at a wavelength of approximately 790.022 nm, with a frequency separation of $\omega_{\mathrm{RF}} = 1$ MHz. The system supports two distinct operational configurations:

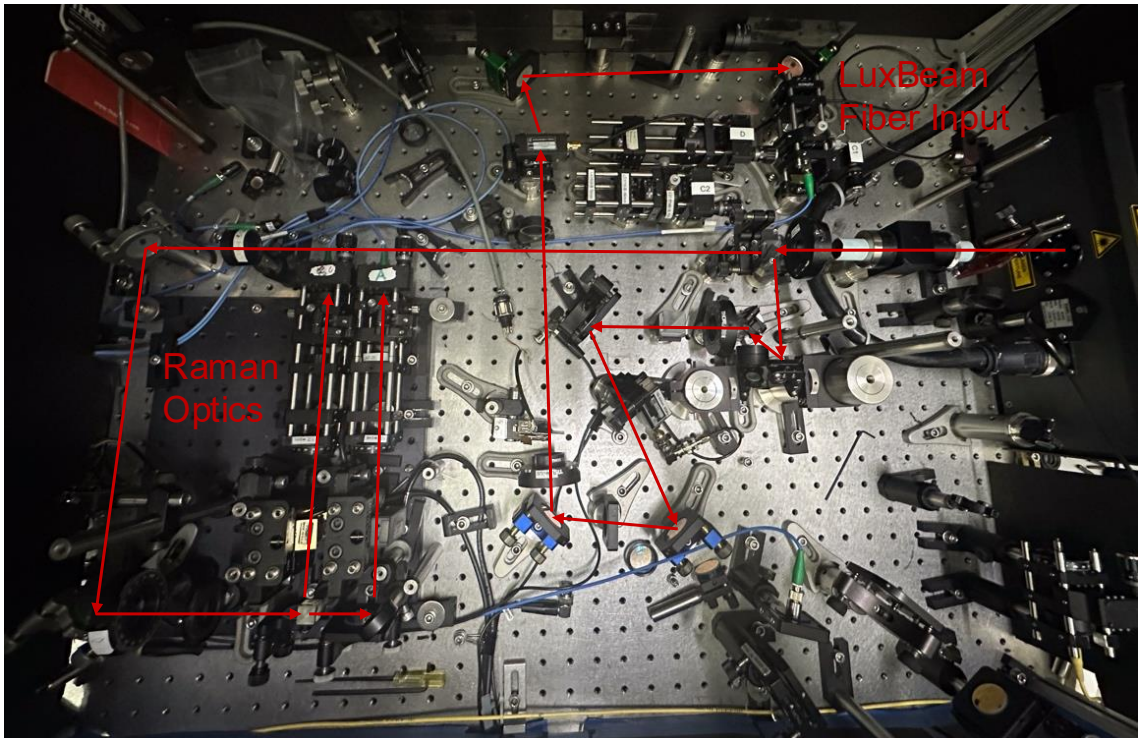

Figure 3.5: Raman System: Raman optical system and DMD 790 nm beam fiber input. Note: Raman A and C beam paths are a bit more involved, done this way for simplicity.

1. **Single-tone configuration:** one beam operates at frequency ω, while the other is shifted by ω_{RF}, i.e., $\omega + \omega_{\mathrm{RF}}$.

2. **Two-tone configuration:** frequency components ω and $\omega + \omega_{\mathrm{RF}}$ are present in each beam.

To generate the required frequency shifts for either configuration, the beam travels through a waveplate, a PBS, where the beam is split into Raman-C and Raman-A paths, and then each beam passes through an independent acousto-optic modulator (AOM), with the first-order diffracted beams coupled into optical fibers for delivery to the atoms. An 80 MHz frequency offset is added to both beams to place the AOMs within their optimal operating range, resulting in effective drive frequencies

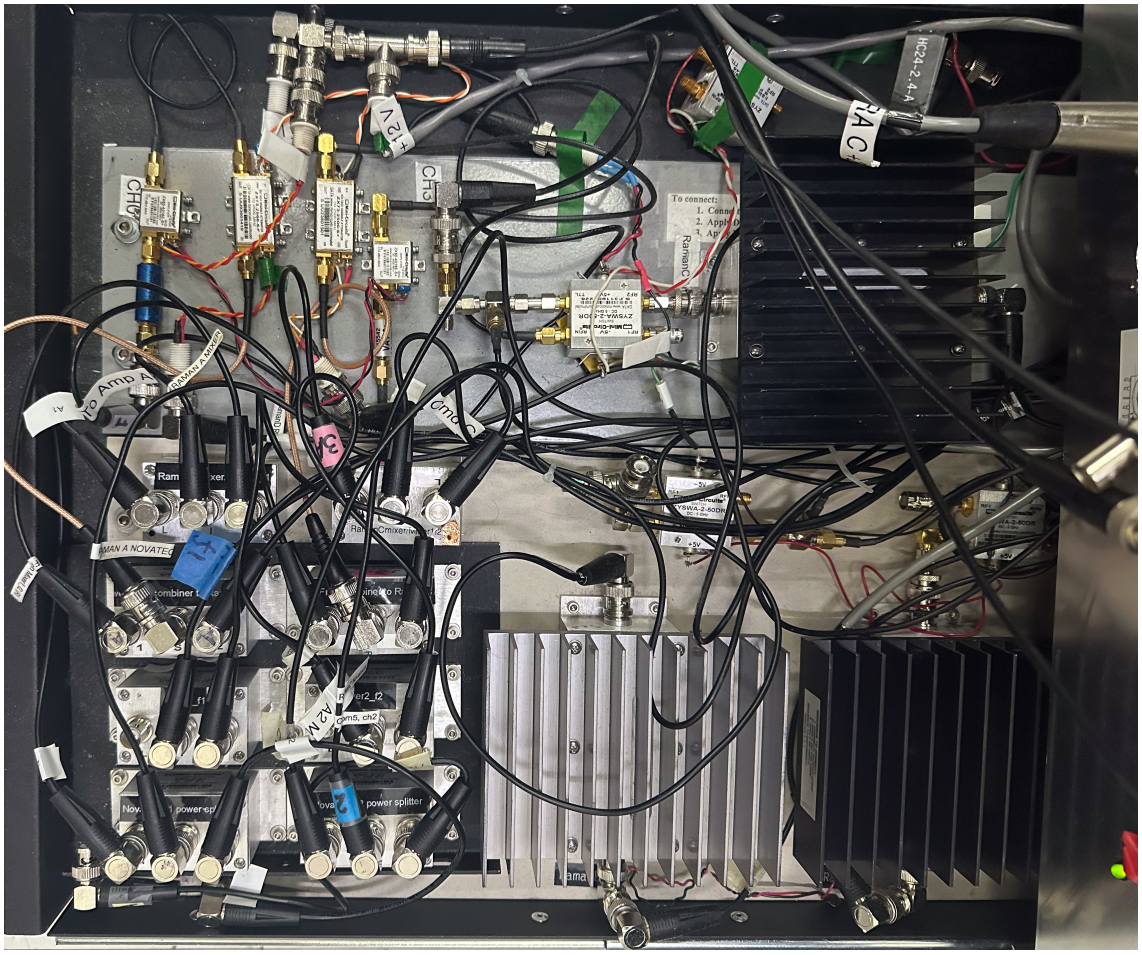

Figure 3.6: Network of RF electronic hardware for Raman laser system.

of 80 MHz and 81 MHz. For single-tone operation, Raman-A is shifted by 80 MHz and Raman-C by 81 MHz; in the two-tone configuration, each beam contains both frequency components, each requiring the appropriate subsequent frequency shifts. A network of RF hardware, illustrated in Fig. 3.6, generates and routes the RF drive signals required for both configurations. Two Novatech 409-B direct digital synthesizers (DDS) provide 80 MHz and 81 MHz outputs, f_1 and f_2, referenced to a 10 MHz clock for phase stability. Each DDS channel output is split using a Mini-Circuits ZSC-2-4+ power splitter, producing four RF signals that are sent to individual Mini-Circuits ZAD-3+ mixers. These mixers enable amplitude modu-

lation through analog output (AO) channels under computer control. The mixed signals are then recombined via additional power splitters to form two independent RF drive pairs corresponding to Raman-A and Raman-C. Each drive path includes a Mini-Circuits ZX73-2500-S+ voltage-controlled attenuator for fine power adjustment, followed by a preamplifier, an optional fixed attenuator for impedance matching, a Mini-Circuits ZYSWA-2-50DR RF switch for fast on/off control, and finally a Mini-Circuits ZHL-1-2W+ amplifier before being delivered to the AOMs. The resulting frequency components, labeled A1, A2 (Raman-A) and C1, C2 (Raman-C), form two distinct Raman channels with Rabi frequencies Ω_1 and Ω_2, which are set by the mixer control voltages. This describes the two-tone configuration, with an easy switch to the single-tone configuration, with a single Rabi frequency Ω_R, by commanding full attenuation of A2 and C2 mixers.

After exiting their fibers, each Raman beam is collimated, with its polarization adjusted using waveplates, and focused onto the atoms using a 300 mm focal-length singlet lenses, producing beam waists of approximately 150 μm at the atoms.

3.7 Imaging Systems

In ultracold atom experiments, imaging is the primary method for probing and characterizing atomic clouds. We employ resonant absorption imaging and partial transfer absorption imaging (PTAI) for time-of-flight and *in situ* measurements. The experiment features three independent imaging systems, oriented along different directions: xy/xy0, xytop, and xz.

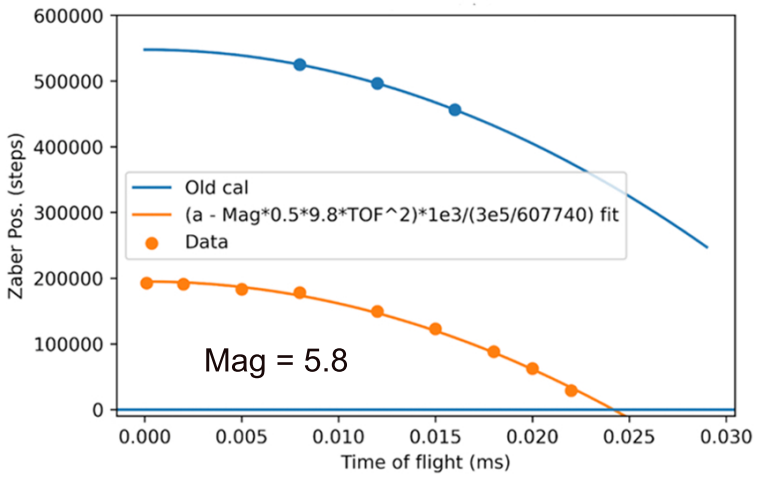

Figure 3.7: Magnification calibration for the xy imaging system after modifcations and including the optical relay telescope.

3.7.1 XY Imaging Systems

Our primary scientific imaging is performed using the *xy* imaging systems. In 2023, the *xy* time-of-flight and *xy in situ* imaging systems were modified to accommodate the LuxBeam DMD optical system, in particular, an optical relay was implemented to allow for the DMD systems' dichroics to be placed in a Fourier plane, reducing additional aberrations that arise when dichroics are located in object planes. To make this change and still maintain the previous 6× magnification, the previous $f = 500$ mm achromatic doublet was replaced with a $f = 250$ mm focal length. These two systems share most of their imaging optics, which consist of a two-lens compound objective with an effective focal length of $f = 83$ mm, coupled to an $f = 250$ mm achromatic doublet, yielding a magnification of 3×. An additional optical relay telescope, composed of $f = 100$ mm and $f = 200$ mm achromatic doublets, provides an additional 2× magnification. The resulting overall magnification is 5.8×, determined by calibrating the time-of-flight system through a Zaber stage step scan

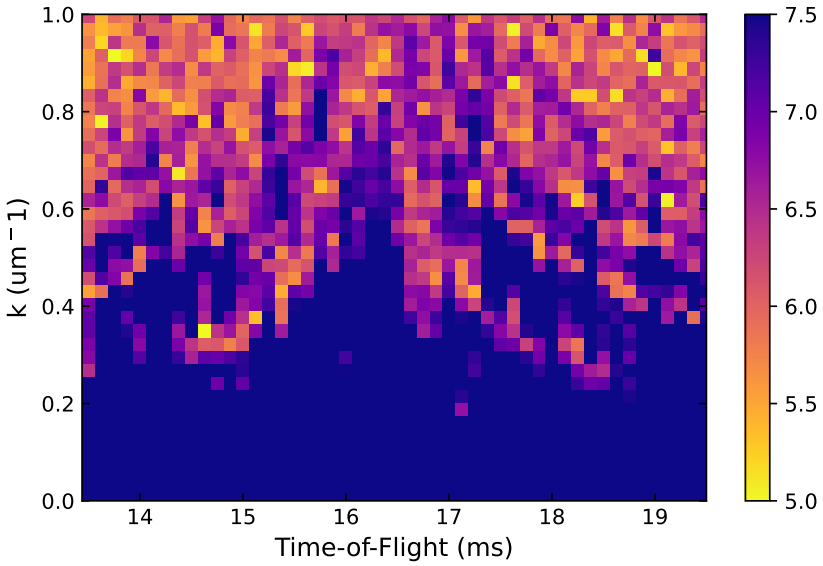

Figure 3.8: Finding optimal focus position. 1d power spectral density (PSD) of the column density along one of the trapping directions. The k-fringes give a volcano-like structure, where the focus position is extracted via the technique from Ref. [101].

(see Fig. 3.7) and confirming the modification was comparable to the previous setup. The two imaging paths are separated by a 50/50 beamsplitter cube, after which the light is directed along independent optical paths to their respective cameras. The *xy* time-of-flight camera is a Mako G-504B (CMOS sensor) mounted on a Zaber T-LSR 300B translation stage, allowing automated repositioning to match different time-of-flight durations. The *xy in situ* camera is a Point Grey Flea FL3-FW-031M (CCD sensor) mounted on a Zaber mini translation stage. Having a dedicated *in situ* camera enables the acquisition of both *in situ* and time-of-flight images within the same experimental shot. This capability is particularly valuable for monitoring magnetic field drift, performing PTAI measurements to characterize the imaging system, and studying disorder effects, as demonstrated above.

Finding the optimal focus position and/or verifying that the atomic cloud is in focus

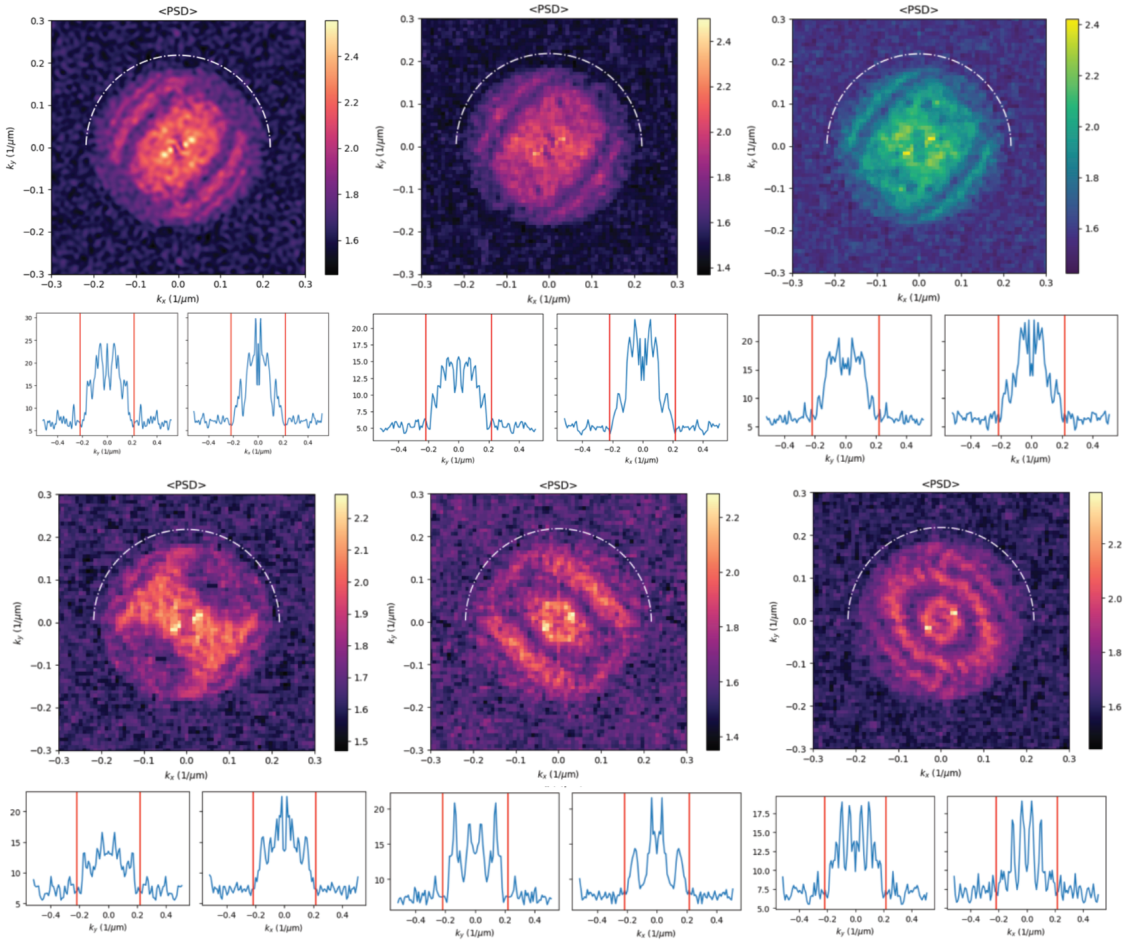

Figure 3.9: Series of average power spectral densities (PSDs) of various in situ focus positions. These PSDs can be utilized to characterize the imaging system. Here various features can be seen by eye, such as ripples, indicating out-of-focus and vacancies indicating loss of information.

can be accomplished using the technique of Ref. [101], which involves plotting the one-dimensional power spectral density (PSD) of the column density along one of the trap directions. The resulting k-space fringes produce a characteristic volcano-like structure, from which the optimal focus position can be extracted, as illustrated in Fig. 3.8.

Beyond focus optimization, characterizing the imaging system is critical for experiments—particularly those involving disorder—where precise knowledge of resolu-

tion and optical aberrations is essential for correctly interpreting spatial features in atomic density distributions. Figure 3.9 presents a series of averaged power spectral densities (PSDs) obtained for various *in situ* focus positions. These PSDs provide a powerful diagnostic tool for assessing imaging performance. Distinct features can be identified visually, such as fringe-like ripples indicating defocus and regions of missing spatial frequency content ("vacancies") corresponding to loss of information. Furthermore, the PSDs can be quantitatively modeled via joint fits to the pupil function, enabling extraction of parameters that describe the imaging system—such as even-order aberrations and astigmatism—using the techniques outlined in Ref. [102].

3.7.2 XZ Imaging System

The xz imaging system consists of a two-lens objective comprising an achromat doublet and singlet, with focal lengths of $f = 200$ mm and $f = 1000$ mm, coupled to another two-lens set composed of a singlet and achromat doublet with focal lengths $f = 750$ mm and $f = 500$ mm. After the lenses, the system contains a dichroic that directs majority of 532 nm light to a beam dump, and an additional 532 nm filter to prevent green light from the sheet trap from reaching the camera (Point Grey Flea FL3-FW-031M, CCD). The resulting overall magnification for this imaging system is 2×, determined via BEC free fall under gravity, as shown in Fig. 3.10. This imaging system is used for a variety of diagnostics. In fact, this imaging axis was vital for the implementation, day-today alignment, and operation of the sheet trap.

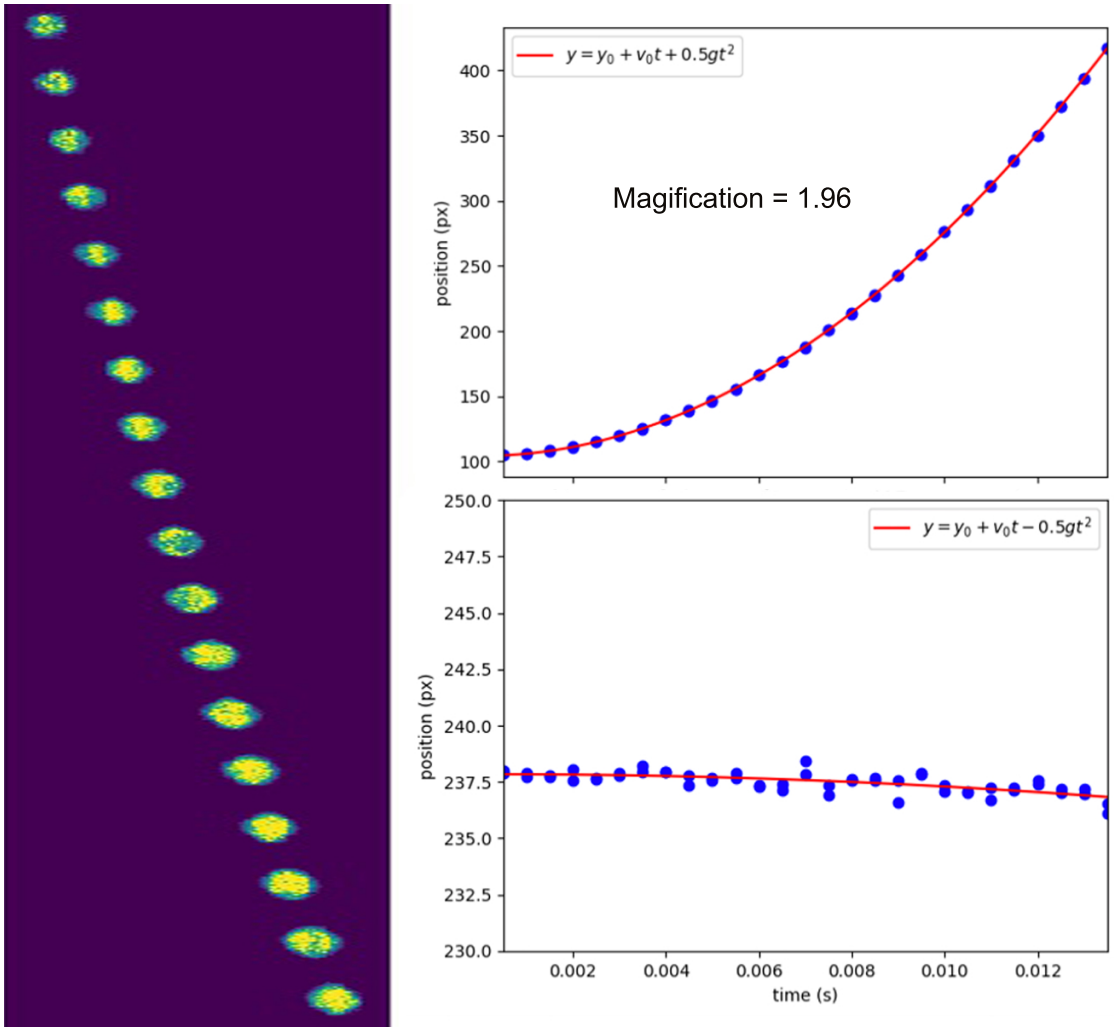

Figure 3.10: Overall magnification for the xz imaging system, determined via BEC free fall under gravity.

This importance will be evident in Section 3.9.

3.8 Digital Micromirror Device System

The intensity profile of a beam can be shaped using a Digital Micromirror Device, a type of spatial light modulator (SLM), composed of a two-dimensional array of periodically spaced movable micromirrors mounted over a CMOS memory cell. In our setup, the DMD is used to generate configurable disorder for Raman systems,

enabling new experimental directions as discussed in Chapters 7 and 8. Each micromirror has two stable tilt states, corresponding to an "on" or "off" position. Each mirror's tilt is set by programming its memory cell, allowing dynamic updates through an external trigger controlled by an experiment control computer.

When illuminated with coherent light, the periodic micromirror array of a DMD acts as a two-dimensional diffraction grating. The resulting diffraction pattern consists of discrete orders, whose angular positions are determined by the grating equation, modulated by a broader *intensity envelope* arising from the finite size of each micromirror (single-slit diffraction). In a *blazed grating* [103], the groove geometry is engineered so that the envelope maximum aligns with a desired non-zero diffraction order, (thereby maximizing its efficiency). In this *blaze configuration* and with the envelope centered normal at the grating, the blaze condition simplifies to

$$\sin(2\theta_i) = m\frac{\lambda}{d}, \tag{3.9}$$

where m is the diffraction order, λ the wavelength, d the grating period, and θ_i the angle of incidence. The LuxBeam DMD geometry is equivalent to a two-dimensional blazed grating, and therefore its intensity envelope can be described by:

$$\mathrm{Sinc}^2\left[\frac{\pi a_x}{\lambda}(x + x_i)\right] \mathrm{Sinc}^2\left[\frac{\pi a_y}{\lambda}(y + y_i)\right], \tag{3.10}$$

where a_j denotes grating pitch along the j-axis, and the overall intensity envelope is separable along the x and y directions. The corresponding two-dimensional grating

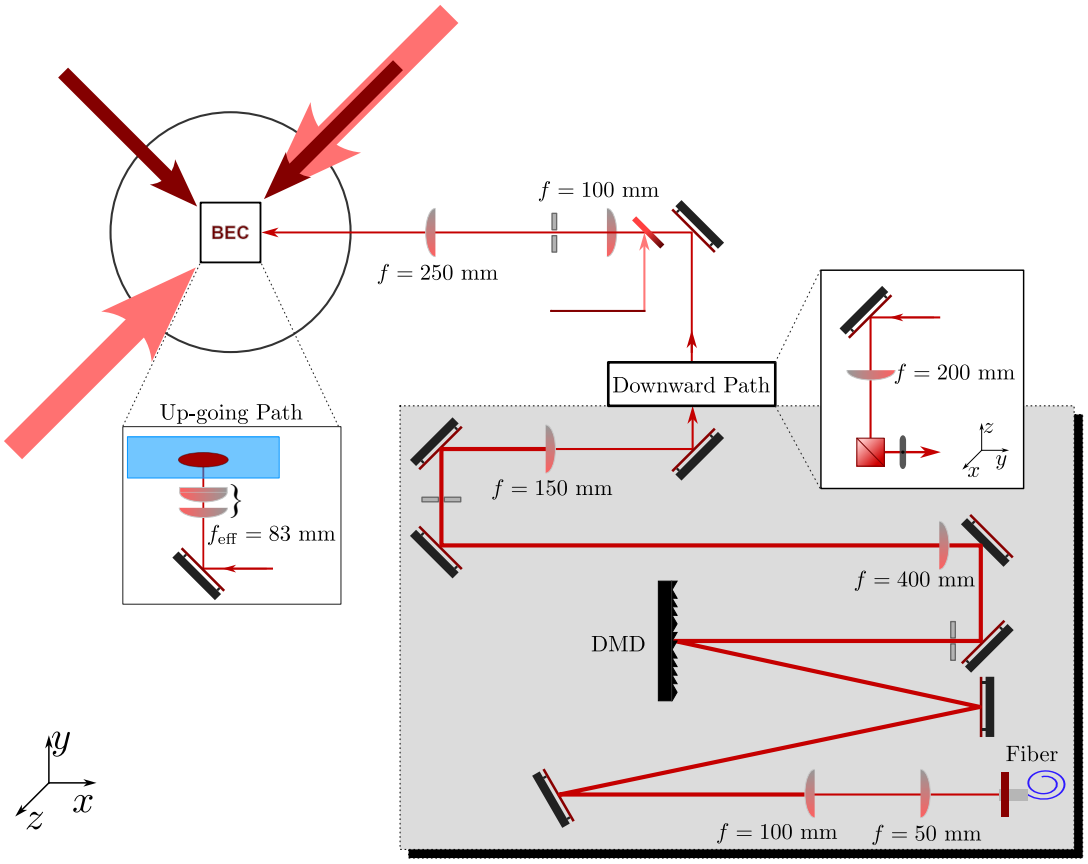

Figure 3.11: Schematic of the LuxBeam DMD optical system.

equation can then be written as

$$\sin\theta_{m,j} + \sin\theta_{i,j} = m_j \frac{\lambda}{a_j}, \quad j \in x, y, \tag{3.11}$$

where θ_j represents the beam's angle of incidence in the z–j plane.

The optical system implemented to project DMD patterns onto the atoms is integrated into the xy imaging system path. In other words, the beam passes through the DMD projection optics before continuing through the xy imaging system en route to the atoms. This system is supplied with a 790 nm fiber output from the Raman bean setup with $\approx$ 120 mW power (measured after the telescope). The

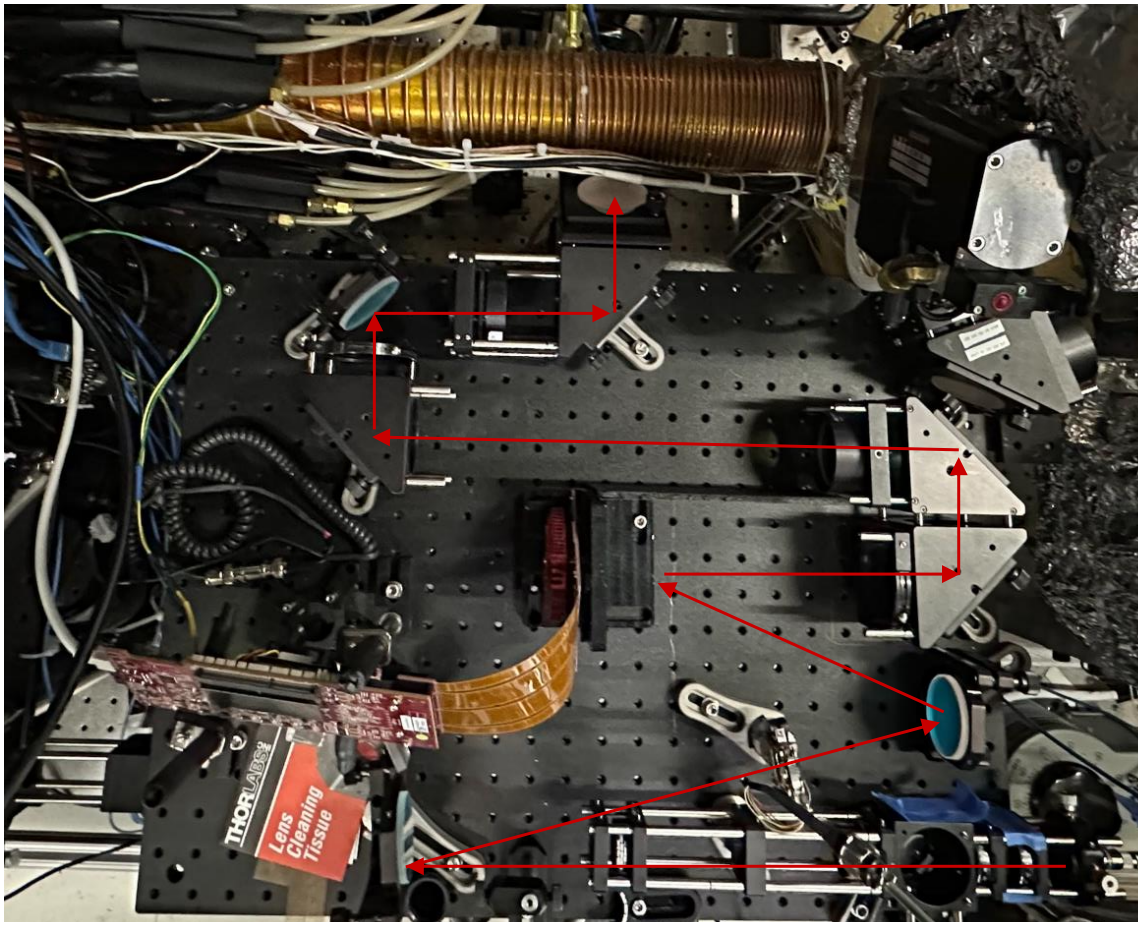

Figure 3.12: Schematic of the main stage of the LuxBeam DMD optical system.

LuxBeam DMD projection system consists of four imaging stages. The first stage is a 2× magnifying telescope composed of two achromatic doublets, ($f_1 = 50$ mm and $f_2 = 100$ mm), magnifying the beam 2×. The second stage is the main stage with two achromatic doublets, ($f_1 = 400$ mm and $f_2 = 150$ mm), yielding a demagnification = 2.667×. An aperture is placed at the Fourier plane of this stage to mark the spatial frequency location; it is currently unused but reserved for future experiments. The third stage consists of two achromatic doublets ($f = 200$ mm and $f = 100$ mm), forming a relay imaging system with a demagnification of 2×. A polarizing beam splitter is located in the Fourier plane, along with a $\lambda/4$ waveplate,

and 767 nm dichroic (belonging to the second LightCrafter DMD optical system). The fourth stage comprises an achromatic doublet with $f = 250$ mm and a two-lens compound objective with an effective focal length of $f = 83$ mm, providing an additional demagnification of 3×. The third and fourth stages make up the stages of the xy imaging system and the total magnification was measured to be 5.8 (as shown in Fig. 3.7), and not exactly 6. The total effective demagnification of the DMD projection optics is therefore

$$\mathrm{M_{DMD}} = (2.667)(5.8) = 15.4667. \tag{3.12}$$

A single micromirror of size $d = 10.8$ μm therefore maps to the image plane at the atoms as

$$d' = \frac{d}{M_{\mathrm{DMD}}} = 0.698(3)\ \mu\mathrm{m}, \tag{3.13}$$

which is below the 2.7 μm resolution limit of the imaging system. In addition, the DMD beam waist at the atoms is approximately 100 μm.

3.9 $\mathrm{TEM_{01}}$ System – Aka: Sheet Trap

The purpose of a sheet trap is to create a planar condensate to confine atoms in two dimensions (2d) by providing strong confinement along one axis. In our implementation, this tight confinement is along the z-axis and is produced using a transverse electromagnetic mode, $\mathrm{TEM_{01}}$–like, optical beam. Such a beam can be generated by passing an incident Gaussian mode through a phase plate that imparts

a π phase shift between its two halves, followed by focusing the modified beam onto the atoms. In the focal plane, the resulting intensity distribution closely resembles that of a Hermite–Gaussian mode:

$$I(x,z) = \frac{2P}{\pi W_x W_z} \frac{4z^2}{W_z^2} \exp\left(-\frac{2z^2}{W_z^2} - \frac{2x^2}{W_x^2}\right), \tag{3.14}$$

where the beam propagates along y, and W_x and W_z denote the beam waists in the x- and z-directions, respectively, P is the beam power, and the phase step is oriented along z. In practice, the focal-plane intensity differs slightly from that of an ideal Hermite–Gaussian beam [104]:

$$I(x,z) = \frac{2P}{\pi W_x W_z} \mathrm{erfi}\left(\frac{z}{W_z}\right)^2 \exp\left(-\frac{2z^2}{W_z^2} - \frac{2x^2}{W_x^2}\right), \tag{3.15}$$

where $\mathrm{erfi}(z)$ is the imaginary error function, defined by $\mathrm{erfi}(z) = -i\,\mathrm{erf}(iz)$. For small arguments, $\mathrm{erfi}(z) \approx \frac{2}{\sqrt{\pi}} z$, leading to the approximate focal-plane intensity:

$$I(x,z) \approx \frac{2P}{\pi W_x W_z} \frac{4z^2}{\pi W_z^2} \exp\left(-\frac{2z^2}{W_z^2} - \frac{2x^2}{W_x^2}\right). \tag{3.16}$$

Relative to a standard Gaussian beam, this profile includes an additional factor $4z^2/(\pi W_z^2)$, and compared to a Hermite–Gaussian beam, it differs by an overall factor $1/\pi$. The deviation from the ideal mode arises because a significant fraction of the optical power is redistributed into the wings of the distribution. Nevertheless, for an optical system designed to focus a Gaussian beam to waists (W_x, W_z) in the absence of the phase plate, the intensity profile with the phase plate is well described

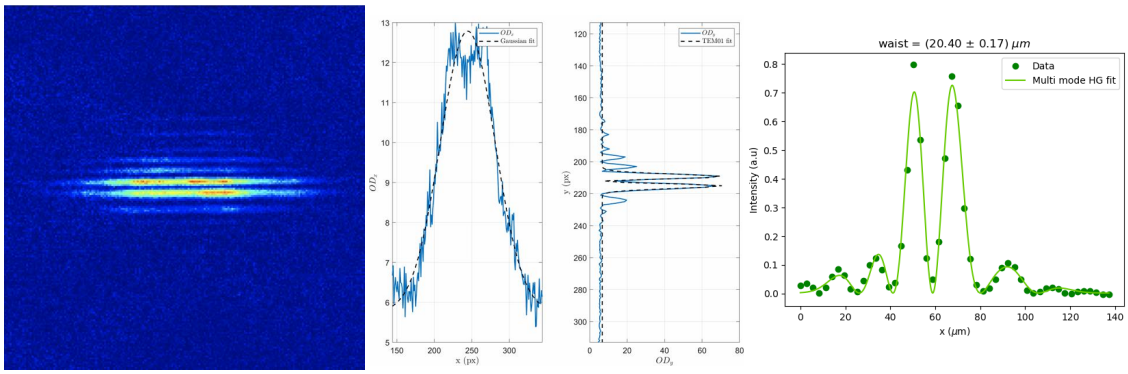

Figure 3.13: TEM_{01} beam imaged on the camera with a corresponding Hermite–Gaussian multi-mode fit. Notice the side fringes on either side of the main sheet, indicating possible side band trapping as a result of clipping and reflections from various optical elements.

by Eq. (3.16). The corresponding dipole potential is proportional to the intensity, and can be expressed as [19]:

$$U_0(x,z) = -\frac{1}{2\epsilon_0 c}\,\mathrm{Re}(\alpha)\,I(x,z), \tag{3.17}$$

where ϵ_0 is the vacuum permittivity, c is the speed of light, and α is the atomic polarizability. For a two-level atom, this becomes:

$$U_0(x,z) = \frac{3\pi c^2}{2\omega_0^3}\frac{\Gamma}{\Delta}\,I(x,z), \tag{3.18}$$

where ω_0 is the atomic transition frequency, Γ is the natural linewidth, and Δ is the laser detuning from resonance. Expanding Eq. (3.18) about $x = z = 0$ yields the trapping frequency in the z-direction (for the two-level approximation):

$$\frac{\omega_z}{2\pi} = \sqrt{-\frac{6Pc^2\Gamma}{m\omega_0^3\Delta\pi^3 W_x W_z^3}}, \tag{3.19}$$

where m is the atomic mass, W_i are the beam waists, and ω_z is the trap frequency along z. However, this expression uses the rotating wave approximation. Since we are using 532 nm light on ^{87}Rb, we are too far from resonance to make this approximation, so a more appropriate expression is

$$\frac{\omega_z}{2\pi} = \sqrt{-\frac{6Pc^2\Gamma}{m\omega_0^3\pi^3 W_x W_z^3}\left(\frac{1}{\omega_0-\omega}+\frac{1}{\omega_0+\omega}\right)}, \tag{3.20}$$

where ω is the frequency of the laser light. This equation yields values very close to calculations that take into account both the D_1 and D_2 transitions.

3.9.1 Anti-Trapping From Zero-Point Energy

Although the TEM_{01} beam produces strong confinement along the z axis, the resulting ground-state (zero-point) energy of the tight z-motion varies across the in-plane coordinates, in other words, the ground state energy of the atoms is not homogeneous and in the transverse direction actually changes depending on where you are in the xy-plane[3]. This spatial dependence produces an effective potential in the xy-plane which can have *negative* curvature (anti-trapping). Below is a brief derivation of this effect and the leading order anti-trapping frequencies. The intensity profile of the beam near the focal plane[4] can be approximated by considering values of z close to zero—that is, near the tightly confined direction's center. In this region, the

[3]Note regarding coordinates: The TEM_{01} beam travels along the y-axis, and the tight confinement is along z. This variation in zero-point energy acts like an extra potential in the transverse directions, xy plane, and it curves the potential downward—this is what we call anti-trapping.

[4]The focal plane is the specific plane perpendicular to the beam's propagation direction where the light is focused to its smallest spot (tightest waist). In other words, it's the location along the beam path where the beam intensity profile reaches its minimum width and maximum intensity.

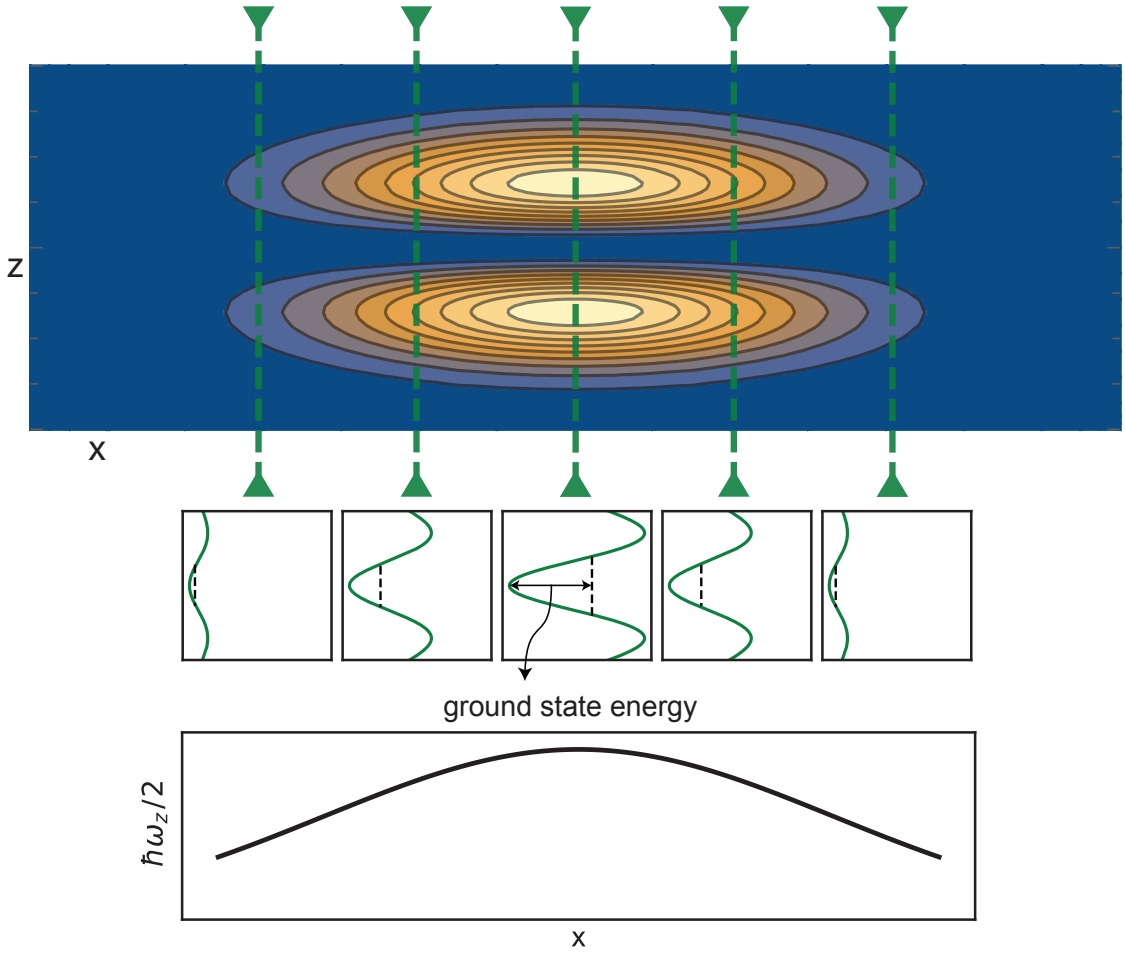

Figure 3.14: Anti-Trapping From Zero-Point Energy. Illustration depicting ground state energy and how it varies with position in the TEM_{01} trap.

intensity varies quadratically with z, reflecting the node created by the π-phase step. Meanwhile, the dipole potential experienced by the atoms can be approximated as harmonic along the z-axis, expressed as

$$U(x, y, z) \simeq \frac{1}{2} m\omega_z^2(x, y)\, z^2 + \dots . \tag{3.21}$$

where the tight-axis trapping frequency $\omega_z(x, y)$ varies smoothly across the xy-plane. For atoms localized in the z ground state, the leading contribution to the effective

2d potential is the zero-point energy,

$$U_z(x,y) = \frac{\hbar}{2}\,\omega_z(x,y). \tag{3.22}$$

Substituting Eq. (3.20) and Taylor expanding $\omega_z(x,y)$ to quadratic order, in x and y, yields effective anti-trap frequencies in the x and y directions, respectively:

$$\frac{\omega_{y,\mathrm{at}}}{2\pi} = \frac{1}{2\pi}\sqrt{\frac{8Pa}{cm\pi^2\,W_x^2 W_y^6}}, \tag{3.23a}$$

$$\frac{\omega_{x,\mathrm{at}}}{2\pi} = \frac{1}{2\pi}\frac{2^{3/4}\,P^{1/4}a^{1/4}\,\hbar^{1/2}}{c^{1/4}m^{3/4}\pi^{1/2}\,W_x^{5/4}W_y^{3/4}}. \tag{3.23b}$$

Because the anti-trapping curvature scales as $\hbar\omega_{z0}/W_i^2$, stronger tight confinement (larger ω_{z0}) increases the anti-trap strength. Conversely, broader waists reduce the anti-trap curvature.

3.9.2 Optical System

The TEM_{01} beam was supplied by a Verdi V10 laser with a 10 W power output. The optical system consisted of a 2× demagnifying telescope, composed of lenses with focal lengths $f = 50$ mm and $f = 25$ mm, which delivered a 532 nm Gaussian beam with a waist of approximately 425 um into an AOM. The output beam was then sent through the sheet-trap axis-shaping cylindrical lenses ($f = 400$ mm and $f = -12$ mm), followed by a $f = 150$ mm achromatic doublet collimating lens. In the Fourier plane, resides a 0–π phase plate, after which a $f = 250$ mm achromatic doublet serves as the final focusing lens. The focused beam is directed into

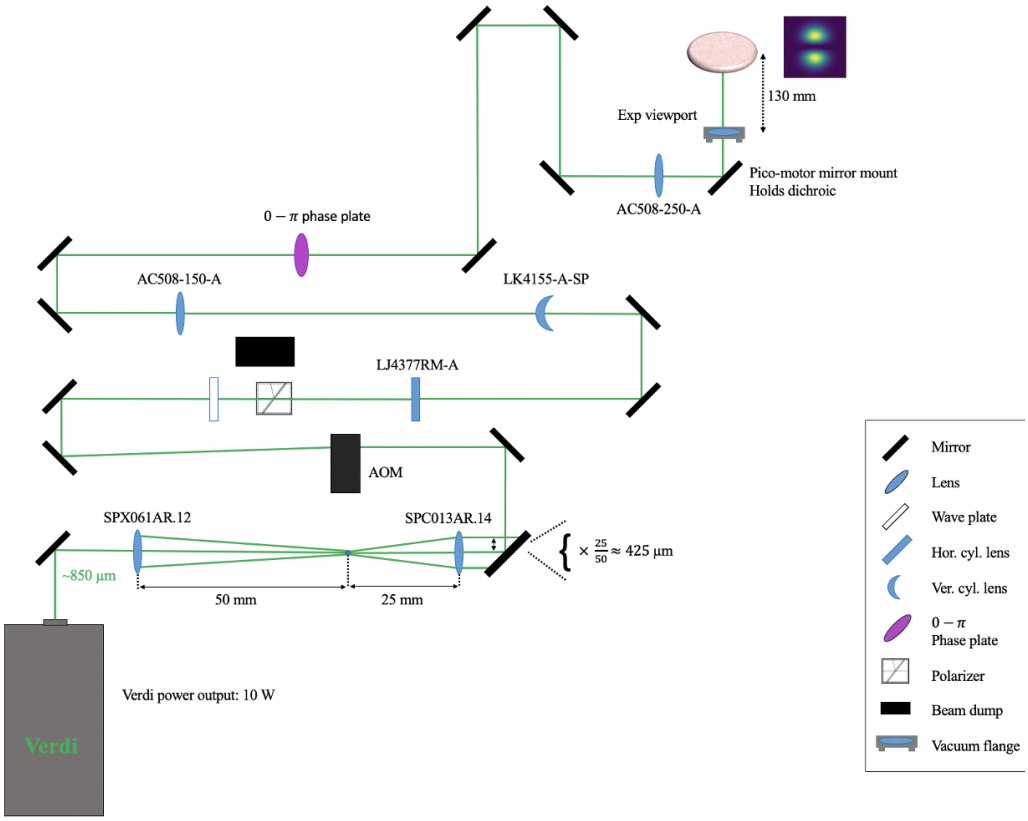

Figure 3.15: Schematic of the TEM_{01}– sheet trap optical system.

the experimental chamber via a dichroic mirror mounted on a picomotor, enabling precise alignment. The measured beam power entering the experimental chamber was 3.9 W.

3.9.3 Performance

The implementation of the TEM_{01} trap was successful. Initial coarse alignment was performed by aligning the beam center to the xz-probe beam at a large distance. For fine alignment, the dichroic mirror mounted on a picomotor was used, slightly adjusting the position of the beam going into the experimental chamber and hitting the atoms. Atoms were adiabatically loaded into the trap over 300 ms to the final

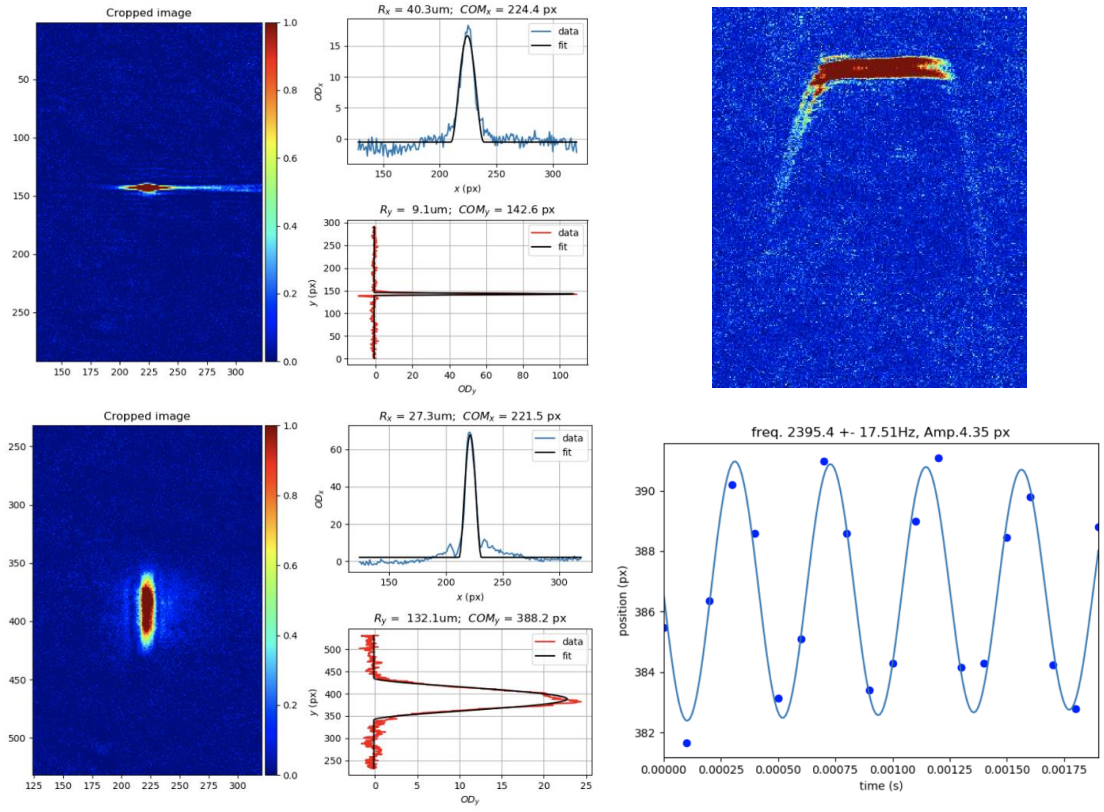

Figure 3.16: Images of BEC in the TEM_{01} Trap and maximum trapping potential. On the left, insitu and time-of-flight images of atoms in the trap and showing modified TF radii. On the right, an image of atoms spilling from the trap. In addition, measurement of the maximum trapping frequency obtained with the atoms confined in 2d.

total intensity, held for an additional 300 ms, and then all confinement—both 2d and harmonic—was abruptly snapped off. Imaging was performed along the *xz* direction. To verify that the horizontal tilt of the trap was balanced, a variable hold time was introduced into the experimental sequence. As the hold time increased, atoms gradually spilled from the sheet trap due to the finite trap lifetime. Uniform loss of atoms, i.e. spilling, from both sides of the trap indicated that the tilt was level. Additionally, the Thomas–Fermi (TF) radii provided a gauge of the trapping potential: as the trapping frequency increased, the BEC became more elongated

Table 3.1: TEM_{01} Trap Parameters

Parameter	**Value**
Wavelength	532 nm
Power at atoms	3.9 W
Final focusing lens focal length	250 mm
Beam size at atoms (short axis)	8.4 μm
Beam size at atoms (long axis)	265 μm
Rayleigh length at atoms	417 μm
Tight confinement frequency, $\omega_z/2\pi$	2.4 kHz

along the vertical axis. Although at large trapping frequencies, the observed change in radii were subtle.

The maximum trapping frequency was found by scanning, literally rotating, the 250 mm focus lens, to find the optimal focus distance. Note that changing this focus position required new alignment each time. The maximum measured trapping frequency was $\omega_z/2\pi = 2.4$ kHz, with the beam size at the atoms measured to be 8.4 um (short axis) and 265 um (long axis). The calculated anti-trapping frequencies were $\omega_{x,\mathrm{at}}/2\pi = 2.0$ Hz and $\omega_{y,\mathrm{at}}/2\pi = 1.1$ Hz, which were negligible and therefore did not require compensation.

3.10 Measurement

Probing and characterizing ultracold atomic clouds is most effectively achieved through optical imaging techniques. In our setup, time-of-flight measurements are performed using resonant absorption imaging, while *in situ* measurements are carried out via partial transfer absorption imaging (PTAI).

3.10.1 Absorption Imaging with Doppler Correction

Absorption imaging converts the fraction of scattered light into atomic density using Eqs. 2.17a&b. By illuminating the cloud with resonant light ($\delta = 0$) of intensity $I_0(x, y)$ and recording the transmitted intensity $I_f(x, y)$, the atomic cloud casts a shadow proportional to its density [45–47].

Low Intensity Imaging: Beer-Lambert Law

For $I \ll I_{\text{sat}}$ and $\delta = 0$, $\sigma \approx \sigma_0$, reducing Eq. 2.17b to:

$$n_{2d}(x, y) = \int dz\, n(x, y, z) = -\frac{1}{\sigma_0} \ln\left(\frac{I_f}{I_0}\right). \tag{3.24}$$

Since only intensity ratios matter, no absolute calibration is required. Using camera counts N_A and N_0, the optical density is:

$$\text{OD}_0(x, y) = n_{2d}\sigma_0 = -\ln\left(\frac{N_A}{N_0}\right).$$

High Intensity Imaging: Saturated Beer-Lambert Law

For $I_0 I_{\text{sat}}$, saturation reduces σ significantly. Using dimensionless variables $s = I/I_{\text{sat}}$, $s_0 = I_0/I_{\text{sat}}$, and $s_f = I_f/I_{\text{sat}}$, we solve:

$$\frac{ds}{s} = -n\sigma_0 \frac{1}{1+s} dz, \quad \Rightarrow \quad \int_{s_0}^{s_f} \frac{ds}{s(1+s)} = -n_{2d}\sigma_0.$$

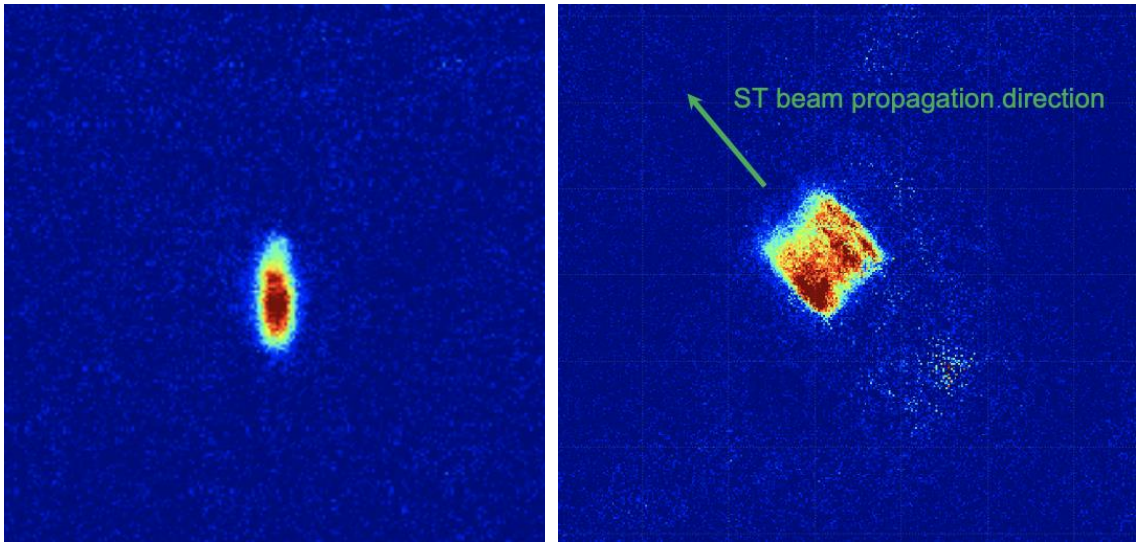

Figure 3.17: Applications of Partial-Transfer Absorption Imaging (PTAI). Left: Image of insitu low-density BEC after PTAI. Right: Image of BEC in the TEM_{01} trap confined in a box potential.

Evaluating the integral via separation of variables gives:

$$\ln\left(\frac{s_f}{s_0}\right) + (s_f - s_0) = -n_{2d}\sigma_0, \quad \Rightarrow \quad n_{2d} = -\frac{1}{\sigma_0}\left[\ln\left(\frac{I_f}{I_0}\right) + \frac{I_f - I_0}{I_{\mathrm{sat}}}\right]. \quad (3.25)$$

Unlike the simple Beer-Lambert case, this regime requires absolute calibration of I_{sat}. Calibration can be performed either by knowing the camera gain, efficiency, and magnification, or by scanning the imaging intensity and measuring the apparent optical density on a fixed atomic cloud.

3.10.2 Partial-Transfer Absorption Imaging

In many cases, absorption imaging is unable to accurately capture key characteristics of the atomic cloud—such as fine density variations or Thomas–Fermi radii—when the optical density is too high, ODs ≥ 3. While the OD can, in principle, be reduced

by lowering the atom number to produce a more dilute BEC or by imaging off resonance, these approaches often still require complex post-processing to reconstruct the true density profile, and the results are not always reliable.

Partial-transfer absorption imaging overcomes the limitations imposed by high optical density by addressing only a controllable subset of the atomic cloud. A small, tunable fraction of atoms is transferred into a state that interacts with the probe light, while the majority remain in a non-resonant "dark" state, unaffected by the imaging process. This selective probing allows for fine control of the effective optical density and minimizes disturbance to the atomic ensemble. This method plays a central role in many of the experiments described in this thesis, including magnetic field drift monitoring, xy imaging system characterization, chemical potential calibrations and disorder characterization.

Chapter 4: Ultracold Atoms in Optical Lattice Potentials

This chapter introduces the essential physics of a single particle in a one-dimensional (1d) optical lattice. The high experimental controllability of cold atoms in optical lattices makes them suitable candidates to study a diverse range of Hamiltonians, from condensed matter to high energy, where the atoms play the role of other particles such as electrons, positrons, or helium atoms, and is the foundation for understanding Raman coupled systems in Chapter 7. This model provides the framework for the experimental lattice system discussed in Chapter 5.

4.1 Optical Lattice Potentials

The emergence of a band structure is a fundamental feature of a periodic potential, such as an optical lattice. These periodic optical potentials can be tailored across various dimensions, with tunable properties including potential depth—regulated by the laser beam intensity—geometry, determined by the spatial configuration of the lasers which allows modification of the crystal's unit cell, and frequency detuning, where changes in light polarization enable the movement or reshaping of the lattice structure.

1d Lattice Potential. A 1d optical lattice can be created by counter-propagating laser beams (for example by retro-reflecting a laser focused on to the position of the atoms) such that a standing wave interference pattern is created. This yields a

periodic trapping potential

$$V_L(x) = -V_0 \sin^2(k_L x),$$

where V_0 is the lattice depth and $k_L x = 2\pi/\lambda$. The addition of more laser beams allows for the realization of two- and three-dimensional optical lattices; however, careful control of the polarizations and phases of the beams is essential to ensure the desired lattice structure is achieved.

4.2 Single Particle Hamiltonian

Consider a single particle in a 1d periodic potential described by the Hamiltonian

$$H = \frac{\hat{p}_x^2}{2m} + V_L(x) \ = \frac{\hat{p}_x^2}{2m} - V_0 \sin^2(k_L x), \tag{4.1}$$

where $V_L(x) = V_L(x + a)$ with periodicity $a = \lambda/2$. The energy scale is determined by the corresponding photon recoil energy

$$E_{\mathrm{L}} = \frac{\hbar^2 k_{\mathrm{L}}^2}{2m_{Rb}} = h \times 2.02 \text{ kHz}, \tag{4.2}$$

where $k_L x = 2\pi/(1064 \text{ nm})$, m is the mass of the atom and here rubidium-87 is used for the mass m_{Rb}.

The eigenstates $\Psi_{q,n}(x)$ of this Hamiltonian take the form of a plane wave times a

function $u_{q,n}(x)$ as described by Boch's Theorem [105, 106]

$$\Psi_{q,n}(x) = e^{iqx} u_{q,n}(x); \;\; u_{q,n}(x) = u_{q,n}(x+a), \tag{4.3}$$

with $u_{q,n}(x)$ having the same periodicity as the potential, and where the wave vector q is the crystal momentum, describing momentum in the lattice and n describes the lattice band.

The eigenstates $\Psi_{q,n}(x)$ satisfy Schrodinger's equation, yielding an effective equation for $u_{q,n}(x)$

$$\left[\frac{(\hat{p}_x + \hbar q)^2}{2m} + V_L(x)\right] u_{q,n}(x) = E_{q,n} u_{q,n}(x). \tag{4.4}$$

Since both V_L and $u_{q,n}$ are periodic with periodicity in momentum space of $2k_L$, a Fourier transform can be executed for the above equation, where V_r and $C_l^{q,n}$ are Fourier components, r and l are integers, and together give the general form

$$V_L(x) = \Sigma_r V_r e^{ir(2k_L)x} \;\; \text{and} \;\; u_{q,n}(x) = \Sigma_l C_l^{q,n} e^{il(2k_L)x}. \tag{4.5}$$

Now Schrodinger's equation can be rewritten with the summed plane waves for the lattice potential and eigenstates as

$$\left[\frac{(\hat{p}_x + \hbar q)^2}{2m} + \Sigma_r V_r e^{ir(2k_L)x}\right] \Sigma_l C_l^{q,n} e^{il(2k_L)x} = E_{q,n} \Sigma_l C_l^{q,n} e^{il(2k_L)x}. \tag{4.6}$$

The momentum operator acting on the momentum space wavefunction is just a number, $\hat{p}_x = 2l\hbar k_L$. Moreover, there are only three non-zero Fourier components

for the 1d optical lattice potential, $V_L = -V_0 \sin^2(k_L x)$, with $r = \pm 1$ being $-V_0/4$ and $r = 0$ being $V_0/2$. With these substitutions, Schrodinger's equation becomes

$$\Sigma_l \left[\frac{(2l\hbar k_L + \hbar q)^2}{2m} + \left(\frac{V_0}{2} - \frac{V_0}{4} e^{2ik_L x} - \frac{V_0}{4} e^{-2ik_L x} \right) \right] C_l^{q,n} e^{2ilk_L x}$$
$$= E_{q,n} \Sigma_l C_l^{q,n} e^{2ilk_L x} \tag{4.7}$$

$$\Sigma_l \left[\frac{(2l\hbar k_L + \hbar q)^2}{2m} C_l^{q,n} + \left(\frac{V_0}{2} C_l^{q,n} - \frac{V_0}{4} C_{l-1}^{q,n} - \frac{V_0}{4} C_{l+1}^{q,n} \right) \right] e^{2ilk_L x}$$
$$= E_{q,n} \Sigma_l C_l^{q,n} e^{2ilk_L x}. \tag{4.8}$$

Now that the sum over l and the exponentials are identical on both sides, we can compare the coefficients directly

$$\frac{(2l\hbar k_L + \hbar q)^2}{2m} C_l^{q,n} + \frac{V_0}{2} C_l^{q,n} - \frac{V_0}{4} C_{l-1}^{q,n} - \frac{V_0}{4} C_{l+1}^{q,n} = E_{q,n} C_l^{q,n}. \tag{4.9}$$

This equation can be conveniently written in a matrix form, $H_{l,l'} \vec{C}_{l'}^{q,n} = E_{1,n} \vec{C}_{l'}^{q,n}$, with a basis $\{C_l^{q,n}\}$. The diagonal term is $\frac{(2l\hbar k_L + \hbar q)^2}{2m} + \frac{V_0}{2}$. However, note that the constant term in the diagonal, $\frac{V_0}{2}$, is just an overall energy offset and can be removed for simplicity.

$$H_{l,l'} C_l^{q,n} = E_{q,n} C_l^{q,n}; \quad \text{where } l = \text{bands kept}$$

$$H_{l,l'} = E_r \left\{ \begin{array}{ll} (2l + \frac{q}{k_L})^2 & \text{if } l = l' \text{ diagonal} \\ \frac{-1}{4} \frac{V_0}{E_r} & \text{if } |l - l'| = 1 \text{ off diagonal} \\ 0 & \text{otherwise} \end{array} \right\} \tag{4.10}$$

Figure 4.1 shows the band structure of a 1d periodic lattice potential for different

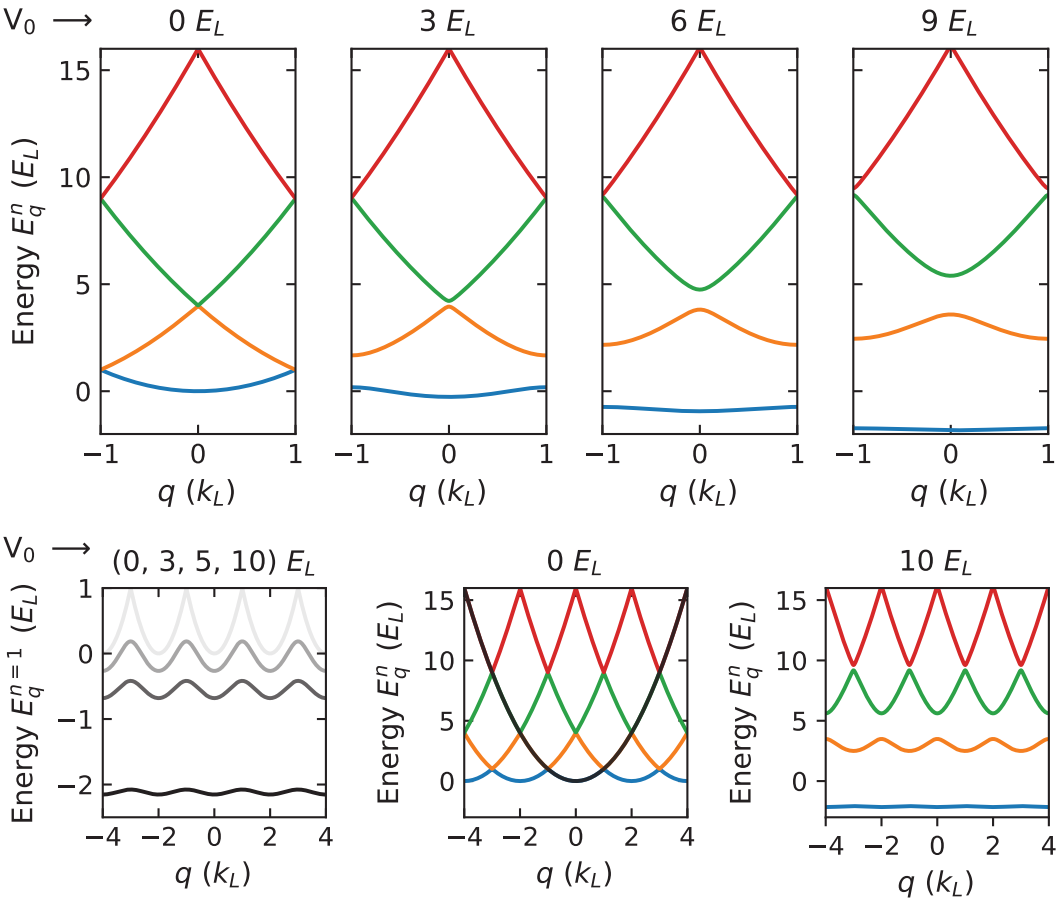

Figure 4.1: Band structure of a 1d periodic lattice potential. Here the energy bands $\mathrm{E}_n(q)$ are shown for lattice depths $V_0 = (0, 3, 6, 9)\mathrm{E_L}$ with $n = 0, 1, 2, 3$ & q from -1 to 1. The bottom left plot shows the energy bands $\mathrm{E}_n(q)$, where $n = 1$, for $V_0 = (0, 3, 5, 10)\mathrm{E_L}$ and q from -4 to 4. The bottom right plot shows the energy bands $\mathrm{E}_n(q)$, where $n = 1, 2, 3$, for $V_0 = 10\mathrm{E_L}$ and q from -4 to 4. In the absence of a lattice, at $V_0 = 0$, the dispersion relation corresponds to that of a free particle, where $E \propto q^2$, resulting in a quadratic energy spectrum. This is shown by the black curve in the bottom center plot. As the lattice depth increases, band structure emerges. For shallow lattices, discontinuities appear only at the edges of the Brillouin zone. With further increase in lattice depth, the energy bands become progressively flatter and the band gaps widen. This behavior is evident both within individual bands and across multiple bands.

lattice depths V_0 by diagonalizing the matrix of (4.10) with dimension = 25. The energy bands $\mathrm{E}_n(q)$ are shown for $V_0 = (0, 3, 6, 9)\mathrm{E_L}$ with $n = 1, 2, 3$. The bottom left plot shows the energy bands $\mathrm{E}_n(q)$, where $n = 1$, for $V_0 = (0, 3, 5, 10)\mathrm{E_L}$ and q

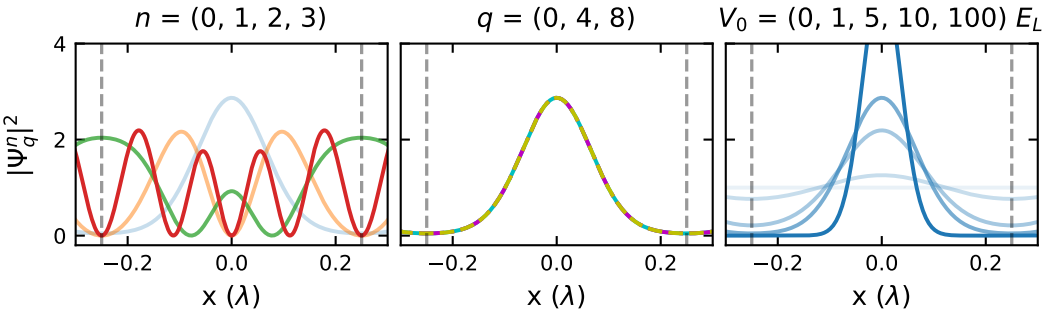

Figure 4.2: Bloch wave functions for different values of n, q and V_0.

from -4 to 4. The bottom right plot shows the energy bands $\mathrm{E}_n(q)$, where $n = 1, 2, 3$, for $V_0 = 10\mathrm{E_L}$ and q from -4 to 4. In the absence of a lattice, for V_0, we obtain the dispersion relation for a free particle, where $E \propto q^2$, so the spectrum is quadratic in q. This is depicted by the black curve in the bottom center plot. As the depth is increased, the band structure appears. For small lattice depths the discontinuity occurs only at the edge of the first Brillouin zone. Another noticeable feature is as the lattice depth increases, the band flattens out and the energy gaps increase. This is observed for a single energy band, as well as for multiple energy bands.

4.2.1 Bloch Bands

In the absence of a lattice, the eigenfunctions of the free system are plane waves. As the lattice depth increases, the barrier height between adjacent lattice sites increase, causing the eigenstates to become increasingly localized at individual lattice sites. At time t = 0, the lattice potential is switched on, and using the Hamiltonian described above, we can evaluate the corresponding eigensystem $H\left|\Psi_q^n\right\rangle = E_q^n\left|\Psi_q^n\right\rangle$.

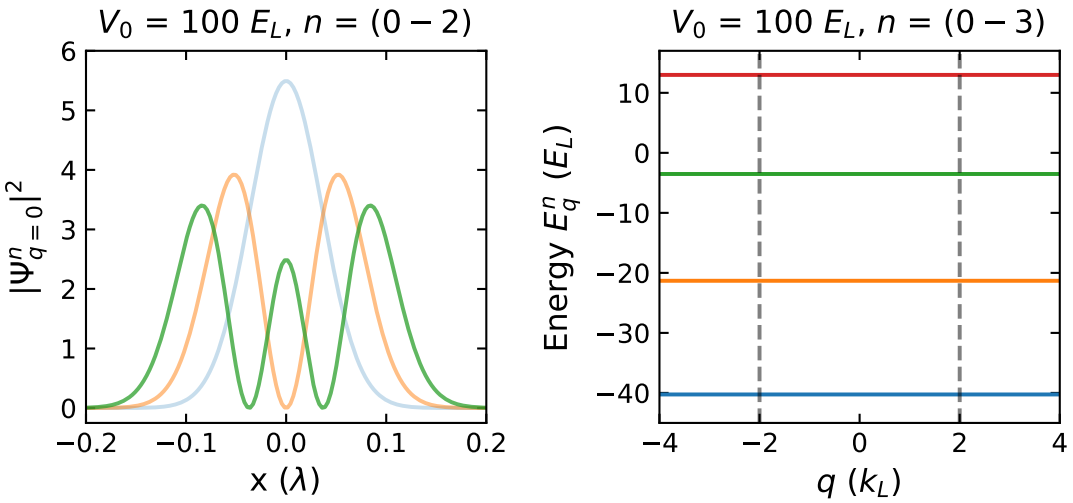

Figure 4.3: Harmonic Approximation.

Evaluating the Bloch wave function in the momentum basis gives

$$
\begin{aligned}
< k|\Psi^n_q > &= \int dx \left(e^{\frac{ikx}{\sqrt{2\pi\hbar}}}\right)^* e^{iqx} u_{q,n}(x) \\
&= \int dx \left(e^{\frac{ikx}{\sqrt{2\pi\hbar}}}\right)^* e^{iqx} \Sigma_l C^n_{q,l} e^{i2lk_L x}.
\end{aligned}
$$

In the position basis, the Bloch wave function is just $\left\langle x \middle| \Psi^n_q \right\rangle = e^{iqx} u^n_q(x)$. Figure 4.2 plots the Bloch wave functions for different values of n, q and V_0. It becomes clear that as the lattice depth increases, the wave function becomes more localized.

Harmonic Approximation. In this limit, when the coupling strength $V_0 > 5E_L$ and atoms are tightly confined in the lattice sites, the lattice potential can be approximated as a sum of harmonic oscillator potentials centered at each of these lattice sites. A notable feature is that as the lattice depth increases, $V_0 > 50E_L$, the energy bands $\mathrm{E}_n(q)$ become flatter, and the energy gaps between consecutive bands widen. Refer to Figure 4.3.

4.2.2 Wannier Functions

Optical lattices form periodic potentials analogous to crystal lattices in solids, but for neutral ultracold atoms instead of electrons. Just as electrons in a crystal can be described by Bloch functions and their localized counterparts—Wannier functions—are a set of orthonormal wave functions that fully describe particles in a band and are localized at lattice sites. Wannier functions provide a real-space, localized basis and are constructed by taking the Fourier transform over the Bloch functions of a given band. For a system with a finiite number of lattice sites M, they are defined as

$$w_n(x - x_i) = \frac{1}{\sqrt{(}M)} \sum_q e^{-iqx_i} \Psi_q^n(x) \tag{4.11}$$

where $\Psi_q^n(x)$ are Bloch functions, M is the total number of lattice sites, n is the band index, q is the quasimomentum, and i is the lattice site. The sum is over the first Brillouin zone, and this Fourier transform is a unitary transformation (assuming orthonormal Bloch states), meaning the Wannier functions remain orthonormal and complete. The approximate form of a Wannier function can be derived by assuming that the periodic part of the Bloch functions, $u_q^n(x)$, remains nearly constant across the Brillouin zone for a given band. Under this approximation, the Wannier function centered at the origin is given by

$$w_n(x) \approx u^n(x) \frac{\sin(kx)}{kx}. \tag{4.12}$$

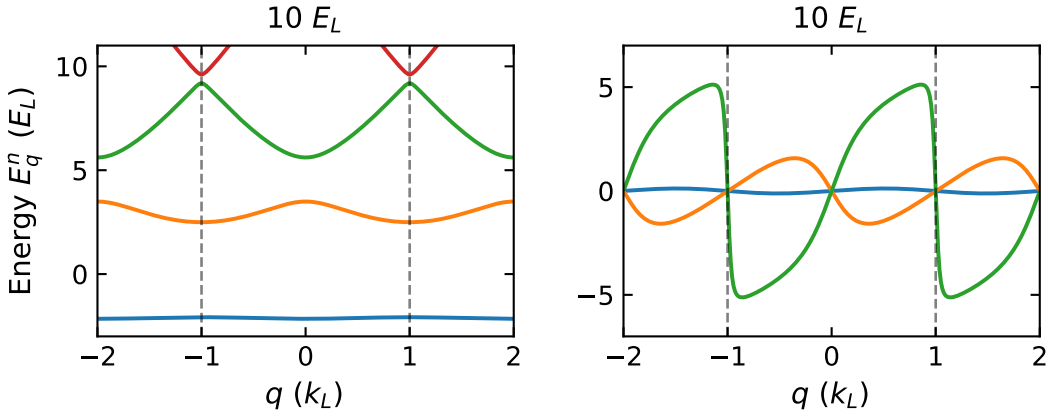

Figure 4.4: Group velocity of lattice energy bands. Here the three lowest energy bands $\mathrm{E}_n(q)$ and corresponding group velocitites are shown for lattice depth $V_0 = \ 10\mathrm{E_L}$ & quasimomentum q from -2 to 2.

This resembles $u^n(x)$ localized at the center of the site, modulated by oscillations whose amplitude gradually decreases with distance. Each Wannier function is centered at a specific lattice site and generally exhibits rapid decay away from that site.

4.3 Hellmann-Feynman Theorem

The Hellmann-Feynman theorem is useful for optical lattice potentials as it allows for the derivative of the dispersion relation of a band to be interpreted as the group velocity v_g, indicating how fast the wave packet is moving. Interestingly, the group velocity v_g corresponds to the weighted average of the velocities associated with each momentum component making up the state, where the weights are given by the probabilities of those components in the wavefunction. For example, in the lowest band of a lattice, at $q = 0$, the state consists of a symmetric superposition of momentum components with $p = +n\hbar k$ and $p = -n\hbar k$. These contributions cancel

out when weighted by their respective probabilities, resulting in a net group velocity of zero. Remarkably, this average velocity can be determined without explicitly knowing the full dispersion relation, as it arises directly from the structure of the wavefunction and the underlying symmetries of the system. The Hellmann-Feynman theorem [107] is defined as

$$\frac{dE}{d\lambda} = \left\langle \Psi \middle| \frac{dH}{d\lambda} \middle| \Psi \right\rangle, \tag{4.13}$$

and for $\lambda = \vec{p}$, can be written as

$$\underbrace{\frac{dE}{\vec{p}} = \vec{v_g}}_{\text{slope of band}} \quad = \quad \underbrace{\left\langle \Psi \middle| \frac{\vec{p}}{m} \middle| \Psi \right\rangle}_{\text{average momentum}} , \tag{4.14}$$

where the slope of the band, v_g, is $\frac{\delta E_n}{\delta q}$, the average momentum $\left\langle \frac{\vec{p}}{m} \right\rangle$ is equal to $\Sigma_{p_x}\ p_x|\Psi(p_x)|^2$, and $|\Psi(p_x)|^2$ is the probability of p_x.

4.4 Experimental Characterization of Bose-Einstein Condensates in a Periodic Lattice Potential

Measurements presented here, were carried out by the adiabatic loading of a BEC in a 1d optical lattice potential. Our 1d optical lattice was created by retro-reflecting a far-detuned laser beam, with a 1064 nm wavelength and $\sim$ 150 μm waist. This yields a periodic trapping potential that allows for the study of a wide range of en-

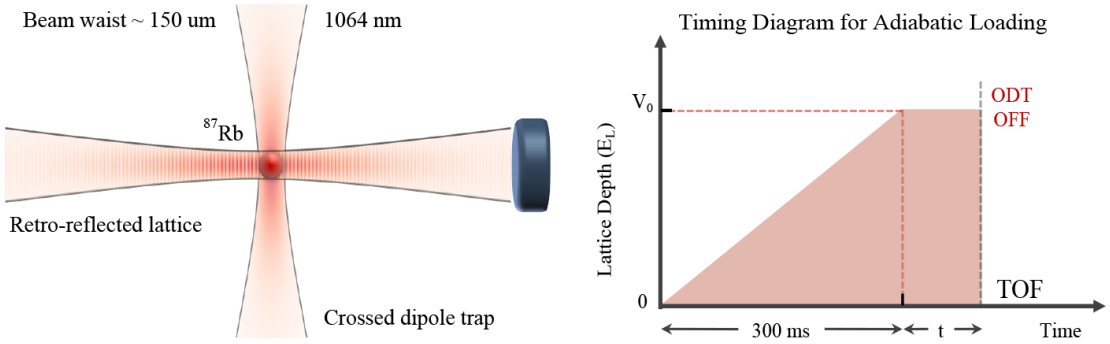

Figure 4.5: Experimental geometry and timing diagram for adiabatically transferring a BEC into an optical lattice potential. The retro-reflected lattice beam is along one of the directions of the crossed ODT. The potential is linearly ramped up to the final lattice depth in 300 ms, held for time t, and then snapped off simultaneously with the dipole trap.

gineered Hamiltonians in the laboratory. In the context of this thesis, it specifically enables the implementation of the Dirac Hamiltonian to simulate an analogue of the Sauter–Schwinger effect in Chapter 5.

4.4.1 Adiabatic Loading of a BEC into a Lattice Potential

The BEC, initially confined in an ODT, is adiabatically loaded into the optical lattice by slowly ramping up the optical lattice potential. If this ramp is sufficiently slow, the wave function of the condensate remains in the ground state of the system. Two key timescales determine adiabaticity during the loading of a BEC into an optical lattice. The first relates to the energy spacing between bands: if the lattice potential is ramped up too quickly, atoms may be excited into higher energy bands. The relevant timescale here is set by the energy spacing between bands, and the adiabaticity criterion for avoiding transitions from the lowest to the nth band in a non-interacting gas is discussed in Ref. [108].

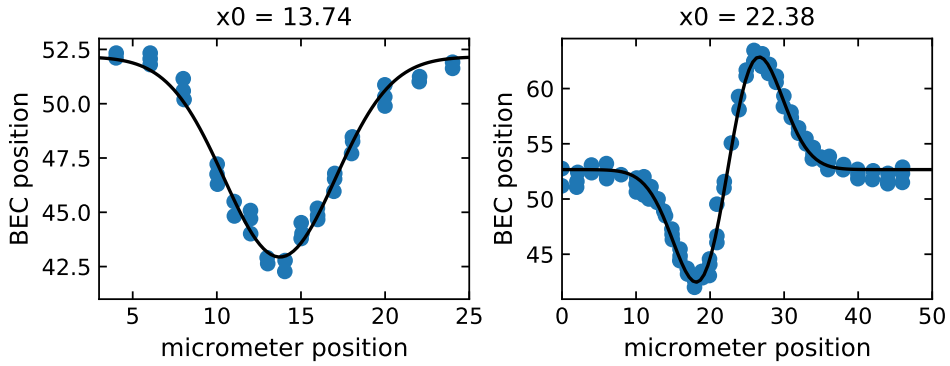

Figure 4.6: Utilizing dipole force for optical lattice laser beam alignment. Left plot: Trapping potential U(x) for a Gaussian beam propagating along $\hat{y}$, with waist ($1/e^2$ radii) of $w_0 = 150$ um. Right plot: The dipole force along x is $-dU/dx$; exhibits a linear dependence near the intensity maximum at $x = 0$.

The second timescale is associated with the external confinement: adiabaticity must also be maintained with respect to the effective trapping frequency along the direction of the lattice beam. This ensures that the BEC remains at the minimum of the modified dispersion curve as the potential is ramped on.

4.4.2 Lattice Alignment

Optimal alignment is achieved when the laser beam overlaps precisely with the BEC. To determine this, we prepare a BEC and suddenly illuminate it with a far-detuned 1064 nm laser beam for a 1/4 period of the transverse harmonic trap frequency. Since the retro-reflection is blocked, the atoms experience only a single-pass Gaussian beam profile. Immediately afterward, the BEC is released from all confining potentials and we perform absorption imaging after a duration of TOF. This procedure is commonly known as the trap-throw or trap-release technique.

To identify the optimal beam alignment, we calculate the trapping potential created

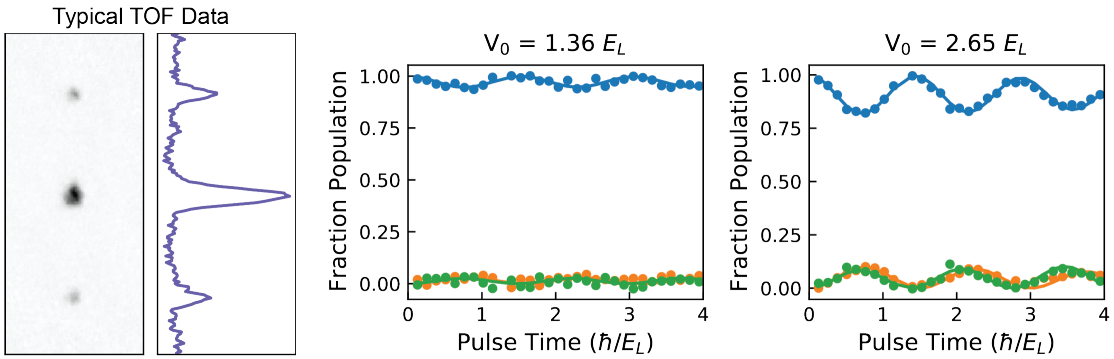

Figure 4.7: Calibrations of shallow lattice depths. Using TOF absorption images, we calibrate the depth of 1d lattices by studying atomic diffraction. The fractional populations, as a function of pulse time, are shown for two shallow lattice depths: $V_0 = 1.36$ $\mathrm{E_L}$ with an initial velocity $q = 0.03\ k_L$ and $V_0 = 2.65$ $\mathrm{E_L}$ with an initial velocity $q = 0.05\ k_L$.

by a propagating Gaussian beam and its corresponding dipole force, as illustrated in Figure 4.6. The dipole force, which is the spatial derivative of the Gaussian intensity profile, exhibits a linear dependence near the intensity maximum at $x = 0$. In this context, x denotes the relative position between the laser beam and the BEC. The point of maximum dipole force, corresponding to the center of the beam, defines the optimal alignment.

4.4.3 Lattice Depth Calibrations

The lattice was calibrated by using Kapitza-Dirac diffraction [109] of the BEC off a pulsed lattice potential. For the Sauter-Schwinger effect project, shallow lattice depths were required. We successfully loaded atoms into optical lattices with depths as low as $\approx 1E_L$, although calibration measurements indicated that the atoms had small initial velocities. Figure 4.7 shows the fractional populations in each state as a function of pulse time for two shallow lattice depths: $V_0 = 1.36$ $\mathrm{E_L}$ with an initial

velocity $q = 0.03\ k_L$ and $V_0 = 2.65\ \mathrm{E_L}$ with an initial velocity $q = 0.05\ k_L$. In both cases, the top curve represents the central order, at $kx = 0$, while the two lower curves correspond to the first diffraction orders, at $kx = \pm\ 2\ k_L$.

Lattice calibrations are performed by fitting the measured data to the time evolution governed by the optical lattice Hamiltonian. The system's dynamics are described using the time evolution operator $U(t) = e^{-\frac{i\hat{H}t}{\hbar}}$, which evolves the initial state forward in time. At $t = 0$, the wavefunction is taken to be a plane wave, $|\Psi(0)\rangle = |k_0\rangle$, representing an atom with a well-defined momentum prior to the lattice pulse. Time evolution of the lattice Hamiltonian demonstrates how the initial momentum state diffracts into a superposition of crystal momentum components, spaced by integer multiples of $2\ k_L$, due to the periodic nature of the lattice potential. By measuring the fractional populations in these crystal momentum orders as a function of lattice pulse duration and fitting them to the time evolution, the lattice depth V_0 can be accurately calibrated. This fitting procedure is sensitive to both the lattice parameters and the initial momentum distribution of the atoms, and is essential for precision control in lattice-based experiments.

4.4.4 Mapping Crystal Momentum to Free Particle Momentum

In typical TOF imaging, the optical lattice is rapidly switched off, and the resulting absorption image reflects the Fourier transform of the atomic wave function—effectively revealing the momentum distribution of atoms confined in the lattice. Alternatively, the lattice potential can be ramped down adiabatically. In this

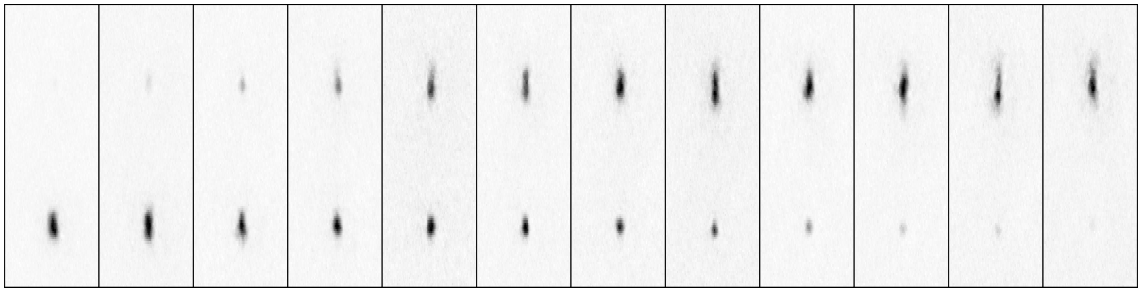

Figure 4.8: Series of TOF images capturing Bloch oscillations within the ground band, accompanied by Landau-Zener tunneling into the first excited band, all within the first Brillouin zone. The full Bloch oscillation time, t_{BL}, was 3.7 ms at a lattice depth of $V_0 = 3.31\ \mathrm{E}_L$.

case, an atom initially with crystal momentum q will be mapped onto a free-particle momentum state with $p = q$ after the lattice is fully turned off. This mapping provides direct access to the crystal momentum distribution in the lattice. In higher dimensions, the situation is more complex due to the structure of the Brillouin zones, but the same principle applies: the population in the nth energy band is adiabatically mapped to the nth Brillouin zone in the momentum distribution.

4.4.5 Bloch Oscillations & Landau-Zener Tunneling

Bloch oscillations arise when atoms in an optical lattice are subjected to a constant external force, such as gravity, an applied magnetic field gradient or as in our case, a displaced ODT beam. This displacement applies a "kick", or rather a force, that causes the atoms to undergo periodic motion in momentum space, with their crystal momentum q evolving linearly in time according to $\boldsymbol{F} = \hbar\frac{d\boldsymbol{q}}{dt}$, where $\boldsymbol{F}$ is the applied force, and reflecting at the edges of the first Brillouin zone. This leads to an oscillatory motion in real space, a direct consequence of the lattice's periodic band structure and the bounded nature of crystal momentum. [110] Bloch

oscillations manifest as oscillations in the momentum of the atomic cloud and can be directly observed using TOF imaging and band-mapping techniques. Figure 4.8 presents a series of TOF images capturing Bloch oscillations within the ground band, accompanied by Landau-Zener tunneling into the first excited band, all within the first Brillouin zone. The full Bloch oscillation time, t_{BL}, was 3.7 ms at a lattice depth of $V_0 = 3.31\ \mathrm{E}_L$, as used in the Sauter-Schwinger experiment, where Bloch oscillations along with Landau-Zener tunneling served as a mechanism for simulating particle–antiparticle pair production.

4.5 Conclusions and Outlook

Optical lattices have been a foundational tool in both theoretical and experimental physics for several decades now, particularly within the field of ultracold atoms [4, 111, 112]. Their high degree of tunability and dynamic control makes them ideal platforms for simulating a wide range of quantum phenomena. Here, optical lattices enable the engineering of effective Dirac Hamiltonians, allowing for experimental analogues of high-energy processes such as vacuum pair production under extremely strong electric fields—regimes that are otherwise inaccessible with current experimental capabilities.

Chapter 5: Sauter-Schwinger Effect with Bose-Einstein Condensates

This chapter presents an experiment quantum simulating the Sauter-Schwinger effect with BECs and is a reprint of my previous work published in Ref. [36] with additions.

The Sauter-Schwinger effect [31–35] predicts the creation of particle-antiparticle pairs from the quantum vacuum when a large electric field is present. This phenomenon arises out of quantum electrodynamics (QED) and the associated pair-creation probability is exponentially suppressed for field strengths below the critical field $E_c \approx 10^{18}$ V/m. Electric fields on this scale are not experimentally accessible; even the largest laboratory fields produced by ultrashort laser pulses [113] fall short, making direct observation of pair creation out of reach of current experiments. Subsequently, analog experiments have been proposed that simulate high-field effects with laboratory accessible energy scales in cold atoms [114–117], graphene [118–123], and other condensed matter systems [119, 124–126].

The high degree of experimental control and direct measurement techniques present in ultracold atomic systems allow for quantitative laboratory analogs with quantum gases in an optical lattice. To experimentally probe the Sauter-Schwinger effect with a bosonic quantum gas, we engineered the relativistic 1d Dirac Hamiltonian with mc^2 reduced by 17 orders of magnitude, allowing laboratory scale forces to greatly exceed the Sauter-Schwinger limit, as published in Ref. [36]. The Dirac picture of

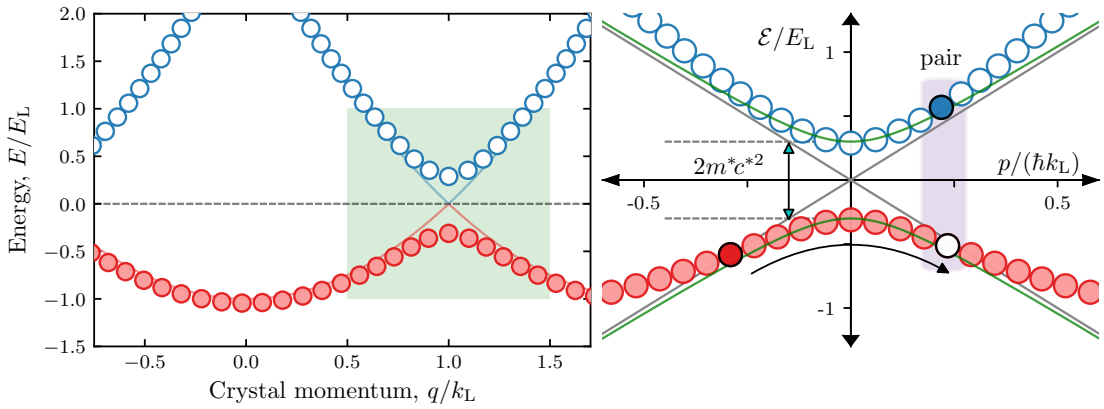

Figure 5.1: 1d Dirac model approimated by optical lattice band structure. The left panel shows the lowest two bands of a 1d optical lattice and the right panel shows an expanded view at the edge of the Brillouin zone. In both cases, the dispersion of the lower (or "antiparticle") band is denoted by red circles and the upper (or "particle") band is denoted by blue circles. The expanded view reveals the connection to the 1d Dirac equation (green shaded region in left panel). The gray lines plot the linear dispersion of massless particles, while the green curves depict the Dirac-dispersion computed from equation 5.3. The curved arrow illustrates the process of pair creation where an occupied state in the antiparticle band is converted to an occupied state in the particle band and a vacancy in the antiparticle band.

particle-antiparticle vacuum and the concept of optical lattice band theory is the foundation of our approach. In this framework, we readily measured pair creation and demonstrated that this high-field phenomenon is well-characterized by Landau-Zener tunneling [127, 128] as was discussed in Refs. [119, 124–126].

In the Dirac vacuum, the enormous required electric field

$$E_c = m_e^2 c^3 / \hbar q_e \tag{5.1}$$

is determined by the particle/antiparticle mass m_e and charge q_e. For an applied electric field E, the pair creation rate is governed only by the dimensionless ratio

E/E_{c}:

$$\frac{m_e c^2}{1E_{\mathrm{L}}} = \frac{8.187 \times 10^{-14}\,\mathrm{J}}{1.34 \times 10^{-30}\,\mathrm{J}} = 6.109 \times 10^{16}. \tag{5.2}$$

This allows our physical system with very different characteristic scales to be used to realize the underlying phenomenon with reduced energy scales.

We construct two experiments: (1) We studied how pair production depends on the force strength and rest mass. Then draw an analogy to Landau-Zener tunneling. (2) We modeled a uniformly filled Dirac vacuum and investigate pair production as a function of time. From results of the experiments we confirm that the experimental analog of pair production can be interpreted in the framework of Landau-Zener tunneling.

5.1 1d Dirac Hamiltonian

Our system was well described by the 1d Dirac Hamiltonian [97, 124, 129–131]

$$\hat{H}_{\mathrm{D}} = c\hat{p}\sigma_z + mc^2\sigma_x, \tag{5.3}$$

where $\hat{p}$ is the momentum operator and $\sigma_{x,y,z}$ are the Pauli operators. Starting with $m = 0$, the 1d Dirac Hamiltonian describes particles with velocities $\pm c$, that are then coupled with strength mc^2 to give the familiar $\mathcal{E}(p) = \pm(p^2c^2 + m^2c^4)^{1/2}$ dispersion relation for relativistic particles and antiparticles. At zero momentum, this dispersion has a gap equal to twice the rest mass, at which point the curvature

Table 5.1: Comparison of scales between relativistic electronic systems and our analog atomic system.

	Dirac theory	Analog atomic system
Rest mass	$mc^2 \approx 0.5$ MeV	$m^*c^{*2} = V/4 \approx 10^{-11}$ eV
Speed of light	$c = 299\ 792\ 458$ m/s	$c^* = \hbar k_{\mathrm{L}}/m_{\mathrm{Rb}} \approx 4.3$ mm/s
Compton length scale	$\lambda_{\mathrm{C}} = h/mc \approx 10^{-12}$ m	$\lambda^*_{\mathrm{C}} = h/m^*c^* \approx 10^{-6}$ m

is inversely proportional to the rest mass. The Dirac vacuum consists of occupied states in the lower (antiparticle) band of the Dirac dispersion and vacant states in the upper (particle) band. Vacancies in the antiparticle band represent antiparticles and occupied states in the particle band represent particles. We explored the Sauter-Schwinger limit for pair creation by measuring the probability and rate of pairs production out of this vacuum as a function of the effective rest mass and applied force.

5.2 Atomic System: 1d Optical Lattice Model

We emulated the Dirac Hamiltonian $\hat{H}_{\mathrm{D}}$ with the lowest two bands of a 1d optical lattice (see Chapter 4) at the edge of the Brilloiun zone with the approximate Hamiltonian

$$\hat{H}_{\mathrm{L}} = \frac{\hbar k_{\mathrm{L}}}{m} p\sigma_z + \frac{V}{4}\sigma_x, \tag{5.4}$$

giving the pair of relativistic modes shown in figure 5.1. Within this close proximity to the edge of the Brillouin zone, the curvature of the two bands are equal and

opposite. The mapping between the scales in $\hat{H}_{\mathrm{D}}$ and the analog quantities in $\hat{H}_{\mathrm{L}}$ are outlined in table 5.1. The effective rest mass $m^*c^{*2} = V/4$ is set by the peak-to-valley lattice depth V generated by our $\lambda_{\mathrm{L}} = 1064$ nm laser light. The speed of light is replaced by the greatly reduced speed of light $c^* = \hbar k_{\mathrm{L}}/m_{\mathrm{Rb}} \approx 4.3$ mm/s equal to the single photon recoil velocity. The single photon recoil momentum $\hbar k_{\mathrm{L}} = 2\pi\hbar/\lambda_{\mathrm{L}}$ specifies the recoil energy $E_{\mathrm{L}} = \hbar^2 k_{\mathrm{L}}^2/2m_{\mathrm{Rb}} = h \times 2.02$ kHz. These recoil units set the scale for all physical quantities in our analog system. The effective Compton wavelength $\lambda_{\mathrm{C}} = h/m^*c^* = 8\lambda_{\mathrm{L}}E_{\mathrm{L}}/V$ is about 10^6 times larger than that of an electron.

Our simulations began with ultracold bosons prepared in the antiparticle band, then subjected to a constant force, $F_{\mathrm{e}} = q_{\mathrm{e}}E = \hbar dq/dt$, modeling an electric field. During the application of this force atoms may transfer from the antiparticle band to the particle band, emulating the pair creation phenomenon. We measured the fraction of atoms transferred to the particle band as a function of the effective rest mass and the applied force. Our experiments began by using a Bose-Einstein condensate to illucidate the connection between Landau-Zener tunneling and pair creation; we then model the Dirac vacuum by uniformily filling the Brillouin Zone of the antiparticle band and observe the predicted rate of pair creation.

5.2.1 Bare Eigen-Energies and the Free Particle

In the absence of the lattice potential, the system exhibits the free-particle dispersion, represented by the solid curves in figure 5.1. Starting from the truncated 3×3

matrix form of the 1d optical lattice Hamiltonian [see eq. 4.10], and evaluating it for the bare eigenstates, i.e., with $V = 0$, we recover the following dispersion relations:

$$\frac{\hbar^2 q^2}{2m} \quad \text{and} \quad \frac{\hbar^2}{2m}(q - 2k_{\mathrm{L}})^2. \tag{5.5}$$

To gain insight into the structure near the Brillouin zone edge, we Taylor expand these expressions about $q = k_{\mathrm{L}}$. Using $f(q) \approx f(k_{\mathrm{L}}) + f'(k_{\mathrm{L}})(q - k_{\mathrm{L}})$, we obtain:

$$\frac{\hbar^2 q^2}{2m} \approx \frac{\hbar^2 k_{\mathrm{L}}^2}{2m} + \frac{\hbar^2 k_{\mathrm{L}}}{m}(q - k_{\mathrm{L}}), \tag{5.6}$$

$$\frac{\hbar^2}{2m}(q - 2k_{\mathrm{L}})^2 \approx \frac{\hbar^2 k_{\mathrm{L}}^2}{2m} - \frac{\hbar^2 k_{\mathrm{L}}}{m}(q - k_{\mathrm{L}}). \tag{5.7}$$

Combining these results, we find that the effective Hamiltonian expanded around $q = k_{\mathrm{L}}$ takes the form:

$$H_{\mathrm{L}} = \frac{\hbar^2 k_{\mathrm{L}}^2}{2m} 1 + \frac{\hbar^2 k_{\mathrm{L}}^2}{m}\left(\frac{q}{k_{\mathrm{L}}} - 1\right)\begin{pmatrix} 1 & 0 \\ 0 & -1 \end{pmatrix}, \tag{5.8}$$

where the bare eigen-energies are then

$$E = E_{\mathrm{L}} \pm 2E_{\mathrm{L}}(q_d - 1). \tag{5.9}$$

Notice, that with the lattice potential V turned on, coupling occurs most significantly between $|q\rangle$ and $|q - 2k_{\mathrm{L}}\rangle$. Truncating to this two-level subspace (centered at $q \approx k_{\mathrm{L}}$), and keeping only the lowest-order coupling term, the effective Hamiltonian

becomes precisely the 1d Dirac Hamiltonian in equation 5.3.

The energy gap $\Delta = V$ opens between the bands at $q = k_{\mathrm{L}}$, separating the particle and antiparticle bands. This representation highlights the Dirac-like dynamics emerging in the vicinity of the zone edge in an optical lattice. This effective model captures both the linear dispersion near the crossing point and the mass gap induced by the lattice. The analogy to the Dirac equation becomes exact in the low-energy limit near the avoided crossing. Lastly, the strength of V can be adjusted to tune the effective mass m^* in experiments.

5.3 Landau-Zener Diabatic Transition Probability

Within the Landau-Zener framework [127, 128], the diabatic transition probability characterizes how likely the system is to remain in its initial eigenstate when the evolution is non-adiabatic, and is

$$P_{LZ} = e^{-2\pi\Gamma}, \text{with } \Gamma = \frac{a^2/\hbar}{|\frac{dq}{dt}\frac{\delta}{\delta q}\Delta E|}. \tag{5.10}$$

Using the results from equation 5.9, the energy difference between the bare states of the upper and lower bands of the optical lattice in the free particle limit is

$$\Delta E = E_{\mathrm{L}} + 2E_{\mathrm{L}}(q_d - 1) - E_{\mathrm{L}} + 2E_{\mathrm{L}}(q_d - 1) \tag{5.11}$$

$$= 4E_{\mathrm{L}}(q_d - 1). \tag{5.12}$$

Taking the derivative of the energy gap ΔE with respect to time gives

$$\frac{\delta}{\delta t}\Delta E = \frac{\delta}{\delta t}[4E_{\mathrm{L}}(q_d - 1)] \tag{5.13}$$

$$= 4E_{\mathrm{L}}\frac{dq_d}{dt}. \tag{5.14}$$

This result will be used to evaluate the Landau-Zener tunneling parameter Γ, which characterizes the diabatic transition probability. Our Landau-Zener expression now takes the form:

$$\Gamma = \frac{s^2E_{\mathrm{L}}^2}{16\hbar|4E_{\mathrm{L}}\frac{dq_d}{dt}|} = \frac{s^2E_{\mathrm{L}}}{64\hbar(\frac{2}{t_{Bl}})} = \frac{s^2E_{\mathrm{L}}t_{Bl}}{128\hbar}, \tag{5.15}$$

where a = $sE_{\mathrm{L}}/4$ is the off-diagonal coupling between states, $\frac{\delta}{\delta t}\Delta$E from equation 5.14, and the sweep rate $d\boldsymbol{q_d}/dt = \boldsymbol{F} = 2\hbar k_{\mathrm{L}}/t_{\mathrm{Bl}}$.

5.4 Relation Between Force & Γ Parameter

To obtain the relationship between force and the Landau-Zener tunneling parameter Γ, we can use the relation for the momentum change under a constant force:

$$F = \frac{dp}{dt} = q_eE, \tag{5.16}$$

$$\Rightarrow \quad \frac{dp}{dt} = \frac{2\hbar k_{\mathrm{L}}}{t_{\mathrm{Bl}}}, \tag{5.17}$$

Converting this to a quasimomentum sweep rate gives

$$\frac{dq_d}{dt} = \frac{F}{2\hbar} = \frac{1}{2\hbar} \cdot \frac{2\hbar k_{\mathrm{L}}}{t_{\mathrm{Bl}}} = \frac{k_{\mathrm{L}}}{t_{\mathrm{Bl}}}. \tag{5.18}$$

Alternatively, the sweep rate can be defined as $\frac{dq_d}{dt} = \frac{2}{t_{\mathrm{Bl}}}$, then the final form becomes exactly as defined in equation 5.15.

5.4.1 Critical Force from Schwinger's Limit

To identify the analog of Schwinger's critical force in our atomic system, we begin by equating it to the original relativistic expression and translating it into optical lattice parameters:

$$F_{\mathrm{S}} = q_e E_{\mathrm{S}} \Rightarrow \frac{m_e^2 c^3}{\hbar} = \frac{(m_e c^2)^2}{\hbar c} \tag{5.19}$$

$$= \frac{(V_o)^2}{\hbar} \left(\frac{m_{Rb}}{\hbar k_{\mathrm{L}}} \right) \tag{5.20}$$

$$= \frac{s^2 E_{\mathrm{L}} k_{\mathrm{L}}}{32} \tag{5.21}$$

Here, Schwinger's critical force is substituted with the analog parameters in the cold atom context, where $V_0 = \frac{sE_{\mathrm{L}}}{4}$, and the effective mass $m^* = \frac{4\hbar^2}{sE_{\mathrm{L}}} \cdot k_{\mathrm{L}}$.

We now arrive at the final relationship connecting the applied force F and the dimensionless Landau-Zener parameter Γ. Starting from the previously derived expression:

$$\Gamma = \frac{s^2}{128} \frac{E_{\mathrm{L}}}{\hbar} t_{\mathrm{Bl}}, \tag{5.22}$$

we multiply both sides by the force experienced by an atom during Bloch oscillations, given by

$$F = \frac{2\hbar k_{\mathrm{L}}}{t_{\mathrm{Bl}}},$$

yielding:

$$\Gamma \times F = \frac{s^2}{64} E_{\mathrm{L}} k_{\mathrm{L}}. \tag{5.23}$$

Now, expressing the lattice depth parameter s in terms of the analog rest mass energy $mc^2 = \frac{sE_{\mathrm{L}}}{4}$, we get:

$$s = \frac{4mc^2}{E_{\mathrm{L}}} \tag{5.24}$$

Substituting into the expression for $\Gamma \times F$:

$$\Gamma \times F = \frac{m^2c^3}{4\hbar} \cdot \left(\frac{\hbar k_{\mathrm{L}}}{E_{\mathrm{L}}/c} \right). \tag{5.25}$$

Using $v_{\mathrm{L}} = \frac{E_{\mathrm{L}}}{\hbar k_{\mathrm{L}}} \Rightarrow \frac{\hbar k_{\mathrm{L}}}{E_{\mathrm{L}}} = \frac{1}{v_{\mathrm{L}}}$, and identifying $c = v_{\mathrm{L}}$ in our analog system, this can be simplified to:

$$\Gamma \times F = \frac{m^2c^3}{4\hbar} = \frac{F_{\mathrm{S}}}{2}, \tag{5.26}$$

where $F_S = \frac{m^2c^3}{\hbar}$ is the analog of Schwinger's critical force. And the final result:

$$\frac{F}{F_S} = \frac{1}{2\Gamma}. \tag{5.27}$$

5.5 Experimental Characterization

Our experiments began with nearly pure ^{87}Rb Bose-Einstein condensates (BECs) in the $|F = 1, m_F = -1\rangle$ internal state, in a crossed optical dipole trap [132] formed at the intersection of two laser beams traveling along $\mathbf{e}_x$ and $\mathbf{e}_y$, giving trap frequencies $(f_x, f_y, f_z) = (44, 45, 94)$ Hz. The low density of our $N \approx 10^3$ atom BECs limited unwanted scattering processes in regimes of dynamical instability [133]. The optical lattice potential was formed by a retro-reflected $\lambda = 1064$ nm laser beam with a waist of ≈ 150 μm. Emulated electric forces were applied by spatially displacing the optical dipole beam providing longitudinal confinement (by frequency shifting an acousto-optic modulator). This effectively added a linear contribution to the existent harmonic potential for displacements small compared to the beam waist. We loaded BECs into the optical lattice by linearly increasing the lattice laser intensity from zero to the final intensity in 300 ms, a time-scale adiabatic with respect to all energy scales. Once the final lattice depth (determined by the laser intensity) was achieved, we applied a force for a time t_F. The lattice was calibrated by using Kapitza-Dirac diffraction of the BEC off a pulsed lattice potential [109], as discussed in Chapter 4. Immediately thereafter, the lattice was linearly ramped off in 1 ms, mapping crystal momentum states to free particles states [134–137]. This process

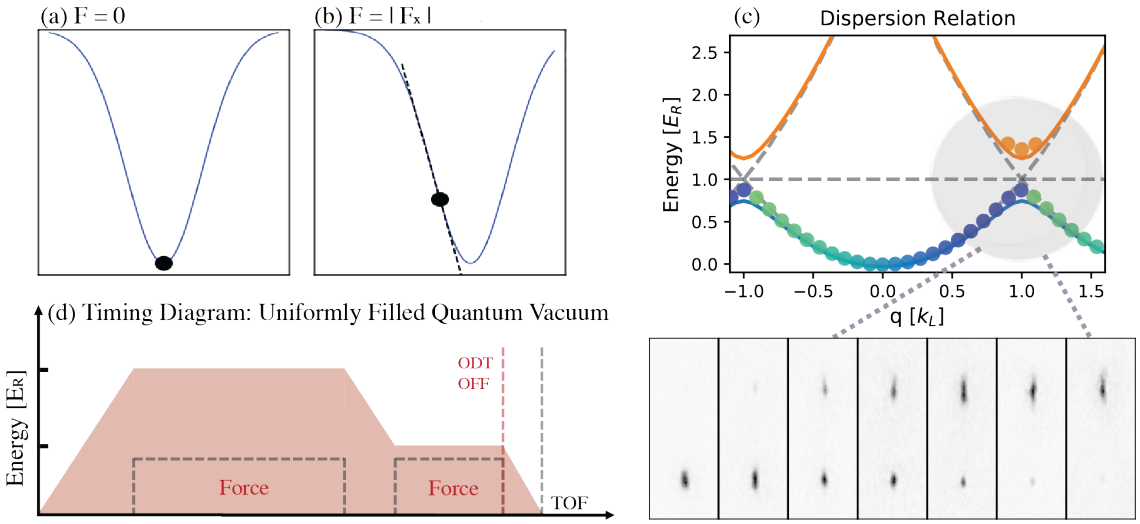

Figure 5.2: Application of an emulated constant electric force by spatially displacing the optical dipole beam. This effectively added a linear contribution to the existent harmonic potential for displacements small compared to the beam waist. (a) When atoms are located at the center (minimum) of the harmonic potential, they experience no net force. (b) Displacing the beam to the right creates a locally linear potential, resulting in a constant positive force on the atoms. (c) Dispersion relation for a 1d optical lattice potential, depicting Bloch oscillations, induced by a constant electric force, within the ground band, accompanied by Landau-Zener tunneling into the first excited band at the edge of the first Brillouin zone. Accompanied by the corresponding TOF images. The full Bloch oscillation time, t_{BL}, was 3.7 ms at a lattice depth of $V_0 = 3.31\ \mathrm{E}_L$. Lastly, (d) shows the timing diagram for the analog Dirac vacuum. Atoms were adiabatically loaded into the lattice over a duration of 300 ms. This initial state was prepared by adiabatically loading a BEC into a relatively deep optical lattice ($V \approx 3.4\ E_{\mathrm{L}}$), in 300 ms, ensuring well-separated energy bands. A constant force was then applied for 1 s—sufficient to induce approximately 300 Bloch oscillations. During this time, crystal momentum-changing collisions and dephasing processes led to uniform population of the antiparticle band. Finally, we adiabatically reduced the lattice depth over 300 μs, resulting in an effective rest energy of $m^* c^{*2}/E_{\mathrm{L}} = 0.20(1)$.

mapped atoms in the anti-particle band to free particle states with momentum between $-k_{\mathrm{L}}$ and k_{L}, and mapped atoms in the particle band to states between $\pm k_{\mathrm{L}}$ and $\pm\, 2\, k_{\mathrm{L}}$. The resulting momentum distribution was absorption imaged after a 15.7 ms time-of-flight (TOF).

5.5.1 Emulated Electric Forces

Emulated electric forces were applied by spatially displacing the optical dipole beam providing longitudinal confinement. This was done by frequency shifting an acousto-optic modulator. This effectively added a linear contribution to the existent harmonic potential for displacements small compared to the beam waist. This application of emulated electric forces is illustrated in figure 5.2, along with the corresponding TOF images. In plot 5.2 (a), atoms positioned at the center of the harmonic potential (the minimum of the Gaussian beam) experience no net force. In plot 5.2 (b), displacing the beam to the right creates a locally linear potential, resulting in a constant positive force on the atoms. Plot 5.2 (c) shows the dispersion relation for a 1D optical lattice potential, depicting Bloch oscillations induced by a constant electric force. These oscillations originate in the ground band and are accompanied by Landau-Zener tunneling into the first excited band at the edge of the first Brillouin zone. The full Bloch oscillation time, t_{BL}, was 3.7 ms at a lattice depth of $V_0 = 3.31\ \mathrm{E}_L$.

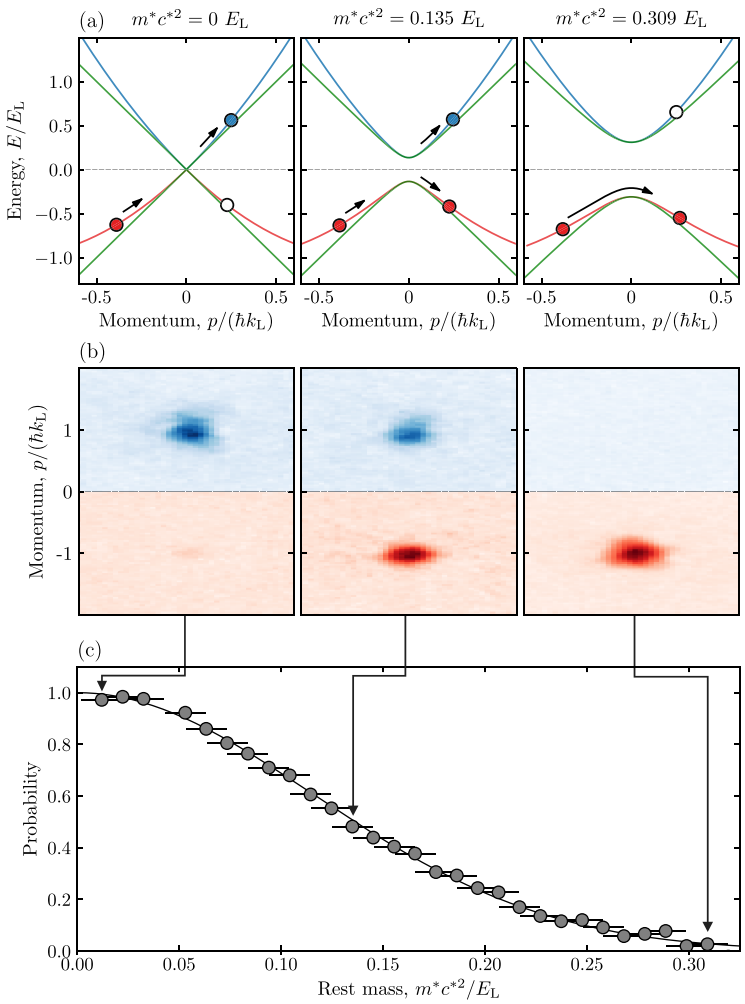

Figure 5.3: Pair creation from a single state with electric force $F_e = 2\hbar k_L/t_F$ applied for a time $t_F = 3.7$ ms. (a) Schematic representation of pair-creation for effective rest mass m^*c^{*2} $(0.012(1), 0.134(9), 0.309(1))E_L$. In each case the green curves denote the Dirac dispersion, and the blue and red curves denote the particle and anti-particle bands respectively. (b) TOF images showing the fractional populations of atoms occupying the particle band (blue tone) and antiparticle band (red tone) for each m^*. (c) Probability of pair creation as a function of effective rest mass, plotted along with the Landau-Zener model from eq. 5.4. Statistical uncertainties are shown with typical error bars.

5.6 Pair Creation From a Single Occupied State

We began with an experiment that is natural in the cold atom setting but is unphysical in high-field physics: we applied an effective electric field and varied the

effective rest mass. The result of this changing effective mass is schematically shown in figure 5.3 (a) by an increasing gap at zero momentum. The decreasing probability of pair creation with increasing effective mass anticipated by equation 5.2 is schematically illustrated by the filled or partially filled circles. Figure 5.3 (b) shows the distribution of atoms at time t_F selected so that the atoms traversed a full Brillouin zone, i.e., underwent a single Bloch oscillation [110]. Atoms in the top portion of the panel (blue tone) represent particles and atoms in the bottom portion of the panel (red tone) denote filled vacuum states. Figure 5.3 (c) quantifies this effect in terms of the fractional population of a BEC transferred into the particle band, and as expected, the probability of pair creation monotonically decreased with increasing effective rest mass. For small effective rest masses, the atoms almost completely populated the particle band, while for large effective mass the particle band was nearly empty. The solid curve in figure 5.3 (c) plots the Landau-Zener diabatic transition probability [127, 128, 130, 138–140] given by

$$P_{\mathrm{LZ}} = e^{-2\pi\Gamma}, \text{with } \Gamma = \frac{a^2}{\hbar|\frac{d}{dt}\Delta E|}, \tag{5.28}$$

describing the transit through a crossing with gap $a = 2m^*c^{*2}$ while the massless energy difference $E(p) = 2c^*p$ changes as p is swept at constant rate dp/dt; this rate sets the electric force $F_{\mathrm{e}} = q_{\mathrm{e}}E$. Remarkably in terms of these parameters, the Landau-Zener coefficient is defined by $F_{\mathrm{e}}/F_{\mathrm{c}} = 1/2\Gamma$ where $F_{\mathrm{c}} = q_{\mathrm{e}}E_{\mathrm{c}}$ is an exact analog of Sauter-Schwinger's limit of pair creation, and as shown in the previous section. This prediction is in near perfect agreement with data in figure 5.3 (c).

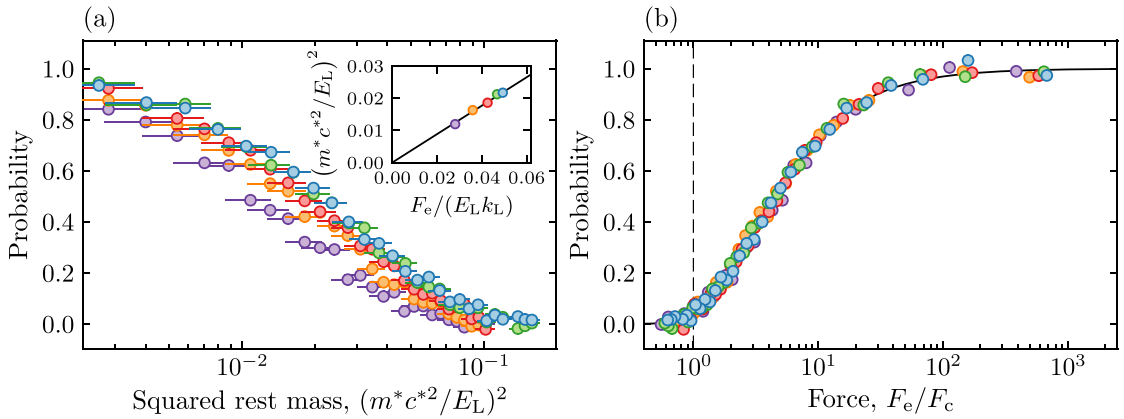

Figure 5.4: (a) Probability of pair creation as a function of effective rest mass squared for $F_e = 2\hbar k_L/t_F$ and $t_F = (3.2, 3.4, 3.7, 4.4, 5.6)$ ms, suggesting a common functional form. Statistical uncertainties are shown with typical error bars. The inset quantifies the scaling relationship between these curves in terms of the point where each curve reaches half-max, in agreement with the prediction of eq. 5.4, shown by the black line. (b) Probability of pair creation plotted as a function of dimensionless force F_e/F_c, showing collapse onto a single curve. The vertical dashed line marks Sauter-Schwinger's limit where $F_e = F_c$, and the solid curve is the prediction of eq. 5.4.

As suggested by the quadratic dependence on mass in equation 5.2, figure 5.4 (a) plots the probability of pair creation as a function of effective rest mass squared for 5 different forces, illustrating their similar behavior. The inset figure confirms the agreement with the Landau-Zener expression by plotting the effective rest mass required to achieve a 50% probability of pair creation as a function of the field strength, and the solid curve shows good agreement with the Landau-Zener prediction.

Figure 5.4 (b) displays the same data (circles) now as a function of F_e/F_c that collapses onto the predicted transition probability (solid curve). This collapse confirms that the physics of pair creation exhibits universal behavior when the field is expressed in units of F_c as predicted by the Landau-Zener expression. The vertical dashed line marks the ratio $F/F_c = 1$, the Sauter-Schwinger limit for pair creation;

much of our data is in the high-field limit, which is extremely difficult to achieve in other physical contexts. Our data densely samples the critical regime near F_c and spans the full gamut from vanishing pair creation to nearly complete pair creation. Together these data show the clear connection between the Landau-Zener tunneling of a single quantum state and the Sauter-Schwinger effect. Still, the single occupied state defined by our BEC is far from the Dirac vacuum state.

5.7 Uniformly Filled Quantum Electrodynamic Vacuum

We therefore created an initial state mimicking the Dirac vacuum in which the negative energy states were occupied with equal probability and the positive energy states were vacant. We prepared this state by first adiabatically loading a BEC into a fairly deep optical lattice ($V \approx 3.4E_L$, making the lowest bands well separated) and applied a force for 1 s, sufficient for about 300 Bloch oscillations to take place [110]. During this time, crystal momentum changing collisions [133] and dephasing processes uniformly filled the antiparticle band. We then adiabatically reduced the lattice depth in 300 μs giving $m^*c^{*2}/E_L = 0.20(1)$, and proceeded as described in the experimental methods section. Here, pairs were produced at a constant rate for the entire time t_F the force was applied, filling initially vancant states in the particle band while depleting initially occupied states in the antiparticle band. Figure 5.5 (a) shows the atomic momentum distribution following this procedure for small (dashed curve) and larger (solid curve) values of t_F. In these data the states in the antiparticle band fall in the pink region, and states in the particle band fall

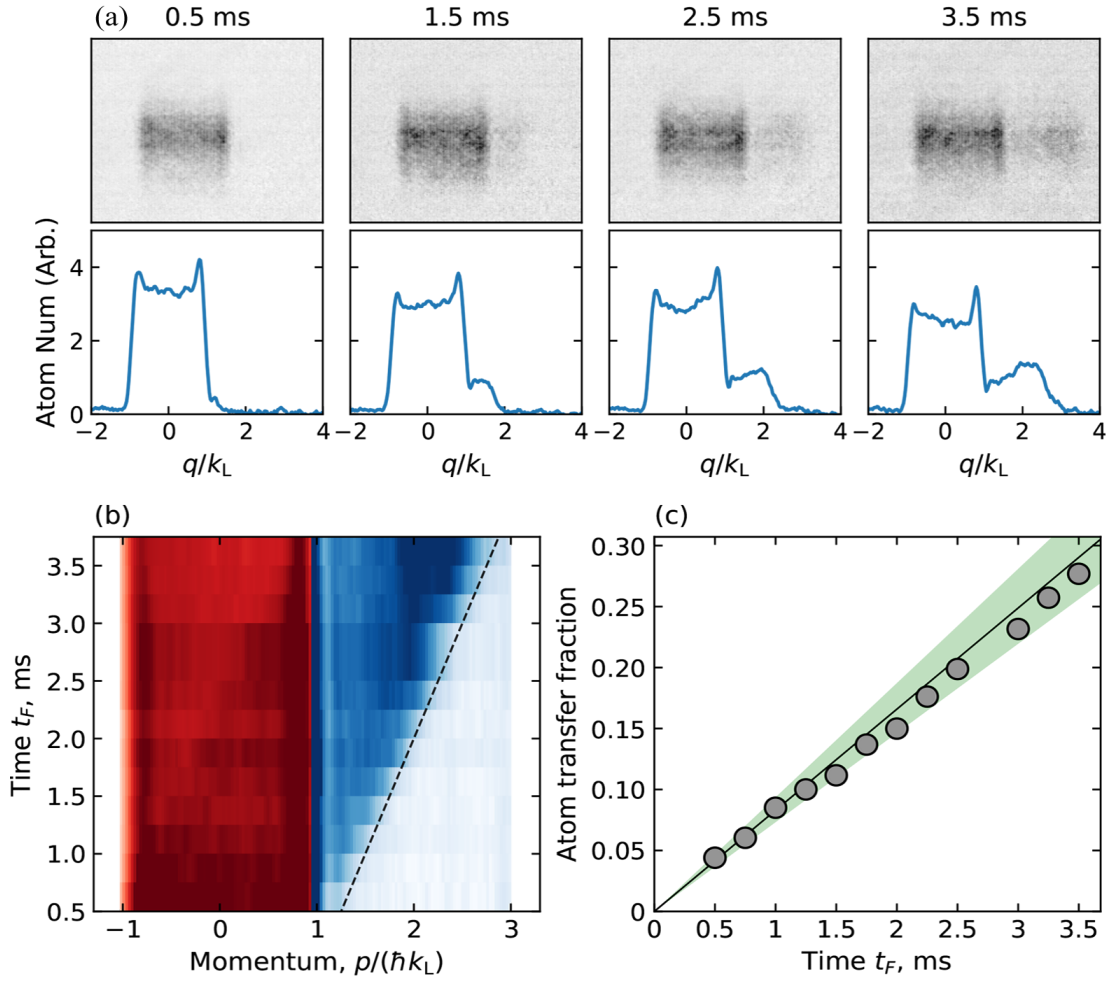

Figure 5.5: Time dependence of pair creation from the Dirac vacuum using the force $dq/dt = 2\hbar k_L/t_{2k_L}$ derived from the single Bloch oscillation time $t_{2k_L} = 3.4$ms. (a) Momentum distribution following the application of a force for short to long hold times. (b) Time-dependence of pair-creation showing the appearance of and acceleration of particle states and the depletion and deceleration of antiparticle states as a function of time. The red regions and blue regions mark states in the anti-particle and particle bands respectively. The dashed line marks the acceleration expected from the applied force alone. Both the slight wedge shape of the particle-state distribution in (a) and the slight shift from the dashed line in (b) result from the harmonic confining potential. (c) Observed fractional transfer of atoms as a function of time plotted along with the prediction of eq. 5.4. The green shaded area represents the uncertainty from input parameters.

in the blue regions. A uniformly filled initial band would ideally produce a top-hat distribution in the pink region; we confirmed that the observed time-independent

peaks in the distribution are consistent with a slight defocus of our imaging system [141–143]. The evolution from the dashed curve to the solid curve clearly shows particles that have been created and then accelerated by F_{e}. Figure 5.5 (b) summarizes data of this type for variable t_F, making clear the appearance of particles already visible in figure 5.5 (a), but also showing a similar reduction of occupation in the antiparticle band. The dashed line marks the anticipated acceleration given by F_{e}; the slightly reduced observed acceleration results from the harmonic confining potential. Finally, figure 5.5 (c) plots the fractional occupation probability of the particle band, clearly showing the creation of pairs at a constant rate. The line plots the rate, computed from the transition probability in equation 5.4, using the force $dq/dt = 2\hbar k_{\mathrm{L}}/t_{2k_L}$ derived from the single Bloch oscillation time $t_{2k_L} = 3.4$ ms for these data. This then is the direct analog of the constant rate of pair creation from vacuum from a uniform electric field.

5.8 Conclusion and Outlook

In this experiment, we used an ultracold atomic system to quantitatively probe both the underlying mechanism and the overall phenomena of pair creation as initially conceived of in high-field physics. Our analysis shows that pair creation in an analog atomic system can be equivalently understood as a quantum tunneling process, and our data spans the full parameter regime from low applied field (negligible pair creation) below the Sauter-Schwinger limit, to high field (maximum rate of pair creation) far in excess of the Sauter-Schwinger limit. High-intensity pulsed

laser experiments [113, 144–147] promise to measure the vacuum non-linearity and ultimately exceed Sauter-Schwinger's limit in its original context. Current theory suggests that actual pair creation threshold will be somewhat in excess of E_c resulting from the Coulomb attraction between electron-position pairs. Future cold atom experiments with repulsively interacting fermions could probe this "excitionic" shift as well, allowing more quantitative comparison with higher order corrections to the threshold field strength. In addition, the pair-creation phenomena occurring in strongly interacting field theories, even absent applied electric fields, may also be realized using mixtures of ultracold bosons and fermions [116, 117] and has already been realized using trapped ions [148].

Chapter 6: Floquet Engineering

A bipartite magnetic lattice is a versatile optical lattice configuration that has enabled experimental realizations of topological systems with rich and nontrivial properties. Notable examples include a quantum geometric "charge" pump implemented with ultracold atoms [90], as well as nonadiabatic schemes that generate unidirectional, constant spin flows—such as spin-dependent bipartite Floquet lattices [37] and dynamically induced symmetry breaking in out-of-equilibrium topological systems [89].

This chapter focuses on the one-dimensional (1d) bipartite magnetic lattice model underlying the latter two pulblished works, and outlines parts of the work presented in Ref. [37], where a Floquet "switching" protocol was implemented. In this scheme, the lattice periodically alternates between two distinct configurations, effectively simulating the Su–Schrieffer–Heeger (SSH) Hamiltonian [149] and the Rice–Mele (RM) Hamiltonian [150], respectively.

6.1 1d Bipartite Magnetic Lattice

Our experimental realization of a 1d bipartite spin dependent lattice in the laboratory is accomplished via the interplay of two Raman fields and one radio frequency (rf) magnetic field with a well defined phase with respect to the Raman fields, coupling the $|f = 1, m_f = 0, \pm 1\rangle$ internal states of the ground state manifold of ^{87}Rb

as shown in Fig 1a-c. The Raman wavelength $\lambda = 2\pi/k_R$ and recoil energy $E_R = \hbar^2 k_R^2/2m$ are the natural length and energy scales for this system. In the rotating wave approximation, the single-atom 1d Hamiltonian takes the form [151]

$$\hat{H} = \frac{\hbar^2 \hat{k}^2}{2m} + \boldsymbol{\Omega}(\hat{x}) \cdot \hat{\boldsymbol{F}} + \hat{H}_Q, \tag{6.1}$$

where $\hat{\boldsymbol{F}}$ is the total angular momentum operator and $\hat{H}_Q = -\epsilon_Q(\hbar^2 \hat{\mathbb{1}} - \hat{F}_z^2)/\hbar$ describes the quadratic Zeeman shift. The potential of this transverse magnetic lattice [90] takes the form $\boldsymbol{U}(\hat{x}) = \boldsymbol{\Omega}(\hat{x}) \cdot \hat{\boldsymbol{F}}$ from the effective magnetic field

$$\boldsymbol{\Omega}(\hat{x}) = [\Omega_{rf}\cos(\phi_{rf}) + (\Omega_1{+}\Omega_2)\cos(2k_R\hat{x}), -\Omega_{rf}\sin(\phi_{rf}) - (\Omega_1{-}\Omega_2)\cos(2k_R\hat{x}), \sqrt{2}\delta]/\sqrt{2} \tag{6.2}$$

interacting with the total atomic spin $\hat{\boldsymbol{F}}$. This Hamiltonian can be solved for the full momentum spin state basis or employ the Born-Oppenheimer approximation to solve the spatial part of the problem, including spin, for this transverse magnetic lattice. By studying this Hamiltonian in various aspects, we can examine the properties of this light-induced engineered system to see the rich physics that arises.

To solve this Hamiltonian in the basis of momentum-spin states

$$\{\cdots|k = 2lk_R, m_f = +1\rangle, |k = 2lk_R, m_f = 0\rangle, |k = 2lk_R, m_f = -1\rangle \cdots\}, \tag{6.3}$$

an easy approach is to convert the total angular momentum operator $\hat{\boldsymbol{F}}$ into F_+ and

F_-, where the F_x and F_y components take the following form:

$$F_x = \frac{1}{2}(F_+ + F_-) \quad \text{and} \quad F_y = \frac{1}{2i}(F_+ - F_-). \tag{6.4}$$

This allows the $\boldsymbol{\Omega}(\hat{x}) \cdot \hat{\boldsymbol{F}}$ term, i.e. the form of the lattice potential, in the Hamiltonian to be expressed in terms of the Ω_+ and Ω_- raising and lowering operators as found below:

$$\boldsymbol{\Omega}(\hat{x}) \cdot \hat{\boldsymbol{F}} = \frac{1}{2}\Omega_x(F_+ + F_-) + \frac{1}{2i}\Omega_y(F_+ - F_-) + \Omega_z F_z \tag{6.5}$$

$$= \left(\frac{1}{2}\Omega_x + \frac{1}{2i}\Omega_y\right)F_+ + \left(\frac{1}{2}\Omega_x - \frac{1}{2i}\Omega_y\right)F_- + \Omega_z F_z \tag{6.6}$$

$$= \underbrace{\left(\frac{\Omega_x - i\Omega_y}{2}\right)}_{\Omega_+} F_+ + \underbrace{\left(\frac{\Omega_x + i\Omega_y}{2}\right)}_{\Omega_-} F_- + \Omega_z F_z. \tag{6.7}$$

Now by rewriting Ω_+ and Ω_- in terms of Ω_x and $\pm\, i\Omega_y$ (with factors of 1/2), we obtain

$$\Omega_+ \equiv \frac{\Omega_x - i\Omega_y}{2} = \frac{1}{2}\left(\Omega_{\mathrm{rf}} e^{i\phi} + \Omega_1 e^{i2k_R x} + \Omega_2 e^{-i2k_R x}\right) \tag{6.8}$$

$$\Omega_- \equiv \frac{\Omega_x + i\Omega_y}{2} = \frac{1}{2}\left(\Omega_{\mathrm{rf}} e^{-i\phi} + \Omega_1 e^{-i2k_R x} + \Omega_2 e^{i2k_R x}\right). \tag{6.9}$$

With $\boldsymbol{\Omega}(\hat{x}) \cdot \hat{\boldsymbol{F}}$ expressed as $(\Omega_+ F_+ + \Omega_- F_- + \Omega_z F_z)$, the Hamiltonian can be written in piece-wise form as

$$H_{(N,m_F),(N',m'_F)} = \begin{cases} \frac{\hbar^2(q-2Nk_R)^2}{2m} + (\delta + \Omega_z) & \text{if } N = N',\ m_F = m'_F = +1 \quad \text{(diagonal)} \\ \frac{\hbar^2(q-2Nk_R)^2}{2m} - \epsilon_q + \Omega_z & \text{if } N = N',\ m_F = m'_F = 0 \quad \text{(diagonal)} \\ \frac{\hbar^2(q-2Nk_R)^2}{2m} - (\delta + \Omega_z) & \text{if } N = N',\ m_F = m'_F = -1 \quad \text{(diagonal)} \\ \frac{\Omega_{\mathrm{RF}}}{2} e^{-i\phi_{\mathrm{RF}}} & \text{if } N = N',\ m_F - m'_F = +1 \quad \text{(off-diagonal RF)} \\ \frac{\Omega_{\mathrm{RF}}}{2} e^{i\phi_{\mathrm{RF}}} & \text{if } N = N',\ m_F - m'_F = -1 \quad \text{(off-diagonal RF)} \\ \frac{\Omega_+}{2} & \text{if } N' = N + 1,\ \ m_F - m'_F = +1 \quad \text{(off-diagonal Raman)} \\ \frac{\Omega_-}{2} & \text{if } N' = N - 1,\ \ m_F - m'_F = -1 \quad \text{(off-diagonal Raman)} \\ 0 & \text{otherwise} \end{cases} \tag{6.10}$$

Matrix elements $H_{(N,m_F),(N',m'_F)}$ with values defined case-by-case, depend on indices, N, m_F, N', m'_F, where N denotes momentum and m_F denotes spin, and include diagonal and off-diagonal couplings for kinetic energy, Raman and RF.

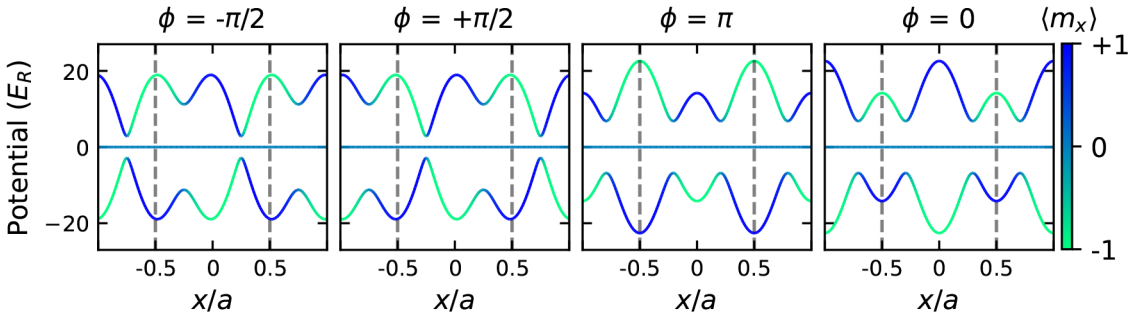

Figure 6.1: Adiabatic potentials as a function of position and including magnetization $\langle m_x \rangle$ for the values of the rf phase $= (-\pi/2, \pi/2, \pi, 0)$ with the fixed values of the coupling strengths $\hbar(\Omega_+, \Omega_-, \Omega_{rf}) = (12.7, 5.7, 4.2)E_R$, $\delta = 0$ and $\epsilon = 0.04E_R$.

6.1.1 Corresponding Adiabatic Potential

The adiabatic potentials derived from the Raman–rf magnetic Hamiltonian of Eq. 6.1 form a state-dependent, bipartite magnetic lattice, as seen from Eq. 6.5. The three adiabatic potential states, corresponding to the dressed spin states, are shown in Fig. 6.1 as a function of position, along with their respective spin projection $\langle m_x \rangle$. The ground-state adiabatic potentials exhibit spatially alternating minima whose spin composition is determined by the local effective magnetic field. These spin-textured potential landscapes are a key feature enabling the experimental realization of magnetic lattices [152]. Their bipartite nature arises from the interplay of the Raman and rf couplings, which modify both the depth and phase of the spin-dependent potential minima.

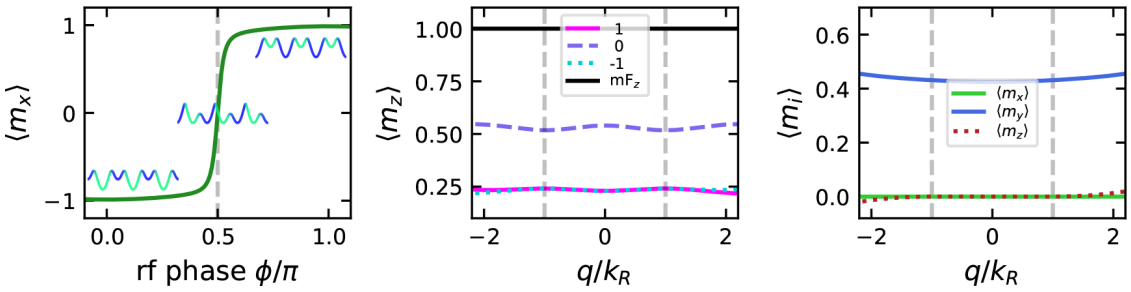

Figure 6.2: Magnetizations. (a) $\langle m_x \rangle$ as a function of the rf phase ϕ. (b) Ground state populations of $\langle m_z \rangle$ and (c) ground state magnetizations, as functions of quasi-momentum q/k_R.

6.1.2 Magnetizations

In the full momentum–spin basis, the magnetization components of a given eigenstate $|\Psi\rangle$ are defined as

$$\langle m_i \rangle = \langle \Psi | F_i | \Psi \rangle, \quad i \in \{x, y, z\}. \tag{6.11}$$

These expectation values provide a direct measure of the spin orientation in each eigenstate and offer insight into how the atomic spin texture evolves across the lattice. Figure 6.2 illustrates several key magnetization properties.

(a) $\langle m_x \rangle$ as a function of the rf phase ϕ_{RF}, with insets showing the corresponding ground state adiabatic potential configurations. The variation of $\langle m_x \rangle$ reflects how the rf phase controls the relative positioning of the spin-dependent lattice sites.

(b) $\langle m_z \rangle$ as a function of quasimomentum, including the individual spin populations and their sum. This reveals how the longitudinal spin polarization

changes across the Brillouin zone.

(c) The ground-state spin populations versus quasimomentum, highlighting the momentum-dependent redistribution of population among the $m_F = \pm 1, 0$ states.

Taken together, these magnetization plots provide a microscopic picture of the spin texture and its tunability through experimental parameters such as the rf phase and Raman coupling strengths. This information is essential for understanding the interplay between spin, momentum, and topology in the bipartite magnetic lattice.

6.2 Experimental Characterization

The experiment utilized BECs of ^{87}Rb atoms confined in a crossed optical dipole trap. Two independent 1064 nm laser beams with 150 μm waists intersected orthogonally along $\hat{e}_x$ and $\hat{e}_y$, forming a harmonic potential with trapping frequencies $(\omega_x, \omega_y, \omega_z)/2\pi \approx (15, 150, 100)$ Hz. Small condensates containing 5–10 $\times 10^3$ atoms were prepared to minimize density-dependent losses and secondary scattering processes [133].

After forced evaporative cooling, the atomic cloud was subjected to a short radio-frequency (rf) pulse and a second evaporation sequence in the presence of magnetic field gradients, yielding condensates in the magnetically insensitive $|f = 1, m_F = 0\rangle$ state. A uniform bias field of $B_0 \approx 0.1$ mT established the quantization axis and produced a Zeeman splitting of $\omega_Z/2\pi \approx 1$ MHz between adjacent m_F sublevels.

The spin-momentum lattice was realized by coupling these states with an rf field

of frequency ω_{rf} and a pair of counterpropagating Raman beams along $\hat{e}_x$. Each Raman beam contained two frequency components, ω_0 and $\omega_0 + \omega_{\mathrm{rf}}$, defining a controllable relative phase ϕ_{rf} between the Raman beat tone and the rf field. The Raman wavelength $\lambda_R = 790.03(2)$ nm was selected to cancel the scalar light shift, defining the single-photon recoil momentum $\hbar k_R = 2\pi\hbar/\lambda_R$ and recoil energy $E_R = \hbar^2 k_R^2/2m$.

Calibrations of the Raman-rf lattice were performed by pulsing the rf and two-tone Raman fields to determine the three coupling strengths $\hbar(\Omega_1, \Omega_2, \Omega_{\mathrm{rf}})$ in units of E_R, while keeping the detuning δ near zero using field stabilization and post-selection. Control over ϕ_{rf} was verified by observing pulsed evolution under the combined rf/Raman lattice and fitting the phase-dependent dynamics, including modulation between 0 and π.

The lowest-energy adiabatic potential forms a spin-dependent bipartite lattice [90] as discussed in Section 6.1.1, where the two sublattice sites, labeled $|\uparrow\rangle$ and $|\downarrow\rangle$, correspond to atomic states nearly fully polarized along $\hat{F}_x$, i.e., $|m_x = \pm 1\rangle$. The relative energy of these sites is controlled by the rf phase ϕ_{rf}: choosing $\phi_{\mathrm{rf}} = \mp\pi/2$ selects the lattice configurations C-I and C-II, while other values introduce a tunable energy offset Δ that can be exploited for state preparation and readout.

BECs were adiabatically loaded into the bipartite lattice by ramping the coupling fields and detuning over 2.5 ms, with $\phi_{\mathrm{rf}} = 0$ or π chosen to populate either $|\uparrow\rangle$ or $|\downarrow\rangle$. The lattice configuration was set by abruptly changing ϕ_{rf} to $\mp\pi/2$, producing a $q = 0$ pseudospin-polarized state that is an equal superposition of the two lowest bands. After this initialization, atoms underwent resonant tunneling between the

strongly coupled pseudospin sites [153, 154].

Following lattice loading and evolution, the spin-resolved momentum distribution was measured by turning off the Raman and rf fields and applying a $\pi/2$ pulse around $\hat{F}_y$, which rotates $\hat{F}_x$ eigenstates into the $\hat{F}_z$ measurement basis. The BEC was then released for 12 ms time-of-flight in the presence of a magnetic field gradient along $\hat{e}_y$, separating the m_F sublevels. Resonant absorption imaging of these clouds allowed the determination of populations on the $|\uparrow\rangle$ and $|\downarrow\rangle$ sublattice sites.

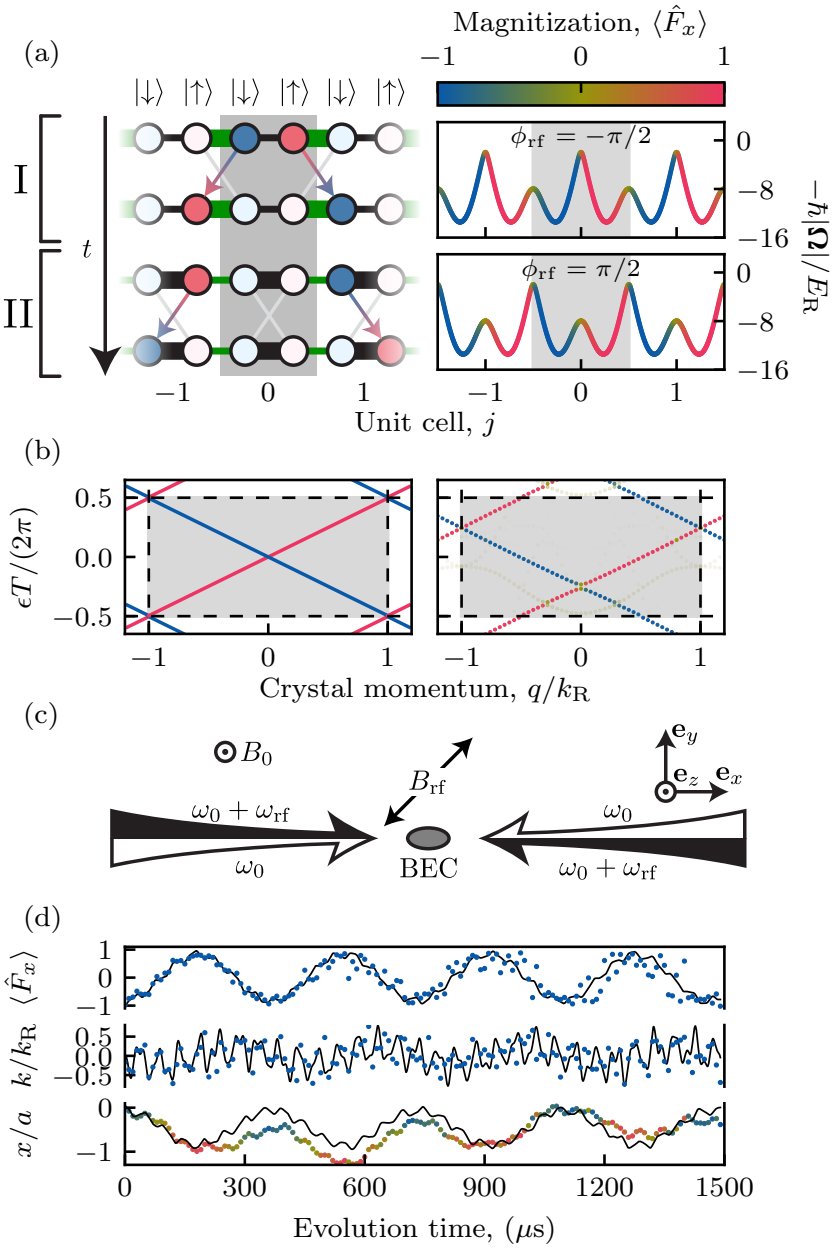

Figure 6.3: Experimental schematic and lattice characterization. (a) Switching protocol showing unit cell $j = 0$ in gray. Bold green links indicate intercell tunneling in configuration C-I; bold black links show intracell tunneling in C-II. Right panel: adiabatic lattice potentials colored by $\langle \hat{F}_x \rangle$. (b) Floquet band structure sampled stroboscopically, colored according to $\langle \hat{F}_x \rangle$. The lowest Brillouin zone (BZ) and quasienergy zone are marked in gray. Left: idealized SSH model. Right: numerical lattice model. (c) Illustration of field geometry: 2-tone counterpropagating Raman lasers and rf magnetic field. (d) Static lattice tunneling dynamics for atoms prepared in $|\downarrow\rangle$: top, magnetization $\langle \hat{F}_x \rangle$; middle, group velocity; bottom, integrated displacement colored according to $\langle \hat{F}_x \rangle$ as in (a). Black curves: numerical simulations.

6.3 Dirac Floquet

The 1d bipartite lattice described above can be mapped onto a 1d Su-Schrieffer–Heeger (SSH) model [149]:

$$\hat{H} = -\sum_{j} \Big[J\big(|j+1,\downarrow\rangle \langle j,\uparrow| + \text{h.c.} \big) + \text{J}'\big(|\text{j},\downarrow\rangle \langle \text{j},\uparrow| + \text{h.c.} \big) \Big], \tag{6.12}$$

where j indexes unit cells, $|\uparrow\rangle$ and $|\downarrow\rangle$ label pseudospin sites, with J the intercell tunneling amplitude (connecting adjacent unit cells) and J' the intracell tunneling amplitude (within a unit cell) [90].

We implement a Floquet "switching" protocol [155], alternating between configurations C-I ($J' \approx 0$, $J = J_0$) and C-II, with period T. During the first half-period, intercell tunneling occurs, while the second half allows intracell tunneling. When $J_0 T = \pi$, each half-period acts as a π-pulse, exchanging amplitudes between sites. Over one full period, atoms are displaced by one lattice constant a, leading to stroboscopic spin-momentum-locked motion described by the Floquet Dirac Hamiltonian

$$\hat{H}^{\text{F}}(q) = qv\hat{\sigma}_z,$$

representing massless, gapless relativistic particles.

Figure 6.3(d) shows static lattice tunneling dynamics: magnetization oscillates with a period of 366(3) μs, with negligible population in $|m_x = 0\rangle$, allowing the mapping $|\uparrow,\downarrow\rangle \rightarrow |m_x = \pm 1\rangle$. Integration of group velocity yields displacement consistent

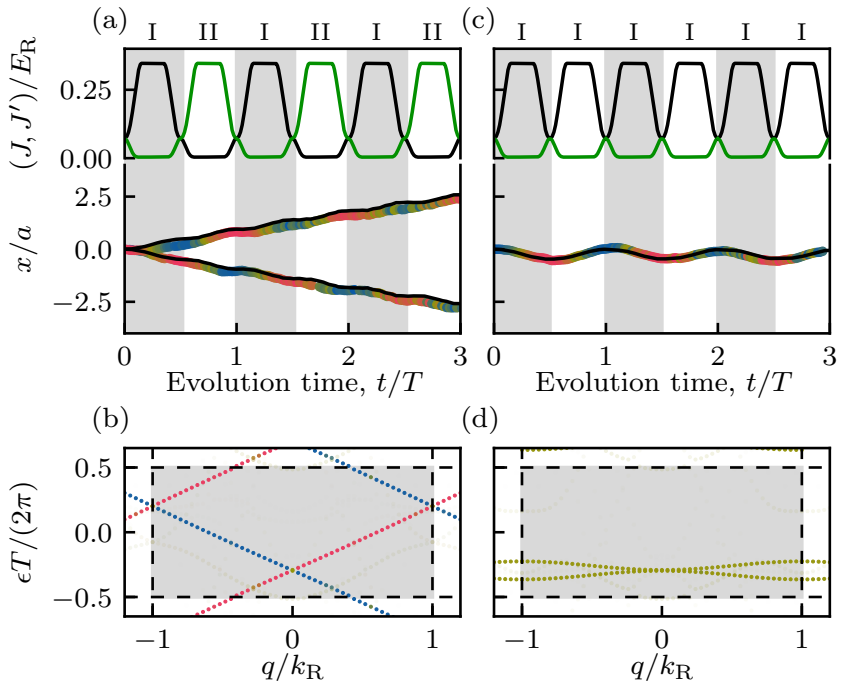

Figure 6.4: Floquet modulation protocols. (a,b) Configuration-switching protocol: (a) calculated intercell (black) and intracell (green) tunneling amplitudes with displacement (colored by $\langle \hat{F}_x \rangle$). Gray/white bands indicate C-I/C-II. (b) Floquet quasienergy bands colored by $\langle \hat{F}_x \rangle$. (c,d) Single-configuration protocol: (c) tunneling amplitudes and displacement; (d) corresponding Floquet band structure showing quadratic touching points. Black/green curves: intercell/intracell tunneling.

with tunneling between adjacent sites ≈ 200 nm apart.

By switching ϕ_{rf} every half-tunneling period while smoothly ramping Ω_{rf} to avoid excitation of higher bands, we realized a drive period $T = 448$ μs. Minor deviations from the SSH model, or rather the ideal π phase shift and tunneling periods were corrected empirically.

The observed displacement and magnetization show near-linear evolution over many Floquet periods, demonstrating spin-momentum-locked transport with drift velocities $\pm 0.89(4)$ a/T and $\pm 0.86(2)$ a/T, consistent with numerical simulations. A single-configuration protocol with constant ϕ_{rf} yields oscillatory displacement con-

fined to a single double well, highlighting the importance of the switching protocol.

6.4 Conclusions and Outlook

We implemented a Floquet "switching" protocol in a 1D bipartite magnetic lattice, realizing a driven SSH model that maps onto a massless Dirac Hamiltonian. By alternating between two lattice configurations with near-optimal timing, we observed spin-momentum-locked transport, with well defined drift velocities and sustained displacement over multiple Floquet periods. Measured magnetization, group velocity, and atomic displacement agree closely with numerical simulations, with small deviations attributed to finite ramp times, residual tunneling during switching, and weak additional lattice potentials.

This work establishes a flexible platform for engineering and probing topological band structures in periodically driven systems. The precise control over tunneling amplitudes and phases allows exploration of generalized Floquet Hamiltonians, including massive Dirac and Rice–Mele-type systems. Our experimental results, including topological invariants measured via micromotion and drift velocity [37], demonstrate that Floquet engineering can realize exotic band structures beyond static systems.

Chapter 7: Induction of Artificial Gauge Fields

The dynamics of charged quantum particles in magnetic fields encompass a diverse array of intriguing phenomena. For more than a decade, experimental advances have enabled the realization of effective magnetic field dynamics with charge-neutral atoms by engineering Hamiltonians that mimic those of charged particles in real magnetic fields [156, 157]. Numerous approaches have been implemented, from exploiting the correspondence between the Lorentz and Coriolis forces in rotating frames [158–162] to generating synthetic magnetic fields via position-dependent optical couplings [95, 163]. These light-induced gauge fields give rise to an effective magnetic flux directly connected to the Aharonov–Bohm phase [164] acquired by charged particles encircling magnetic-field regions. Many successful experiments have since demonstrated that ultracold atoms constitute a remarkably versatile platform for realizing magnetic-field effects and engineering artificial gauge fields for intricate analog systems [71, 91, 165–169]. Prior to the work presented in this chapter and in chapter 8, previous techniques produced only uniform and slowly varying synthetic fields—tuned via magnetic-field gradients—which are inherently unsuitable for generating disorder. Realizing disordered gauge fields in ultracold-atom systems therefore requires a fundamentally different approach. Here, we implement such an approach by synthesizing position-dependent optical fields—intensity patterns—using a DMD (see Section 3.8). This method enables tunable vector po-

tentials and light-intensity gradients, effectively creating spatially varying detunings that drive the vortex-nucleation transition in BECs. We show that this approach successfully reproduces familiar effects—New dog, old tricks. In chapter 8, we extend the technique to generate controlled disorder for exploring both equilibrium and out-of-equilibrium regimes in the context of localization phenomena.

7.1 Effective Single-Particle Hamiltonian with Artificial Gauge Field

By engineering a Hamiltonian that incorporates an effective vector gauge potential—analogous to that of a charged particle—it is possible to create synthetic electric and magnetic fields. This artificial vector potential is realized by optically dressing a BEC with a pair of Raman beams, yielding a tunable dispersion relation of the form $(\mathbf{p}_{\text{can}} - \mathcal{A})^2/2m^*$, where $q\boldsymbol{A} \Rightarrow \mathcal{A}$, $\mathcal{A} = (\mathcal{A}_x, \mathcal{A}_y, \mathcal{A}_z)$ and serves as the synthetic gauge field, and m^* denotes an effective mass.

Our system consists of ^{87}Rb BECs in the $F = 1$ ground-state, prepared in an optical dipole trap. A uniform magnetic field, $B_0\mathbf{e}_z$, is applied to break the degeneracy of the hyperfine magnetic sublevels $|m_F = 0, \pm 1\rangle$. The energy splittings between these levels are described by the linear and quadratic Zeeman shifts, which are expressed as:

$$\hbar\omega_Z = g_F\mu_B B_0 \approx \pm E_{\pm 1}, \qquad \hbar|\epsilon| = E_0 - \frac{E_{-1} + E_{+1}}{2}, \tag{7.1}$$

where $g_F\mu_B = 0.7$ MHz/G for ^{87}Rb in $F = 1$, $E_{-1} = \hbar\omega_z$, $E_0 = \hbar\epsilon$, $E_{+1} = -\hbar\omega_z$, and $|E_{-1}| \approx |E_{+1}| \gg |E_0|$. A pair of Raman lasers with wavelength λ couple the m_F states with Rabi frequency Ω_R. The lasers differ in frequency by $\Delta\omega_R \approx \omega_Z$,

and the detuning from Raman resonance is defined as $\delta = \omega_R - \omega_Z$. The quadratic Zeeman shift is taken as negative, i.e., $-\hbar\epsilon$. When expressed as a frequency in kHz, its amplitude for ^{87}Rb in the $F = 1$ manifold is given by $\epsilon/h = \epsilon_B B^2$.

A Raman transition involves two or more light fields with different frequencies that couple internal atomic states while imparting momentum to the atom. This process is effectively a two-photon transition mediated by a virtual excited state. When Raman lasers intersect at an angle, the effective recoil momentum from a single-photon absorption is given by $\hbar k_R = 2\pi\hbar/(\lambda \sin(\theta/2))$, which defines the natural momentum scale. The corresponding recoil energy for an atom of mass m is $E_R = \hbar^2 k_R^2/(2m)$, setting the system's natural energy scale. These quantities, k_R and E_R, are fundamental for describing the momentum and energy dispersion of Raman-dressed systems.

The origin of the Raman coupling Hamiltonian relies on the vector light-shift experienced by the atoms from the Raman beams. If we consider the counter propagating case, the electric field from each Raman field is given by:

$$\mathbf{E}_1 = E_0 e^{i(k_R x - \omega_R t)}\, \mathbf{e}_x, \quad \text{and} \quad \mathbf{E}_2 = E_0 e^{-i(k_R x + \omega_R t + \Delta\omega_R t)}\, \mathbf{e}_y, \tag{7.2}$$

where we have assumed equal amplitudes for both fields: $E_1 = E_2 = E_0$. Note that the fields must have distinct polarizations in order to drive Raman transitions between internal states. The total electric field at the atoms is then

$$\mathbf{E}(x,t) = E_0 \left\{ e^{i(k_R x - \omega_R t)}\, \mathbf{e}_x + e^{-i(k_R x + \omega_R t + \Delta\omega_R t)}\, \mathbf{e}_y \right\}. \tag{7.3}$$

The vector light shift, is proportional to the cross product $\mathbf{E}^* \times \mathbf{E}$, and can be written as

$$\mathbf{E}^* \times \mathbf{E} = (\mathbf{E}_1^* + \mathbf{E}_2^*) \times (\mathbf{E}_1 + \mathbf{E}_2) \tag{7.4}$$

$$= \mathbf{E}_1^* \times \mathbf{E}_2 + \mathbf{E}_2^* \times \mathbf{E}_1, \tag{7.5}$$

where the cross terms remain since $\mathbf{E}_1^* \times \mathbf{E}_1 = \mathbf{E}_2^* \times \mathbf{E}_2 = 0$. Evaluating the remaining terms:

$$\mathbf{E}^* \times \mathbf{E} = \left(E_0^2 e^{-i(2k_R x + \Delta\omega_R t)} - E_0^2 e^{i(2k_R x + \Delta\omega_R t)}\right) \mathbf{e}_z. \tag{7.6}$$

Thus, the vector light shift produces an effective Zeeman magnetic field along $\mathbf{e}_z$:

$$\mathbf{B}_{\text{eff}} \propto -2iE_0^2 \sin(2k_R x + \Delta\omega_R t)\, \mathbf{e}_z. \tag{7.7}$$

This effective magnetic field couples to the atomic spin through the interaction with the effective magnetic moment $\boldsymbol{\mu} = g_F m_F \hat{\mathbf{F}}$, where $\hat{\mathbf{F}}$ is the angular momentum operator for the $F = 1$ manifold. The resulting interaction Hamiltonian is

$$\hat{H}_{int} = -\boldsymbol{\mu} \cdot \mathbf{B}_{\text{eff}}. \tag{7.8}$$

In a frame rotating at frequency $\Delta\omega_R$, and under the rotating wave approximation (RWA), the Raman coupling Hamiltonian in the bare spin basis $\{|-1\rangle, |0\rangle, |+1\rangle\}$

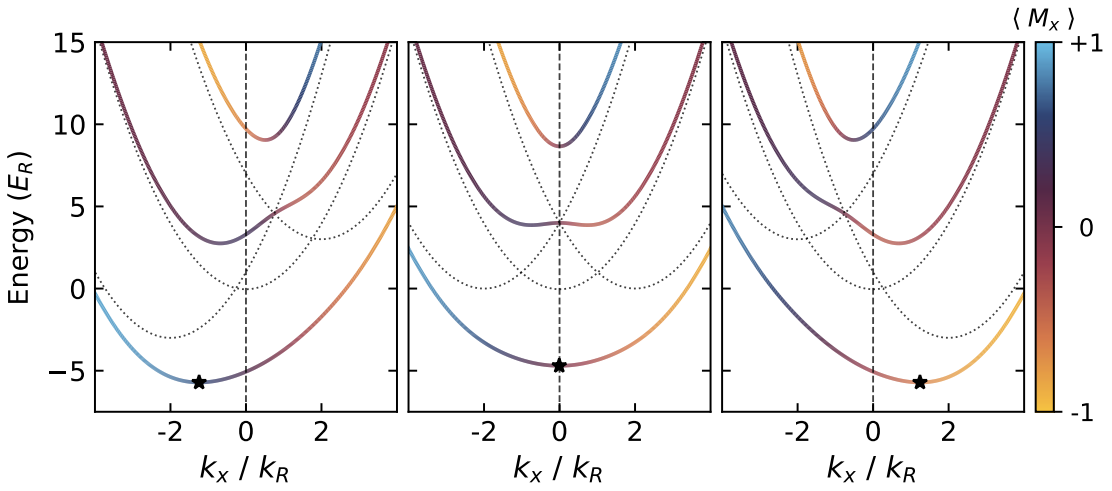

Figure 7.1: Eigenenergies of the Raman dressed states as a function of quasimomentum k_x, with the colorbar indicating the respective spin compositions. The dotted curves correspond to free-particle dispersion relations of the bare spin-momentum states. The solid curves represent the eigenenergies of $\hat{H}_x$ at $\Omega_R = 9E_R$, $\epsilon = 0.044\ E_R$ and for detuning δ values of $[-3, 0, 3]\ E_R$; stars indicate the location of the minimum of the dispersion relation $k_{min} = \mathcal{A}/\hbar$, where $\mathcal{A}$ is the vector potential.

is

$$\hat{H}_R/\hbar = \begin{bmatrix} 0 & \frac{\Omega_R}{2}e^{i2k_Rx} & 0 \\ \frac{\Omega_R}{2}e^{-i2k_Rx} & 0 & \frac{\Omega_R}{2}e^{i2k_Rx} \\ 0 & \frac{\Omega_R}{2}e^{-i2k_Rx} & 0 \end{bmatrix}, \tag{7.9}$$

where Ω_R is the two-photon Rabi frequency characterizing the strength of the Raman coupling, and the detuning from Raman resonance is $\delta = \Delta\omega_R - \omega_Z$.

The Hamiltonian of the system can be written in the form

$$\hat{H} = \left[\frac{\hbar^2(k_y^2 + k_z^2)}{2m} + V(\mathbf{r})\right] \otimes \hat{1} + \hat{H}_x, \tag{7.10}$$

where $\hat{H}_x$ is a 3×3 matrix that includes the kinetic energy associated with the x-component of the momentum, $k_x = \mathbf{k} \cdot \mathbf{e}_x$, the interaction with the Raman field,

and the Zeeman energy shifts.

Raman Coupling Hamiltonian in Momentum Space. The set of spin-momentum states $\{|-1,\, k_x - 2k_R\rangle,\ |0,\, k_x\rangle,\ |+1,\, k_x + 2k_R\rangle\}$,[1] where k_x is the quasimomentum, defines the basis in which the $\hat{H}_x$ component of the full Hamiltonian 7.10 is expressed. It includes both the kinetic energy along the coupling direction and the spin-dependent light shifts induced by the Raman fields. The Raman process couples states differing in spin by $\Delta m_F = \pm 1$ and momentum by $\pm 2\hbar k_R$. In this basis, $\hat{H}_x$ takes the form:

$$\hat{H}_x = \begin{bmatrix} \hbar^2(k_x - 2k_R)^2/2m - \hbar\delta & \hbar\Omega_{\mathrm{R}}/2 & 0 \\ \hbar\Omega_{\mathrm{R}}/2 & \hbar^2 k_x^2/2m - \hbar\epsilon & \hbar\Omega_{\mathrm{R}}/2 \\ 0 & \hbar\Omega_{\mathrm{R}}/2 & \hbar^2(k_x + 2k_R)^2/2m + \hbar\delta \end{bmatrix}. \tag{7.11}$$

This is referred to as the Raman coupling Hamiltonian, as it captures all the essential physics relevant to our experiments. Notice how $\hat{H}_x$ (7.11) bears resemblance to the Hamiltonian encountered in a periodic potential, as discussed in Chapter 4. A distinctive feature is that it yields only three energy bands, along with two additional tunable parameters—the Zeeman shifts δ and ϵ.

Energy-Momentum Dispersion Relation. In the absence of Raman coupling, the Hamiltonian is diagonal, and the energy of each spin-momentum state, is simply given by its corresponding diagonal entry. These states follow the free-particle dis-

[1] This basis represents the spin-momentum eigenstates realized in the laboratory. It reflects the physical recoil imparted by the Raman process—i.e., an atom that absorbs a photon from beam 2 and emits into beam 1 and the recoil direction. This form also reflects the group velocity of the data to follow in the next Sections and Chapter 8.

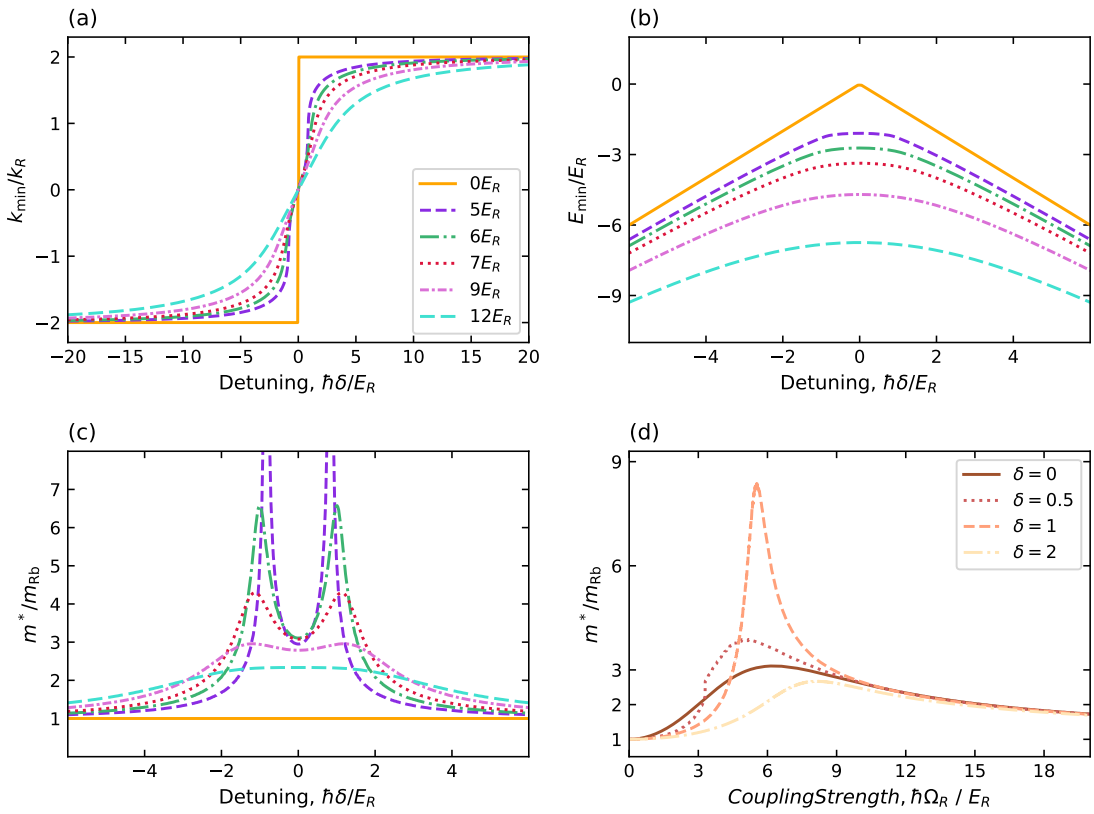

Figure 7.2: Properties of the lowest Raman-dressed energy band as functions of detuning δ and Raman coupling strength Ω_{R}. (a)-(c) Quasimomentum of the energy minimum $k_{\min}/k_{\mathrm{R}}$, Minimum energy $E_{\min}/E_{\mathrm{R}}$, and Effective mass m^*/m_{Rb}, all as functions of detuning δ for various coupling strenths; (d) Effective mass m^*/m_{Rb} as a function of Ω_{R} at fixed detunings. These features reflect how Raman coupling and detuning reshape the band structure and influence atomic dynamics.

persion, as illustrated by the gray dotted parabolas in Fig. 7.1. When Raman coupling is introduced, the previously degenerate crossings between these parabolas open into avoided crossings, forming energy gaps in the spectrum. This results in new, hybridized energy bands shown in Fig. 7.1, as colored curves corresponding to spin composition. These band structures are obtained by numerically diagonalizing $\hat{H}_x$ as a function of quasimomentum k_x. In the regime of strong Raman coupling $\hbar\Omega_{\mathrm{R}} \gg 4E_{\mathrm{R}}$, this dressed dispersion takes a nearly free-particle form centered at a

shifted quasimomentum minimum:

$$E(k_x) \approx \frac{(\hbar k_x - \mathcal{A})^2}{2m^*}, \quad \text{where} \quad \mathcal{A} = \hbar k_{\min}$$

and corresponds to an light-induced vector potential, where m^* is an effective mass reflecting the modified curvature of the band relative to that of the bare states.

Figure 7.2 illustrates key features of the lowest energy Raman-dressed band as functions of detuning $\hbar\delta$ and coupling strength $\hbar\Omega_{\mathrm{R}}$. (a) Shows the quasimomentum $k_{\min}/k_{\mathrm{R}}$ at which the energy minimum occurs, plotted versus detuning for several Raman coupling strengths. As Ω_{R} increases, the transition from $k_{\min} \approx -2k_{\mathrm{R}}$ to $+2k_{\mathrm{R}}$ becomes smoother, indicating direct signature of dressed states. In contrast, for $\Omega_{\mathrm{R}} = 0$, the transition is abrupt, reflecting the bare-state crossing. (b) Displays the minimum energy $E_{\min}/E_{\mathrm{R}}$ as a function of detuning. This reflects the overall shift of the dressed dispersion and is important for understanding adiabatic loading and energy scales of the system. (c) Shows the effective mass m^*/m_{Rb} which is found from the curvature of the lowest band at $k_{\min}$. Near $\delta = 0$, the band becomes very flat, causing the effective mass to increase significantly. As the Raman coupling strength Ω_{R} increases, the peak in the effective mass becomes smoother and less pronounced. This reflects the widening of the avoided crossing and a reduced sensitivity of the band curvature to detuning. Lastly, (d) shows the effective mass m^*/m_{Rb} as a function of Raman coupling strength $\hbar\Omega_{\mathrm{R}}$ for several fixed detunings: $[-2, -0.5, 0, 1]$ E_{R}. The curves are symmetric with respect to detuning—i.e., the behavior at $+\delta$ mirrors that at $-\delta$—so the trends for ± 0.5 E_{R}, ± 1 E_{R}, etc., are

identical. For each detuning, the effective mass peaks at an intermediate coupling strength and then decreases as the band broadens. In particular, sharp features at $\pm 1\ E_{\mathrm{R}}$ become much smoother by $\pm 2\ E_{\mathrm{R}}$, indicating that the peak in effective mass is quickly reduced as the coupling strength increases. All together, these plots highlight how the parameters δ and Ω_{R} tune the shape and energy of the dressed band, and how they play critical roles with effective dynamics. This is especially important as we explore disordered Raman-dressed systems in later sections and in the next Chapter.

7.2 New Dog, Old Tricks: DMD Generated Optical Fields

In this section, we demonstrate the realization of position-dependent optical fields, i.e. intensity patterns, generated from a DMD in our Raman-dressed system. Figure 7.3 illustrates the necessary ingredients for implementing light-induced gauge fields in our lab. Here, we show a "new dog", the DMD, and how it performs "old tricks", i.e. confirms previous results. Indeed we can create uniform vector potentials and in addition we observe the vortex-nucleation transition in a BEC from a synthetic magnetic field generated by our new dog.

7.2.1 Experimental Characterization

All artificial gauge field experiments described in this chapter, and the next, share the same experimental setup. The direction, wavelength, and polarization of the Raman lasers; the direction and amplitude of the bias magnetic fields; the geometry

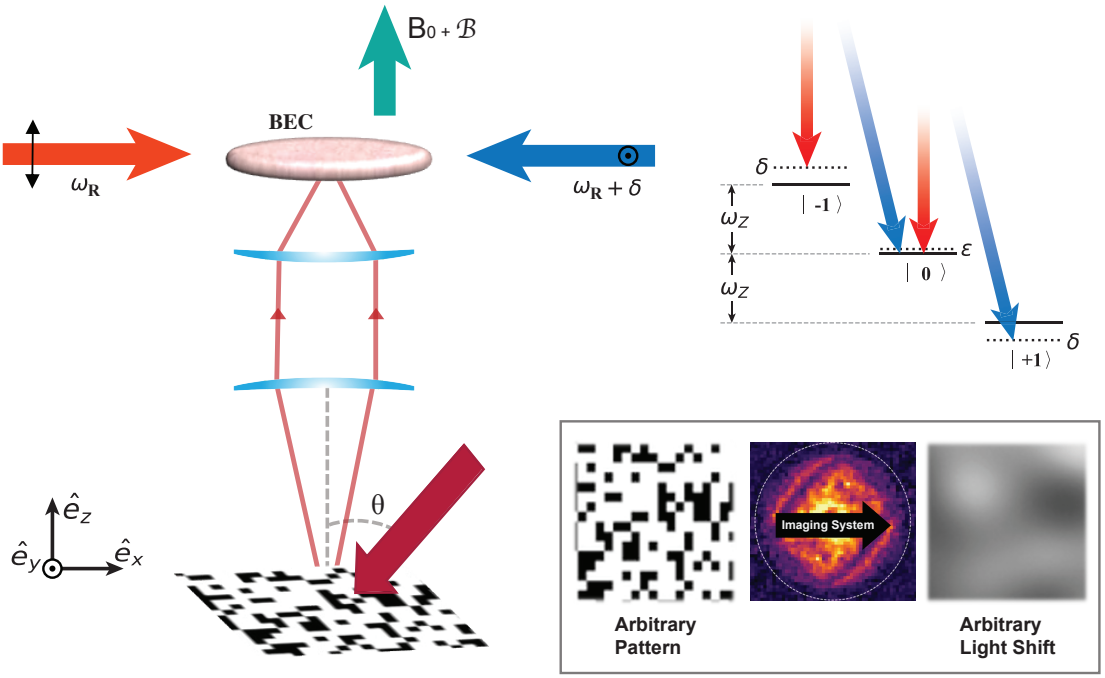

Figure 7.3: Standard experimental setup and level diagram for implementing light-induced artificial gauge fields with BECs. A uniform bias magnetic field $B_0\hat{e}_z$ Zeeman-splits the energy levels in the $F = 1$ manifold of ^{87}Rb, while a pair of counter-propagating Raman beams couple spin states of a BEC initially prepared in the $m_F = 0$ state. Additionally, a DMD beam projects a spatially varying light pattern that creates a position-dependent detuning, corresponding to an effective field $\mathcal{B}\hat{e}_z$, at the location of the atoms. Note: The arbitrary pattern generated by the DMD propagates through both the DMD optical path and the imaging system before reaching the atoms.

of the dipole trap; and specifications of the DMD system are summarized in Fig. 7.3.

Our experiments begin with BECs of ^{87}Rb atoms prepared in the $|F = 1, m_F = 0\rangle$ state, confined in a crossed optical dipole trap with trapping frequencies $2\pi \times (32, 97, 140)$Hz. A uniform bias magnetic field $B_0\hat{e}_z$ defines the quantization axis and introduces a Zeeman splitting between spin states of $\hbar\omega_z$. Raman coupling is implemented using a pair of counter-propagating laser beams along the $\hat{e}_x$ direction, with frequency difference $\Delta\omega_R$. These beams are ramped on from zero to a final

Rabi coupling strength Ω_R over 20–100 ms. Adiabatic loading into the lowest-energy Raman-dressed state with quasimomentum $k_x = 0$ is ensured by choosing a ramp time long compared to the effective trap period along $\hat{e}_x$, the Raman beam direction. The Raman beams couple the internal spin states with Rabi frequency Ω_R, modifying the dispersion relation. A DMD beam with waist ≈ 100 um, along with a simultaneous compensation detuning gradient-to compensate the vector light shift, is then ramped on from zero to a final control power $P = 160$ mW over 40 ms, ensuring adiabaticity. Additionally, this DMD beam projects a spatially varying light pattern that creates a position-dependent detuning at the location of the atoms, where the pattern changes depending on the appropriate experiment. The arbitrary pattern generated by the DMD propagates through both the DMD optical path and the imaging system before reaching the atoms. The resonance condition for Raman coupling is determined through pulsed time-evolution experiments under the Raman Hamiltonian, where the position-dependent detuning is present, along with a compensation detuning.

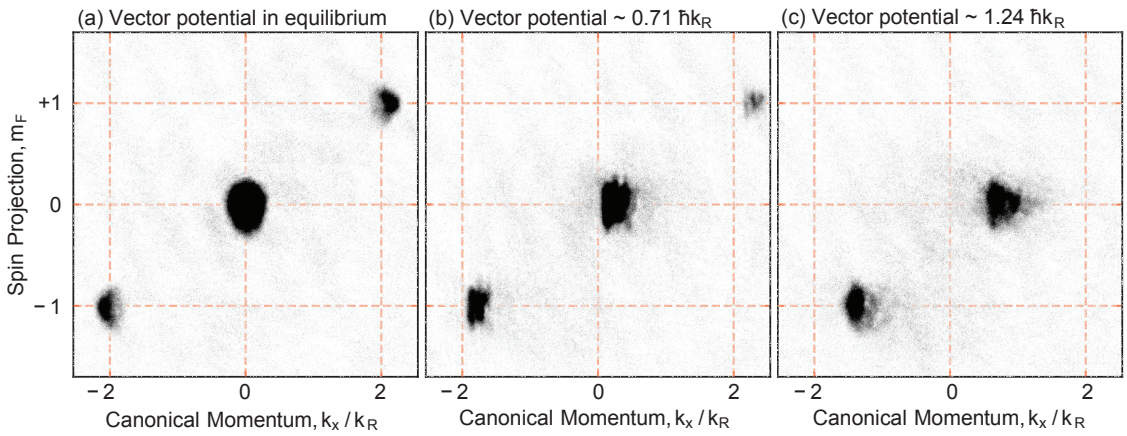

Figure 7.4: Detection of Raman dressed states after TOF, where the experimental parameters are $\hbar\Omega_{\mathrm{R}} = 9\ E_{\mathrm{R}}$ and $\hbar\epsilon = 0.44\ E_{\mathrm{R}}$. (a) A Raman dressed state in equilibrium, where the detuning $\delta = 0\ E_{\mathrm{R}}$ and the corresponding vector potential $\mathcal{A} = 0\ \hbar k_{\mathrm{R}}$. (b) Raman dressed state with $\delta = 1.5\ E_{\mathrm{R}}$ and the corresponding vector potential $\mathcal{A} \approx 0.71\ \hbar k_{\mathrm{R}}$. Here the mechanical momentum $\langle \hat{p}_x \rangle \approx 0.865\ \hbar k_{\mathrm{R}}$. (c) Another Raman dressed state with $\delta > 3\ E_{\mathrm{R}}$ and the corresponding vector potential $\mathcal{A} \approx 1.24\ \hbar k_{\mathrm{R}}$. Here the mechanical momentum $\langle \hat{p}_x \rangle \approx -0.32\ \hbar k_{\mathrm{R}}$.

7.2.2 Uniform Vector Potential

This section demonstrates the implementation of spatially uniform artificial vector potentials in the large Raman coupling regime, where $\hbar|\Omega_R| \gg 4E_R$. Figure 7.1 illustrates the most prominent effect of a uniform light-induced artificial vector potential $\mathcal{A}$: a shift in the energy-momentum dispersion relation $E(k)$. This light-induced vector potential forms the basis of our experiments with artificial gauge fields and can be directly measured from absorption images of atomic distributions, as shown in Fig. 7.4a where the vector potential is in equilibrium and its mechanical momentum $\langle \hat{p}_x \rangle = 0$. Examples of non-zero vector potentials are shown in Fig. 7.4b–c, corresponding to detunings of $\delta = 1.5\, E_{\mathrm{R}}$ and $\delta > 3\, E_{\mathrm{R}}$, with associated mechanical momenta of $\langle \hat{p}_x \rangle \approx 0.865\, \hbar k_{\mathrm{R}}$ and $\approx 1.24\, \hbar k_{\mathrm{R}}$, respectively, reflecting the average

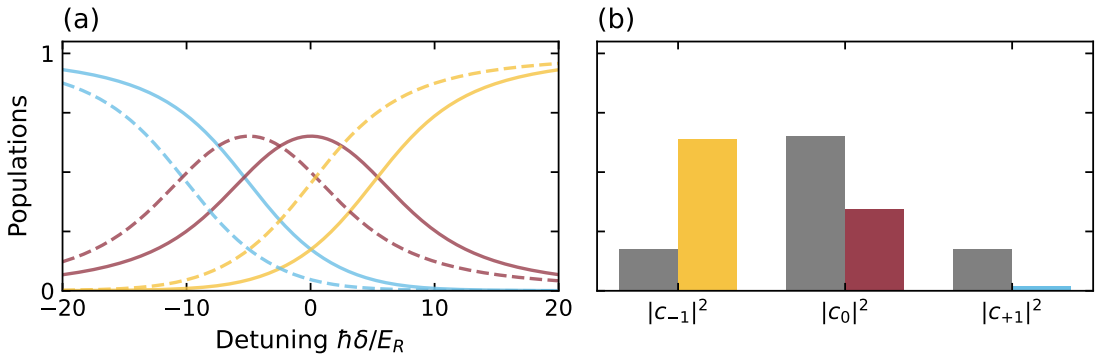

Figure 7.5: Frational populations of the lowest dressed state. (a) Spin-momentum composition at $\hbar\Omega_{\mathrm{R}} = 9\ E_{\mathrm{R}}$ and $\hbar\epsilon = 0.44\ E_{\mathrm{R}}$, is shown as a function of detuning δ. Where the solid curves denote $\delta = 0$, and the dashed curves denote $\delta = 1.5\ E_{\mathrm{R}}$. (b) Weighted probabilities, $|c_{m_F}|^2$, reflecting the spin composition of the dressed state. Here, the solid bars show fractional populations for $\delta = 0$ and the color bars show fractional populations for $\delta = 1.5\ E_{\mathrm{R}}$. Note: The spin-momentum composition here with $\delta = 1.5\ E_{\mathrm{R}}$, corresponds to the TOF image in Fig. 7.4b.

atomic motion in the dressed states.

7.2.3 Vortex-Nucleation Transition in BECs

This section focuses on spatially varying artificial gauge fields via the generation of synthetic magnetic field gradients using our new dog, i.e. our DMD system, Section 3.8. By controlling the light intensity profile via the DMD, we create spatially varying light shifts—equivalent to detuning gradients—and observe the vortex-nucleation transition in a BEC. This confirms previous results obtained with coil-generated gradients and highlights the capability of our DMD-based approach to produce synthetic magnetic field gradients and other intensity patterns.

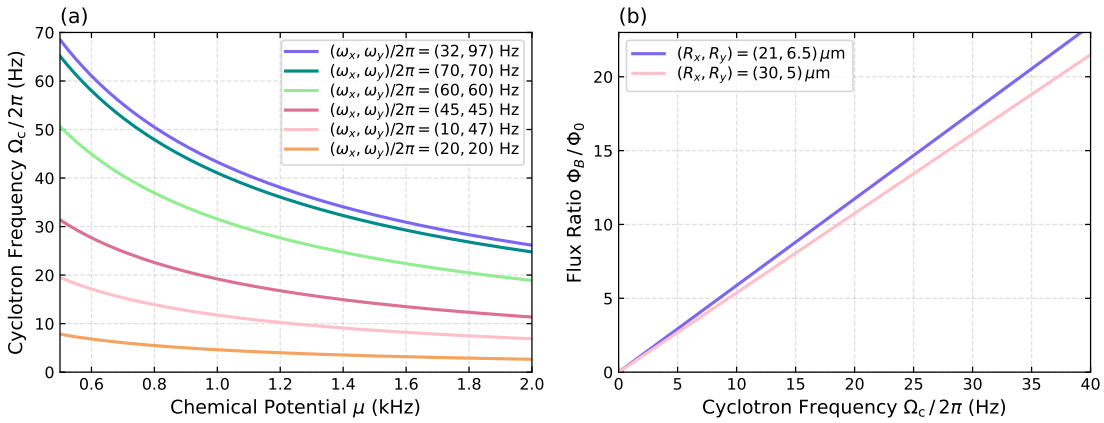

Figure 7.6: Trap geometry comparison. (a) Critical cyclotron frequency Ω_c, emphasizing the dependence on the chemical potential μ and the trap geometry, where $m^* = m$ is used to isolate the effect of trap geometry for comparison. The violet or top curve reflects trap geometry for artificial gauge field experiments. (b) Flux ratio Φ_B/Φ_0 as a function of critical cyclotron frequency Ω_c, for two BEC sizes, where the violet (top) line corresponds to experiments in this Chapter and the Chapter 8. While the pink (bottom) line corresponds to Ref. [71].

7.2.3.1 Critical Cyclotron Frequency

In the presence of rotation or synthetic magnetic fields, vortices nucleate once the cyclotron frequency exceeds the critical value $\Omega_{\rm C}^{\rm cr} = \mathcal{B}_{\rm cr}/m$. This threshold corresponds to the point where the rotational energy gain offsets the energy cost of creating a vortex. Above this value, vortices are energetically stable, and the critical frequency may be estimated as [170–172]:

$$\Omega_{\rm C}^{cr} = \frac{5\hbar}{mR_\perp^2} \ln\left(\frac{R_\perp}{\xi}\right). \tag{7.12}$$

$R_\perp = [4\mu/m\left(\omega_x^2 + \omega_y^2\right)]^{1/2}$ is the mean transverse Thomas–Fermi radius in a harmonic potential with frequencies $\omega_{x,y,z}$. The healing length $\xi = [\hbar^2/2m\mu]^{1/2}$ sets the characteristic vortex core size, where $\mu = n_0(4\pi\hbar^2 a_s/m)$ is the central mean-field

energy, a_s is the s-wave scattering length and n_0 is the central density. For the parameters in this experiment,

$$\Omega_{\mathrm{C}}^{cr}/2\pi = 29.5 \text{ Hz} \tag{7.13}$$

This form emphasizes the dependence of Ω_{C}^{cr} on the chemical potential μ and the trap geometry. Note that m^* represents the effective mass arising from Raman coupling along the $\hat{e}_x$ direction and should be taken into account. However, for Fig. 7.6a, the case $m^* = m$ is used to isolate the effect of trap geometry for comparison.

In experiments using rotation to generate a synthetic gauge field, the effective cyclotron frequency Ω_{C} differs by a factor of two from the physical rotation frequency $\Omega_{\mathrm{C}} = 2\Omega$.

7.2.3.2 Flux Quanta in a BEC

We define the synthetic magnetic flux Φ_B through a condensate with effective magnetic field $B_{\text{eff}}(x, y)$ as:

$$\Phi_B = \iint_A B_{\text{eff}}(x, y)\, dx\, dy. \tag{7.14}$$

The flux quantum for neutral atoms (with effective charge $q^* = 1$) is $\Phi_0 = \frac{h}{q^*}$,

so the flux ratio is:

$$\frac{\Phi_B}{\Phi_0} = \frac{1}{h} \iint_A B_{\text{eff}}(x, y)\, dx\, dy. \tag{7.15}$$

If the effective magnetic field is approximately uniform over the condensate area A, and we input the critical field $\mathcal{B}_{cr} = \Omega_{\mathrm{c}}^{\mathrm{cr}} m$ from Eq. 7.13, then the magnetic flux

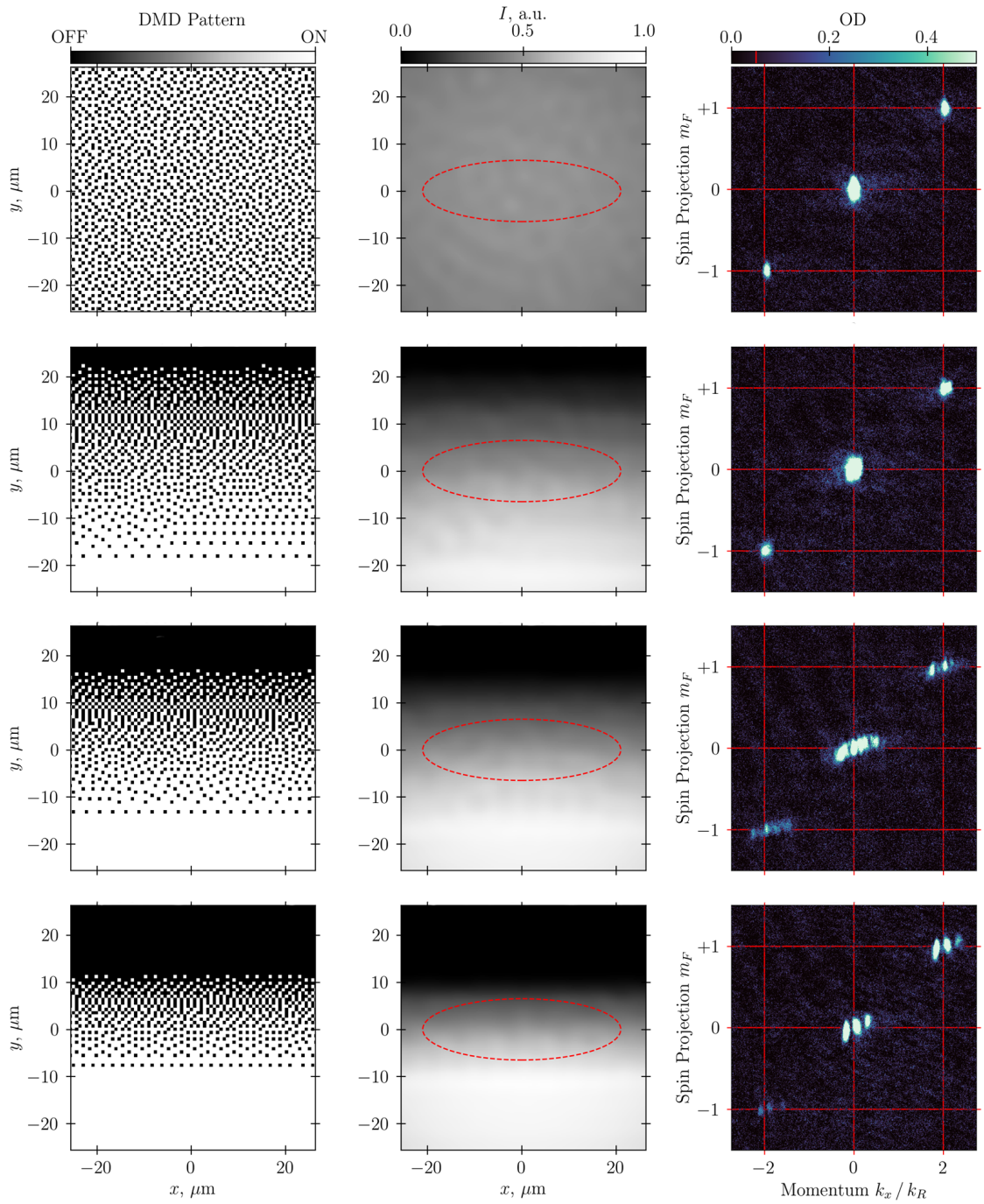

Figure 7.7: Set of time-of-flight images at various artificial field strengths–detuning gradients. The DMD patterns, intensities and optical densities (ODs) are shown for 4 different detuning gradients $[0, 0.48, 0.64, 0.97]$ kHz/um. Here, the ODs show the progression from zero shear, to slight shear, to largest shearing in the data set.

integral simplifies to:

$$\frac{\Phi_B}{\Phi_0} = \frac{A \cdot \mathcal{B}_{cr}}{h}. \tag{7.16}$$

If the condensate has an elliptical Thomas–Fermi profile with transverse radii R_x and R_y, then the area is $A = \pi R_x R_y$, and the flux ratio becomes:

$$\frac{\Phi_B}{\Phi_0} = \frac{\pi R_x R_y \cdot \mathcal{B}_{cr}}{h}. \tag{7.17}$$

This flux ratio $\frac{\Phi_B}{\Phi_0}$ is found from the detuning gradient $\delta^{'}$ with the corresponding field

$$\langle \mathcal{B} \rangle = \delta' \left\langle \frac{\partial \mathcal{A}_x}{\partial \delta} \right\rangle, \tag{7.18}$$

which serves as a measure of the *synthetic magnetic field strength* experienced by the atoms. Hence, vortices appear above a minimum gradient, when the corresponding field $\langle \mathcal{B} \rangle$ exceeds the critical field $\mathcal{B}_{cr}$. Therefore, it also provides the expected number of vortices in the condensate, assuming each vortex carries one quantum of circulation. This is a central concept in understanding vortex nucleation and vortex lattices in rotating or Raman-dressed BECs.

7.2.3.3 Shearing Parameter

The shearing motion of a condensate in time-of-flight has contributions from initial velocity and the position-dependent electric force. Here, we obtained time-of-flight images of BECs in the presence of various artificial field strengths–detuning gradients, where we observed subtle change in the shear of clouds, followed by a gigantic

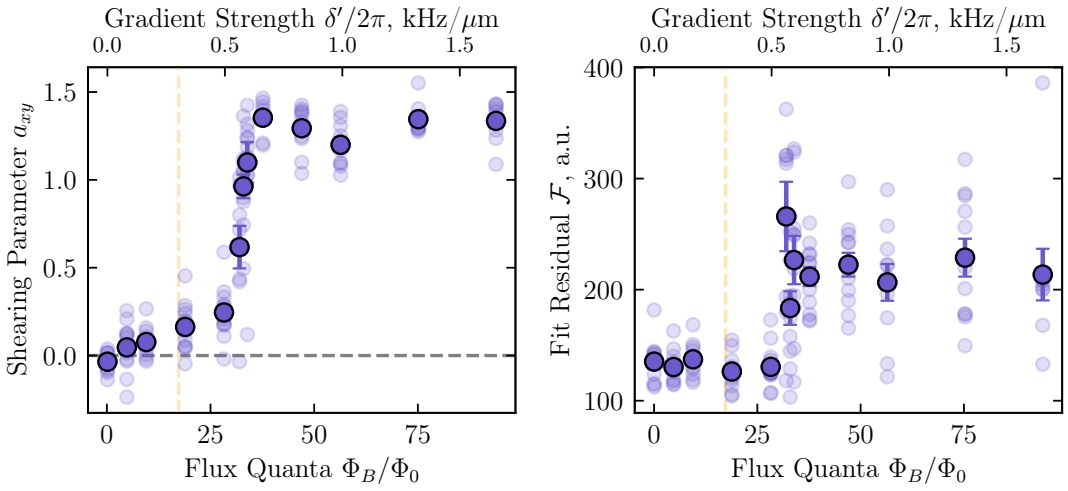

Figure 7.8: Signatures of vortex formation. Shear parameter $a_{xy}/2$ and residuals $\mathcal{F}$, are shown as functions of gradient strength $\delta'/2\pi$ and flux quanta Φ_B/Φ_0. The experimental data points (blue circles) represent averages over the measurements, with error bars indicating the standard deviation of the mean. The vertical dash line marks the expected location of the vortex nucleation transition: $\Omega_c/2\pi = 29.5$ Hz. The fit residuals $\mathcal{F}$, quantify spatial irregularity due to vortex-induced density variations. As more vortices enter the system, the spatial frequency of the time-of-flight density modulations increases, which is evident in the images in Fig. 7.7.

change when vortices enter the system. The resulting 2d column densities were fit to a sheared Thomas–Fermi profile:

$$n_{\mathrm{2D}}^{\mathrm{TOF}}(x,y) = n_0^{\mathrm{TOF}}\left[1 - \left(\frac{x^2}{R_x^2} + \frac{y^2}{R_y^2} + \frac{2a_{xy}xy}{R_xR_y}\right)\right]^{3/2}, \tag{7.19}$$

where n_0^{TOF} is the central density, R_x and R_y are the Thomas–Fermi radii, and a_{xy} is a dimensionless shear parameter. In addition, we obtain a measure of the spatial irregularity from the fit residuals:

$$\mathcal{F} = \sum_{x,y}\left[n_{\mathrm{2D}}^{\mathrm{meas}}(x,y) - n_{\mathrm{2D}}^{\mathrm{fit}}(x,y)\right]^2, \tag{7.20}$$

within the determined Thomas-Fermi radii. Figure 7.8 shows that both the shear parameter a_{xy} and residuals $\mathcal{F}$ sharply increase around 35 Φ_B/Φ_0, indicating the full transition to the BEC's vortex phase. This data is consistent with previous results reported by LeBlanc et al. in Ref. [71].

7.3 Conclusions and Outlook

We have demonstrated the implementation of light-induced artificial gauge fields generated via a DMD for ultracold atom simulators; and have succeeded in demonstrating signatures of vortex formation. This interpretation demonstrates the topological nature of vortices and highlights the utility of BECs as versatile quantum simulators of gauge fields and electromagnetic phenomena in highly tunable settings. The success with this experimental demonstration allowed us to move on with generating different position-dependent potentials with the DMD system, and study out-of-equlibrium and equilibrium regimes in the context of localization phenomena.

Chapter 8: Disordered Gauge Fields with Bose Gases

The ongoing study of disordered systems has so far revealed a variety of complex phenomena, such as Anderson localization [173–176], where quantum interference leads to constructive interference of time-reversed paths, thereby suppressing transport in the absence of interactions. In two-dimensional systems, this phenomenon manifests as weak localization [177, 178], which is well-established, and any amount of disorder can lead to localization. In the presence of a magnetic field, charged particles encircling a region of nonzero magnetic flux experience a phase shift via the Aharonov–Bohm effect [179], which modifies interference between time-reversed trajectories and can lead to destructive interference. This acquired phase alters the probability of constructive interference that underlies localization, providing the essential mechanism for the suppression of weak localization in magnetic fields. Disorder remains a highly active topic of research, as its effects can significantly alter various physical properties such as electrical conductivity [180], magnetism [181], and thermal transport.

The strong connection between weak localization and magnetic fields makes it a particularly relevant context in which to study localization phenomena. One possible route is to realize disorder through spatially varying magnetic fields, however, random magnetic fields are not a common tool in condensed matter experiments as typical fields are uniform. In addition, engineering magnetic fields that fluc-

tuate on length scales comparable to the mean free path of particles remains a considerable experimental challenge. Here, we demonstrate a new capability of arbitrary control of disordered position-dependent vector potentials and realize disordered gauge fields with ^{87}Rb BECs. This study is built on previous artifical gauge fields work [71, 95, 96, 163, 182] and the method introduced in the previous chapter, where a DMD is used to project tailored light intensity profiles, or in this context, position-dependent detunings. Here, we investigate localization physics resulting from disorder on time scales where single particle effects are dominant, as well as the temporal evolution in the regime of many body interactions. We consider the limitations of our imaging system, such as the numerical aperture and optical aberrations, to understand the statistical properties of various intensity patterns cast upon the atoms. This work opens up capabilities for studies beyond this chapter and further advances the experimental toolbox for manipulating ultracold quantum gases.

8.1 Effective Hamiltonian for Disordered Gauge Fields

The Raman-coupled Hamiltonian for a hyperfine ground state with total angular momentum F can be written in real space as

$$H = H_{\mathrm{KE}}(y,z) + \frac{\hat{p}_x^2}{2m} + \delta \hat{F}_z + \frac{\epsilon}{\hbar}\hat{F}_z^2 + \frac{\Omega}{2}\left[\hat{F}_x \cos(2k_{\mathrm{R}}x) + \hat{F}_y \sin(2k_{\mathrm{R}}x)\right], \qquad (8.1)$$

where $H_{\mathrm{KE}}(y,z)$ is the transverse kinetic term, δ is the detuning, ϵ is the quadratic Zeeman shift, and Ω is the Raman coupling strength. The position dependence

in the Raman term originates from the wavevector difference $2k_{\mathrm{R}}$ between the two Raman beams. In some cases, it is necessary to remove the explicit x-dependence of the Raman coupling. This is completed by performing a position-dependent spin rotation about $\hat{F}_z$:

$$U(x) = e^{i\,2k_{\mathrm{R}}x\hat{F}_z/\hbar}. \tag{8.2}$$

This transformation acts on the spin operators as

$$U\,\hat{F}_x\,U^\dagger = \hat{F}_x\cos(2k_{\mathrm{R}}x) + \hat{F}_y\sin(2k_{\mathrm{R}}x), \tag{8.3}$$

$$U\,\hat{F}_y\,U^\dagger = \hat{F}_y\cos(2k_{\mathrm{R}}x) - \hat{F}_x\sin(2k_{\mathrm{R}}x), \tag{8.4}$$

$$U\,\hat{F}_z\,U^\dagger = \hat{F}_z, \tag{8.5}$$

and on the momentum operator as

$$U\,\hat{p}_x\,U^\dagger = \hat{p}_x + 2\hbar k_{\mathrm{R}}\hat{F}_z. \tag{8.6}$$

Applying this transformation to Eq. (8.1) gives the rotated Hamiltonian

$$H' = U^\dagger H U = H_{\mathrm{KE}}(y,z) + \frac{1}{2m}\left(\hat{p}_x + 2k_{\mathrm{R}}\hat{F}_z\right)^2 + \delta\hat{F}_z + \frac{\varepsilon}{\hbar}\hat{F}_z^2 + \frac{\Omega}{2}\hat{F}_x. \tag{8.7}$$

In this spatially rotated frame, the Raman coupling is uniform in space, and the kinetic term acquires a minimal-coupling form in which the quasi-momentum $\hat{p}_x$ is shifted by a spin-dependent amount $2k_{\mathrm{R}}\hat{F}_z$.

For $F = 1$, the spin operators in the $\{|m_F = 0, \pm 1\rangle$ basis are

$$\hat{F}_x/\hbar = \frac{1}{\sqrt{2}} \begin{bmatrix} 0 & 1 & 0 \\ 1 & 0 & 1 \\ 0 & 1 & 0 \end{bmatrix}, \quad \hat{F}_y/\hbar = \frac{i}{\sqrt{2}} \begin{bmatrix} 0 & -1 & 0 \\ 1 & 0 & -1 \\ 0 & 1 & 0 \end{bmatrix}, \quad \hat{F}_z/\hbar = \begin{bmatrix} 1 & 0 & 0 \\ 0 & 0 & 0 \\ 0 & 0 & -1 \end{bmatrix}. \tag{8.8}$$

In summary, Hamiltonian (8.1) is the natural starting point for describing the physical Raman interactions in the laboratory frame, while Hamiltonian (**??**) is the simplified, translationally invariant representation obtained via the unitary transformation Eq. (8.2).

8.2 Experimental Characterization

Our experiments began with harmonically trapped ^{87}Rb Bose–Einstein condensates with trap frequencies $(\omega_x, \omega_y, \omega_z)/2\pi \approx (31, 130, 115)$ Hz in the $|f = 1, m_f = 0\rangle$ hyperfine state. These BECs experienced two photon Raman transitions generated by counter propagating lasers with wavelength $\lambda \approx 790$ nm and coupled the $|f = 1, m_f = 0, \pm 1\rangle$ hyperfine states with strength $\Omega \approx 9\ E_{\mathrm{R}}$). The single photon recoil wave-vector $k_R = 2\pi/\lambda$ and energy $E_{\mathrm{R}} = \hbar^2 k_R^2/2m$ specify the natural momentum and energy scales of this system. An additional upward-propagating beam from a DMD imparts a position-dependent potential and a vector light shift, resulting in an artificial gauge field proportional to the spatially varying light shift. Figure 8.1 illustrates this experimental geometry and includes the Zeeman energy level diagram of the $|f = 1, m_f = 0, \pm 1\rangle$ hyperfine states applicable for the following discussions.

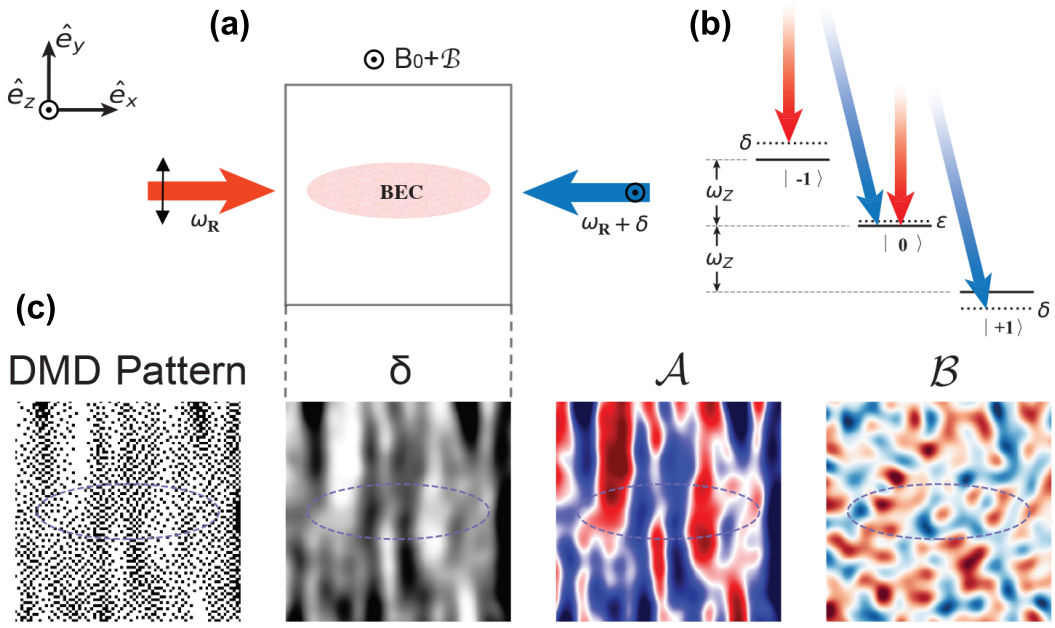

Figure 8.1: Experimental system and signatures of disordered magnetic fields. (a) Schematic of the experimental geometry: A uniform bias magnetic field $B_0\hat{e}_z$ Zeeman-splits the energy levels in the $F = 1$ manifold of ^{87}Rb, while a pair of counter-propagating Raman laser beams generate a dressed-state configuration that supports artificial gauge fields. An additional upward-propagating beam from a DMD imparts a position-dependent potential and a vector light shift, resulting in an artificial gauge field proportional to the spatially varying light shift. (b) Zeeman energy level diagram of the $|f = 1, m_f = 0, \pm 1\rangle$ hyperfine states. (c) The strips illustrate the following: the DMD encodes an arbitrary intensity pattern, which is filtered by the imaging system to yield a position-dependent detuning from the vector light shift. This light intensity profile induces a position-dependent light shift—effectively a detuning as experienced by the atoms—which imprints a spatially varying vector potential $\mathcal{A}$. The curl of this potential then gives rise to an effective magnetic field $\mathcal{B}$.

The strips depict the following: The position-dependent potential is generated by an arbitrary pattern via the DMD, where it is modeled/modified by our imaging system. This light intensity profile we are controlling provides a light shift, which is just a detuning, as interpreted by the atoms. Here, this detuning, is transmuted into a vector potential $\mathcal{A}$ that then gives rise to an effective field $\mathcal{B}\hat{e}_z$. it can be observed that the DMD pattern starts off pixelated and gets smoothed. Then no-

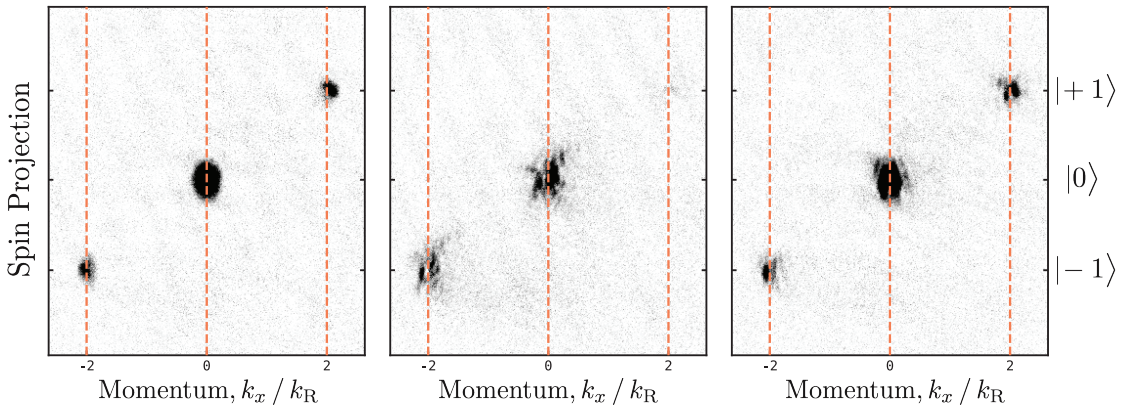

Figure 8.2: Vector light shift effect from DMD light intensity profile and its compensation in Raman-Dressed BECs. Time-of-flight images are shown for: (left) Resonant Raman-dressed states in equilibrium, (center) Raman-dressed states subject to a vector light shift (VLS) induced by the DMD light intensity profile, and (right) Raman-dressed states with a compensation detuning applied to counteract the VLS.

tice how transmuting into the vector potential, where a y-derivative is taken, makes the stripy behavior become isotropic. Also, note, the detuning and vector potential panels are very similar, this is because the quantities are almost proportional.

Calibrations of the Raman coupling strength and compensation detuning was completed via pulsing experiments. For the compensation detuning, the calibrations were completed with a flat potential intensity profile. Figure 8.2 presents time-of-flight images of: (left) Raman-dressed states in equilibrium, (center) Raman-dressed states subject to a vector light shift (VLS) induced by the DMD light intensity profile, and (right) Raman-dressed states with a compensation detuning applied to counteract the VLS.

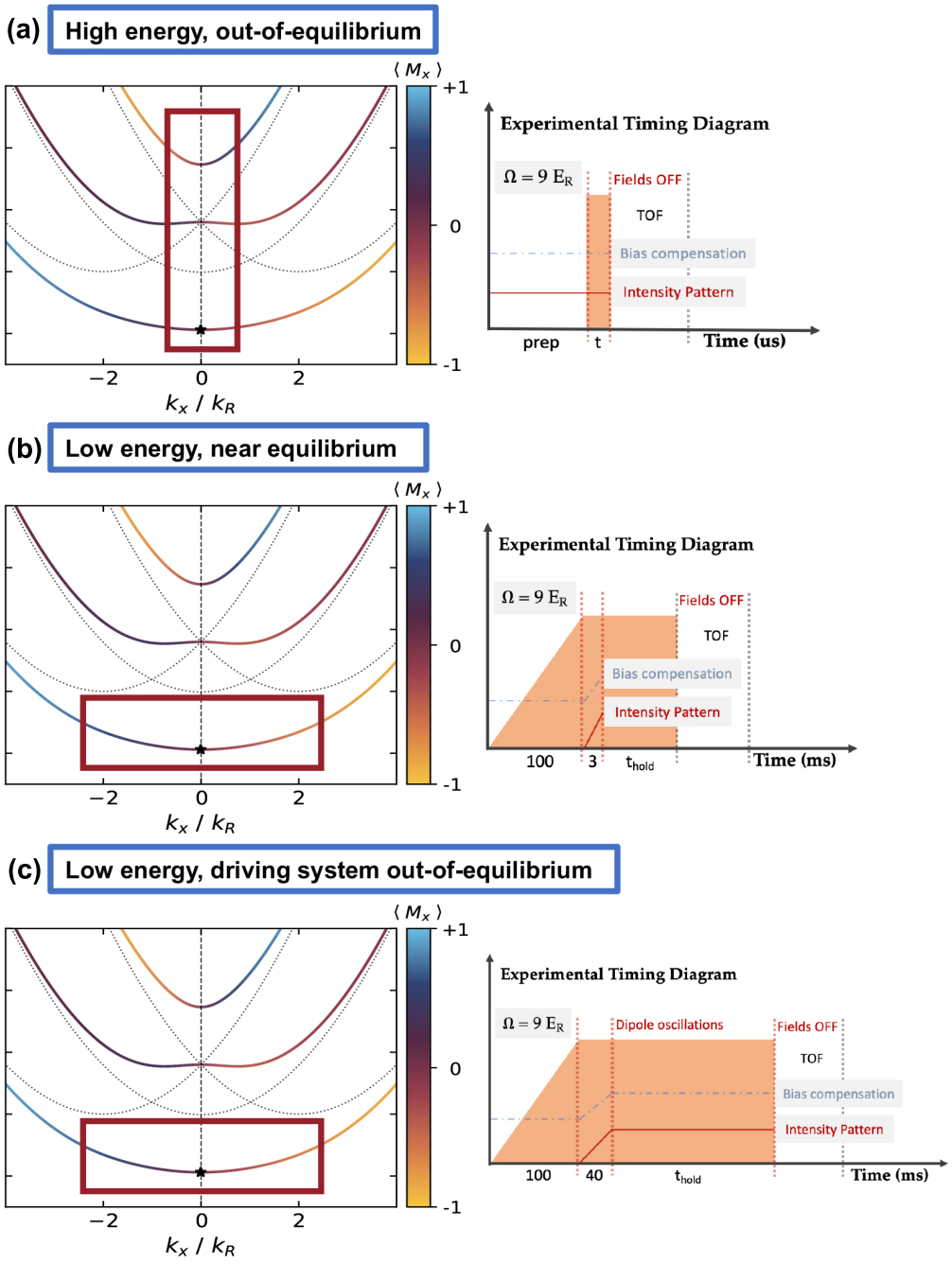

Figure 8.3: Energy regimes and corresponding timing diagrams for studies of localization physics. (a) High-energy, out-of-equilibrium: The instantaneous limit regime, where Raman pulsing experiments were performed, probing the time evolution of spin–momentum states in the presence of disorder. Low-energy: In this regime, when the Raman coupling is adiabatically turned on, the Raman-dressed states adiabatically follow the ground state of the system and the lowest energy band $E(k_x)$ is their dispersion relation. Here two experiments are described to study system response in presence of disorder, (b) Near equilibrium: Intensity patterns are ramped on in 3 ms and system is held for a variable hold time. (c) Driving system out-of-equilibrium: Intensity patterns are ramped on in 40 ms, dipole oscillations were induced, and the system is held for a variable hold time.

8.3 Signatures of Synthetic Disordered Gauge Fields

This chapter presents localization physics in BECs subjected to artificial gauge fields and controlled disorder, investigated across a range of energy and time scales in both equilibrium and out-of-equilibrium regimes. The loading protocols—including the timescales for applying the Raman coupling and disorder, as well as the disorder strength—were systematically varied to access distinct dynamical regimes.

We began with a natural starting point, the high-energy regime, or instantaneous limit–where the Hamiltonian is suddenly changed—and observe the resulting unitary evolution in the presence of disorder. Next, we study the low-energy regime where the Raman coupling is adiabatically turned on so that the Raman-dressed states follow the ground-state of the system and the lowest energy band $E(k_x)$ is their dispersion relation. We perform two different experiments to probe the system's response to disorder: 1) Near equilibrium: Intensity patterns were ramped on in 3 ms and the system is held for a variable hold time and then all fields are snapped off. Here, the position-dependent electric field kick experienced by the atoms is observed. 2) Driving system out-of-equilibrium: Intensity patterns were ramped on over 40 ms, dipole oscillations were then induced, and the system is held for variable hold times. Here we plot the damping rate and frequency dependence on disorder strength. Together, these measurements map the interplay between energy scale, disorder, and equilibrium – nonequilibrium evolution of our system. Figure 8.3 illustrates the relevant energy regimes and corresponding experimental timing diagrams.

8.3.1 High-Energy, Out-Of-Equilibrium

The high-energy regime, i.e. instantaneous limit, the Hamiltonian is suddenly changed and the resulting unitary evolution is in the basis of the original bare states. Atoms are initially prepared in the magnetically insensitive $|f = 1, m_f = 0\rangle$ hyperfine state and are then abruptly subjected to Raman coupling. This sudden coupling projects the atoms into a superposition of the $|f = 1, m_f = 0, \pm 1\rangle$, after which the system evolves unitarily under the new Hamiltonian. These experiments were conducted with a coupling strength of $9.5E_{\mathrm{R}}$ and at a fixed pulse time = 28μs, where the spin–momentum states were in the presence of disorder. The disorder strength was controlled via the DMD while keeping the average light intensity fixed and with each experimental shot corresponding to a different intensity pattern realization.

In this regime, the behavior is well described by single-particle physics. Figure 8.4a shows the time evolution, i.e. the fractional populations of the spin-momentum states as a function of the pulse time. Notice that it looks almost exactly as it would without disorder, except that when you look close, meaningful statistical variations from shot-to-shot are noticeable from the overall probability of arriving in these spin states. During the time evolution, the disorder was present throughout the duration of the pulse, in addition to a compensation detuning-that accounts for the vector light shift induced by the DMD intensity profile. Figure 8.4b plots the magnetization and its standard deviation as a function of disorder strength for a pulse time t = 28μs where the errorbars are significant and there's a good signal. This data shows that

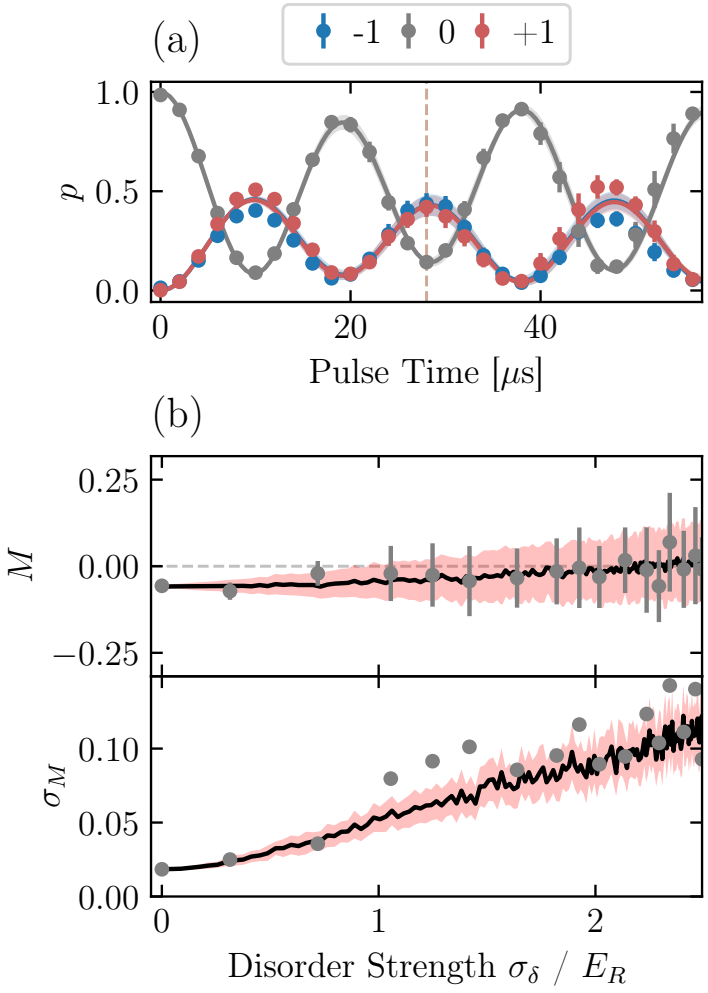

Figure 8.4: Spin-momentum states in the presence of disorder. In the high-energy, out-of-equilibrium regime, Raman pulsing experiments were performed with a coupling strength of $\Omega = 9.5E_{\mathrm{R}}$. (a) Typical time evolution of spin–momentum states in the presence of disorder at a detuning of $\hbar\delta = 2.5, E_{\mathrm{R}}$. The dashed vertical line indicates the fixed pulse time duration of 28 μs used in the experiments. (b) Here the magnetization and its standard deviation σ_M are plotted as a function of disorder strength. Monte Carlo simulations of single particle evolution (black curves), (150 realizations per disorder strength across 5×10^3 ensembles), demonstrate agreement with the experimental data (gray circles). The shaded red region reflects single sigma uncertainty across the realizations.

as the disorder strength increases, the observed uncertainty increases (marked by the gray errorbars). This is in line with Monte Carlo simulations, represented by solid lines, that predicts these error bands in shaded pink (propagated uncertainty

due to variation from input parameters). The simulations were performed using 150 disorder realizations per disorder strength across 5k random ensembles. The simulation results were fitted to the time evolution (black curves) and demonstrate agreement with the averaged data (gray circles), and in good quantitative agreement with observed experimental uncertainties. Here this data shows how these pulses drove detuning dynamics, leading to inhomogeneous global magnetization. However, this high-energy regime doesn't resolve any of the physics in the spin states. Next, we'll investigate physics where the atoms are adiabatically loaded.

8.3.2 Low-Energy, Near Equilibrium

To further probe localization physics, we perform an experiment in which atoms initially at equilibrium are subjected to pulsed disorder. We measure the maximum vector potential inferred from the condensate widths and determine the characteristic timescale for the atoms to travel approximately one correlation length in the presence of disorder.

Atoms are adiabatically loaded into the Raman-dressed states in 100 ms, where they follow the ground-state of the system and the lowest energy band $E(k_x)$ is their dispersion relation. Disorder was then introduced via a distinct timing protocol: a rapid 3 ms ramp on, where the atoms suddenly experience disorder. During this timing protocol, the Zeeman shift was simultaneously ramped on (refer to experimental timing diagram in Fig. 8.3b) to compensate the vector light shift, as demonstrated in Fig. 8.2. The system was then held for a dynamic hold time, vary-

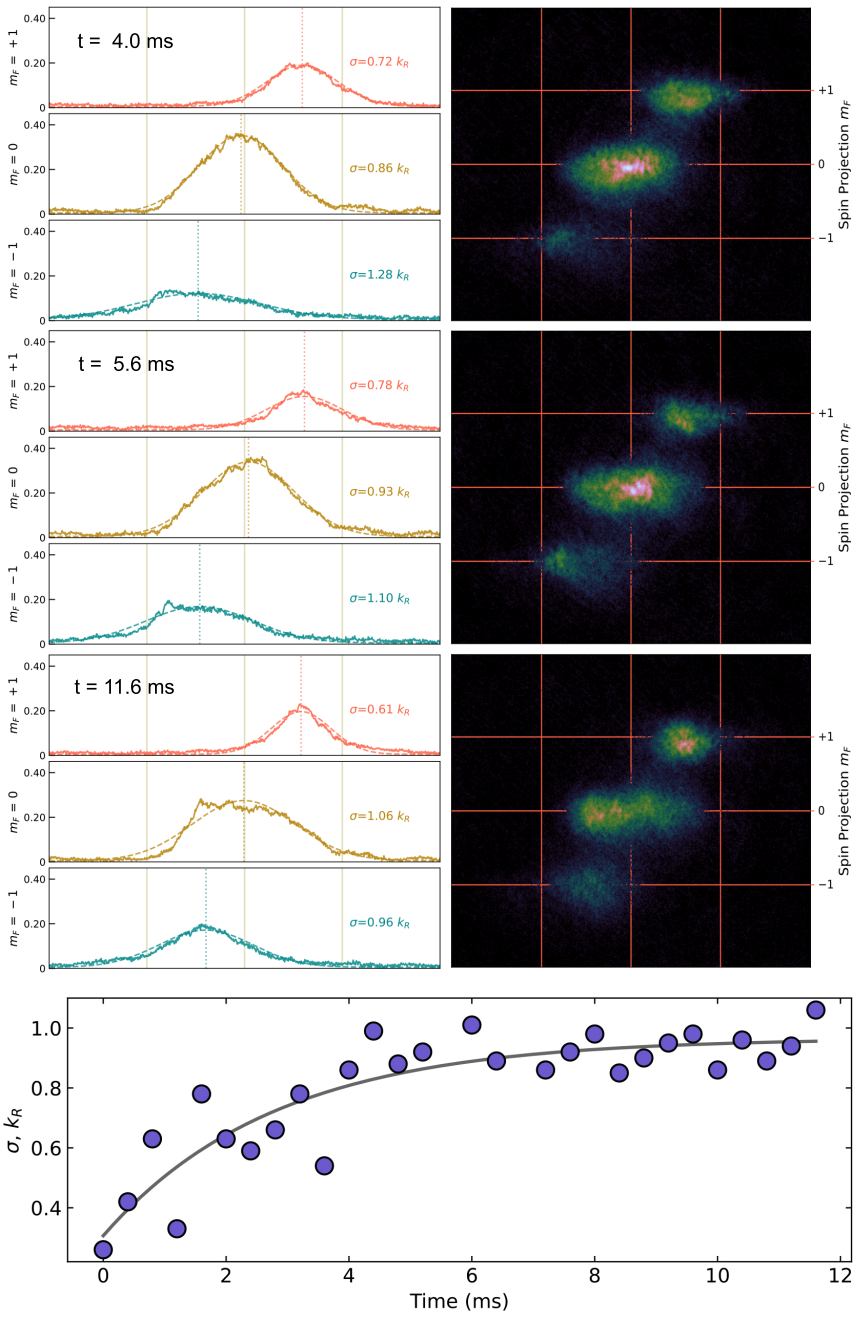

Figure 8.5: Raman-dressed states in the presence of pulsed disorder. Shown are a series of time-of-flight images along with their corresponding averaged optical density (OD) cross-sections (solid lines) and 1d Gaussian widths (dashed lines) for the Raman-dressed spin-momentum states, $|F = 1, m_F = 0, \pm 1\rangle$, subjected to a fixed disorder strength of 1.78 $\mathrm{E_R}$ at times $t = [4.0, 5.6, 11.6]$ ms. The averaged width σ of the $|F = 1, m_f = 0\rangle$ state is plotted as a function of time from 0–12 ms, providing an estimate of the effective vector potentials generated by the disorder, with a maximum of $1\,k_\mathrm{R}$ recoil.

ing from 0 to 12 ms. Immediately after, all control fields and harmonic trapping were suddenly turned off, and the atoms were then Stern-Gerlach imaged after a 15 ms time-of-flight.

During this short time, atoms experience a position-dependent electric field kick, via $\delta\mathcal{A}/\delta t$. As a result, the atoms acquire velocity in different directions but their momentum remains $k = 0$. As the atoms move, they move balistically and they find themselves in places with different vector potentials. Then, when the disorder is snapped off, the atoms experience a different position-dependent electric field kick. This approach enabled a systematic study of the dynamical response of Raman-dressed states in the presence of disorder, as a function of time. Figure 8.5 shows representative time-of-flight images, their corresponding OD cross-sections (solid lines), and 1d Gaussian fits (dashed lines) for the Raman-dressed spin-momentum states, $|F = 1, m_f = 0, \pm 1\rangle$, subject to a fixed disorder strength of 1.78 $\mathrm{E_R}$ at times t=$[4.0, 5.6, 11.6]$ ms. Each image and cross-section represents an average of 4 images with different disorder realizations. The averaged width σ of the $|F = 1, m_f = 0\rangle$ state is plotted as a function of time from 0–12 ms. The increase in width reflects the momentum acquired over a range of momenta, with a maximum corresponding to roughly one recoil momentum, $1k_{\mathrm{R}}$. For atoms moving one correlation length (≈ 3 μm, inferred from the imaging resolution of the system) over a 3 ms timescale, the corresponding velocity is approximately 1 μm/ms. Thus, the maximum observed width provides an estimate of the effective vector potential generated by the disorder.

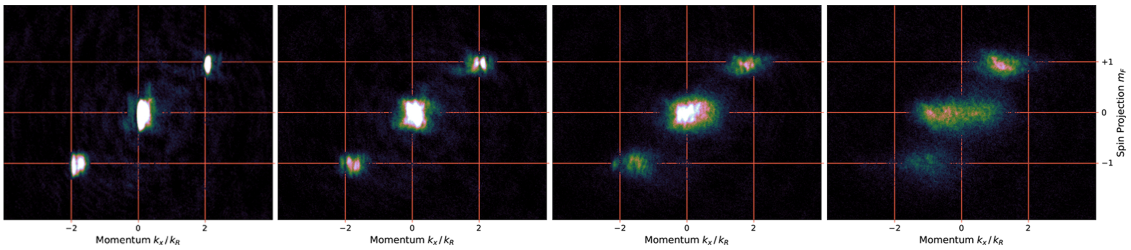

Figure 8.6: Raman-dressed states in the presence of pulsed disorder. Shown are a series of time-of-flight images for the Raman-dressed spin-momentum states, $|F = 1, m_F = 0, \pm 1\rangle$, subjected to disorder strength $\sigma_{\mathrm{I}} = [0, 0.70, 1.04, 1.78]$ $\mathrm{E_R}$ at a fixed time $t = 9.6$ ms.

Figure 8.6 shows a series of time-of-flight images for the Raman-dressed spin-momentum states, $|F = 1, m_F = 0, \pm 1\rangle$, subjected to disorder strength $\sigma_{\mathrm{I}} = [0, 0.70, 1.04, 1.78]$ $\mathrm{E_R}$ at a fixed time $t = 9.6$ ms. Here, it is also evident that the BEC widths increase as a function of the disorder strength. Since our experiments were conducted with ^{87}Rb atoms, s-wave scattering was found to be significant, especially for times $t < 5$ ms, slightly offsetting our width measurements. Nevertheless, our results demonstrate a measurable increase in BEC width as a function of disorder strength as well as time, as shown above.

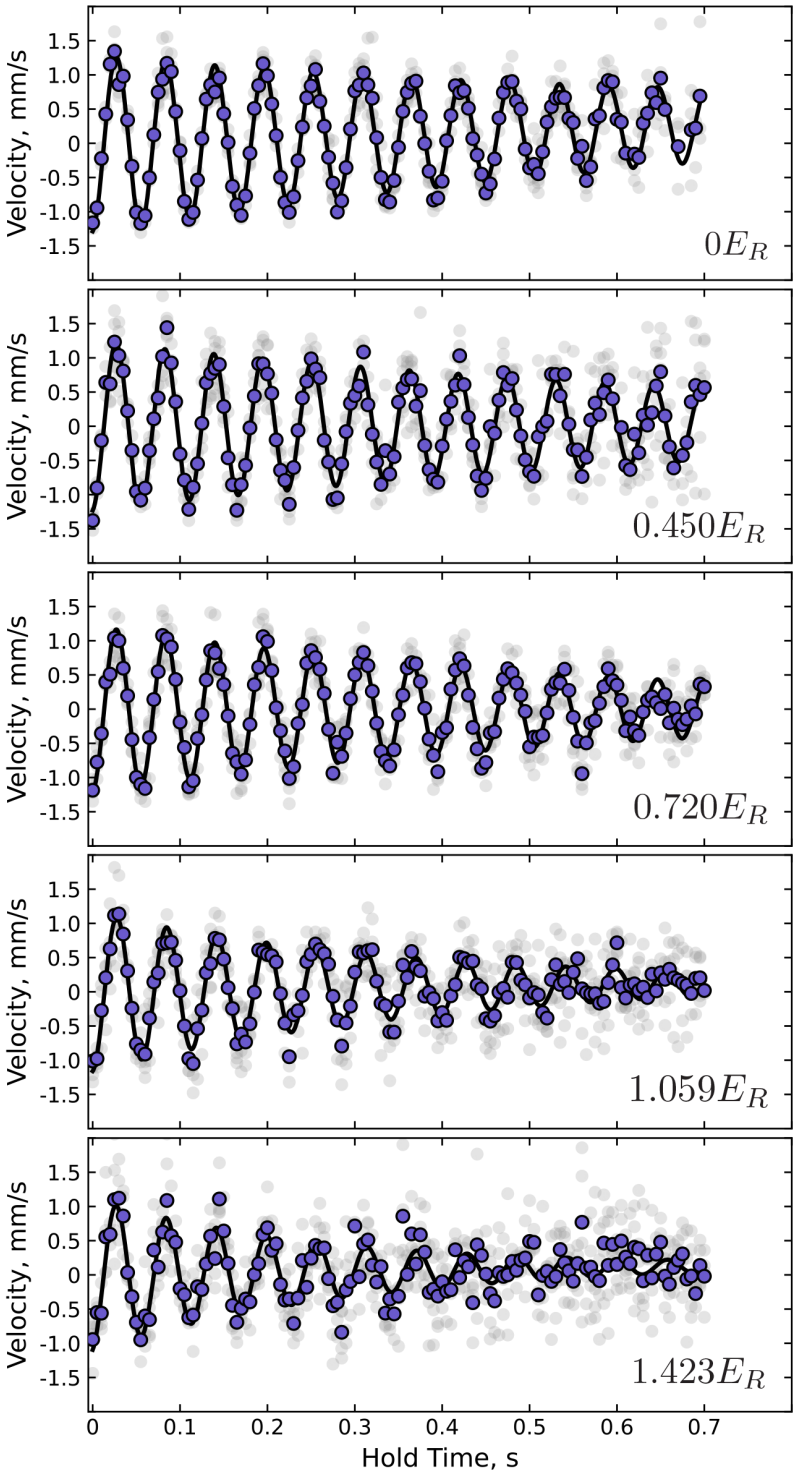

Figure 8.7: Driving system out of equilibrium and the effect of disorder. Here, dipole oscillations are plotted for different disorder strengths = $[0, 0.45, 0.72, 1.06, 1.4]$ E_{R}. The dark blue markers represent the average velocity for each time t.

8.3.3 Low-Energy, Driving System Out-Of-Equilibrium

A characteristic feature of localization is the suppression of coherent transport, which can be observed through the damping of collective oscillations in trapped BECs. To probe this effect, we studied how the damping of dipole oscillations and the effective trap frequency—modified by Raman coupling—depend on the strength of disorder.

Experiments were performed by first adiabatically loading the BEC into the Raman-dressed state, followed by ramping on disorder over 40 ms. Dipole oscillations were then induced to drive the system out of equilibrium, and the response was studied in the presence of disorder. A set of five experiments were conducted for disorder strengths of $[0, 0.45, 0.72, 1.06, 1.4]$ E_{R}, and are presented in Fig. 8.7. For each evolution time t, twelve experimental realizations were recorded, and the dark-blue markers indicate the average velocity at each time.

As expected, disorder induced damping of the dipole oscillations, with stronger disorder leading to faster decay. The time-dependent oscillations were fitted with a damped sinusoidal function of the form

$$x(t) = A\cos(\omega t + \phi), e^{-t/\tau}, \tag{8.9}$$

where A is the oscillation amplitude, ω is the oscillation frequency, ϕ is the phase, and τ is the damping time. The damping rate $1/\tau$ was extracted from the fitted decay constant, and the oscillation frequency ω was obtained from the same fit. Fig-

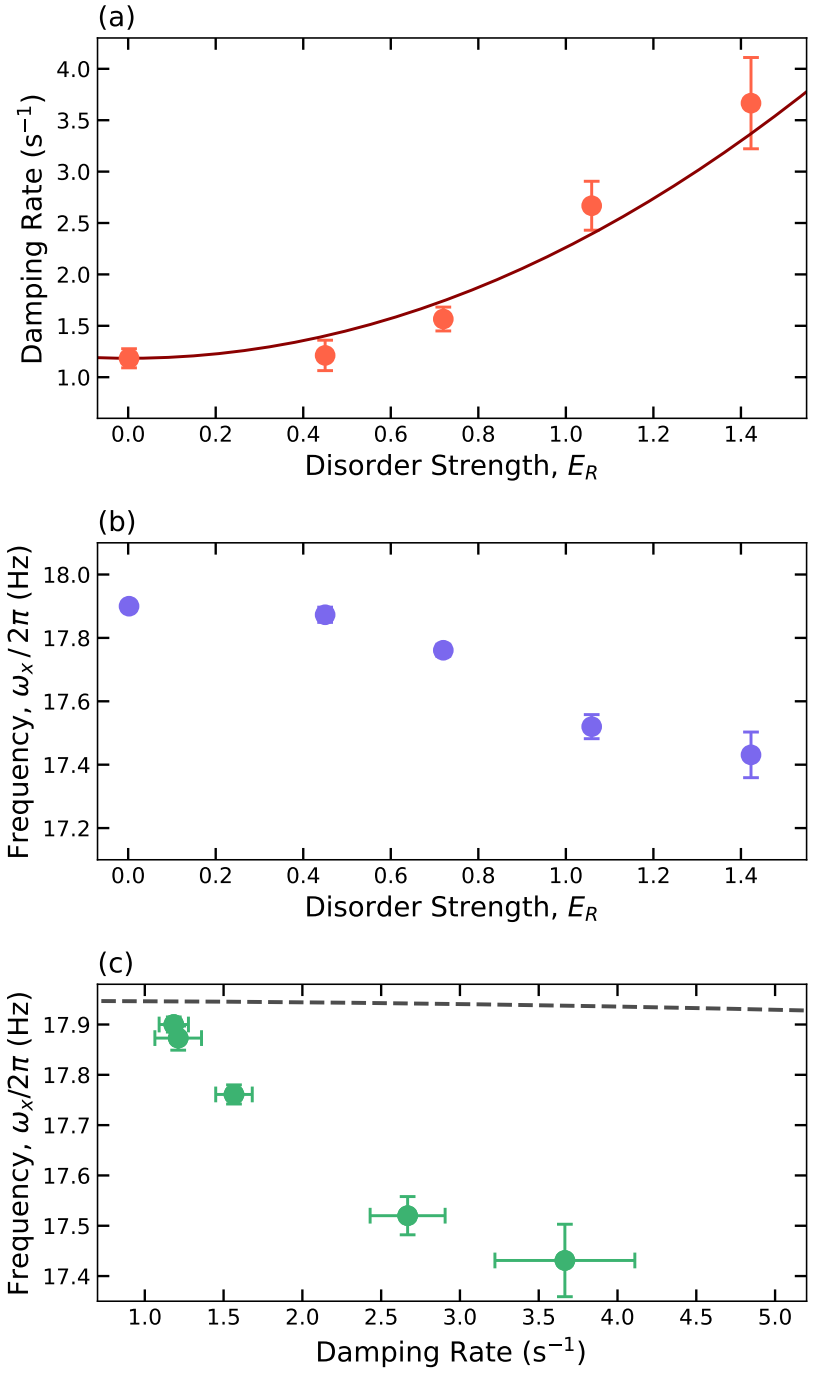

Figure 8.8: Damping rate and frequency dependence on disorder strength. (a) Damping rate $1/\tau$ as a function of disorder strength. The curve is a quadratic polynomial curve included to guide the eye. (b) Frequency as a function of disorder strength. (c) Frequency as function of Damping rate for comparison with a damped harmonic oscillator. Here, we observe that the data depart from the simple damped HO prediction as disorder increases.

ure 8.8a shows the damping rate as a function of disorder strength, with a quadratic polynomial curve included to guide the eye. Figure 8.8b shows the corresponding oscillation frequencies, highlighting shifts in the Raman-modified trap frequency. Interestingly, we observe deviation from a simple damped harmonic oscillator, where it becomes apparent at higher disorder strengths. These deviations are found by comparing the measured frequencies to the damped HO model

$$\omega_{\text{damped}} = \omega_0 \sqrt{1 - \left(\frac{\gamma}{2\pi\omega_0}\right)^2},$$

where ω_0 is the undamped trap frequency and $\gamma = 1/\tau$ is the damping rate. Figure 8.8c presents this comparison, plotting frequency as a function of the decay rate, and clearly shows that the data depart from the simple damped HO prediction as disorder increases, giving insight that this disorder has properties beyond those of a random potential.

8.4 Conclusions and Outlook

The work presented in this chapter has demonstrated the implementation of experimental techniques for generating disordered vector potentials and magnetic fields in Raman-dressed atomic systems. This approach of generating optical fields by projecting intensity patterns has established a new framework for investigating artificial gauge fields with ultracold atoms and related platforms. In particular, this technique opens pathways to probing localization phenomena in equilibrium conditions, studying weak localization effects using the implemented TEM_{01} trap, examining

vortex pinning, and realizing a range of additional models through programmable intensity patterns engineered with the DMD.

In the high-energy regime, pulsed measurements showed very good agreement with Monte Carlo simulations. Since our experiments were conducted with interacting bosons, s-wave scattering played a noticeable role in the low-energy, near-equilibrium regime, introducing deviations in width measurements. Even so, we observed a clear increase in BEC width along the Raman coupling direction. In the low-energy equilibrium regime, dipole oscillations were induced to drive the system out-of-equilibrium. In these experiments, disorder caused substantial damping of dipole oscillations, consistent with expectations of localization signatures. In addition, we observed deviation from a simple damped harmonic oscillator for the Raman-modified frequency shifts. Altogether, these results validate the experimental techniques developed in the previous chapter as well as this chapter, and position the continued generation of intensity fields as a foundation for future, more advanced quantum simulation studies of disordered gauge fields.

Chapter 9: Conclusion and Outlook

This thesis presented new experimental techniques for controlling and characterizing artificial gauge fields combined with intensity fields. These methods establish a versatile platform for future investigations of disordered gauge fields with ultracold atoms and related systems—enabling studies of localization dynamics, weak localization phenomena using the implemented TEM_{01} trap, vortex pinning, and other models made accessible through tailored intensity patterns generated by the DMD. Future work on the RbK apparatus will likely focus on enhancing imaging capabilities, refining the DMD optical systems, and incorporating time-dependence via the dynamic DMD capabilities. Such developments would enable the exploration of time-dependent noise, thereby extending studies to noisy quantum systems.

Looking forward, a central objective of quantum simulation research is to explore computationally demanding models. Continued advances in quantum simulation techniques will not only strengthen the capabilities of existing platforms but also extend their applicability to a broader class of models and to other fields.

Bibliography

[1] M. Inguscio, W. Ketterle, and C. Salomon. Ultracold fermi gases. In M. Inguscio, W. Ketterle, and C. Salomon, editors, *Proceedings of the International School of Physics "Enrico Fermi", Course CLXIV, Varenna, 20–30 June 2006*. IOS Press, Amsterdam, 2008.

[2] Allan Adams, Lincoln D. Carr, Thomas Schäfer, Peter Steinberg, and John E. Thomas. Strongly correlated quantum fluids: Ultracold quantum gases, quantum chromodynamic plasmas and holographic duality. *New Journal of Physics*, 14:115009, 2012.

[3] Michael Schreiber, Sean S. Hodgman, Pranjal Bordia, Henrik P. Lüschen, Mark H. Fischer, Ronen Vosk, Ehud Altman, Ulrich Schneider, and Immanuel Bloch. Observation of many-body localization of interacting fermions in a quasirandom optical lattice. *Science*, 349(6250):842–845, 2015.

[4] Y.-J. Lin, K. Jiménez-García, and Ian B. Spielman. Spin–orbit-coupled bose–einstein condensates. *Nature*, 471:83–86, 2011.

[5] T. Ozawa and H. M. Price. Topological quantum matter in synthetic dimensions. *Nature Reviews Physics*, 1:349–357, 2019.

[6] Ehud Altman, Kenneth R. Brown, Giuseppe Carleo, Lincoln D. Carr, Eugene Demler, Cheng Chin, Brian DeMarco, Sophia E. Economou, Mark A. Eriksson, Kai-Mei C. Fu, et al. Quantum simulators: Architectures and opportunities. *PRX Quantum*, 2(1):017003, 2021.

[7] Hannes Bernien, Sylvain Schwartz, Alexander Keesling, Harry Levine, Ahmed Omran, Hannes Pichler, Soonwon Choi, Alexander S. Zibrov, Manuel Endres, Markus Greiner, Vladan Vuletić, and Mikhail D. Lukin. Probing many-body dynamics on a 51-atom quantum simulator. *Nature*, 551:579–584, 2017.

[8] Rainer Blatt and Christian F. Roos. Quantum simulations with trapped ions. *Nature Physics*, 8:277–284, 2012.

[9] J. Zhang, G. Pagano, P. W. Hess, A. Kyprianidis, P. Becker, H. Kaplan, A. V. Gorshkov, Z. X. Gong, and C. Monroe. Observation of a many-body dynamical phase transition with a 53-qubit quantum simulator. *Nature*, 551:601–604, 2017.

[10] Joseph W. Britton, Brian C. Sawyer, Adam C. Keith, C.-C. Joseph Wang, James K. Freericks, Hermann Uys, Michael J. Biercuk, and John J. Bollinger. Engineered two-dimensional Ising interactions in a trapped-ion quantum simulator with hundreds of spins. *Nature*, 484:489–492, 2012.

[11] Justin G. Bohnet, Brian C. Sawyer, Joseph W. Britton, Michael L. Wall, Ana Maria Rey, Michael Foss-Feig, and John J. Bollinger. Quantum spin dynamics and entanglement generation with hundreds of trapped ions. *Science*, 352:1297–1301, 2016.

[12] Nicholas C. Harris, Mihika Prabhu, Gregory R. Steinbrecher, Yoav Lahini, Jacob Mower, Darius Bunandar, Changchen Chen, Franco N. C. Wong, Tom Baehr-Jones, Michael Hochberg, Seth Lloyd, and Dirk Englund. Quantum transport simulations in a programmable nanophotonic processor. *Nature Photonics*, 11:447–452, 2017.

[13] S. N. Bose. Plancks gesetz und lichtquantenhypothese. *Z. Phys.*, 26:178, 1924.

[14] A. Einstein. Quantentheorie des einatomigen idealen gases. *Sitzungsberichte/ Physikalische Klasse, Preussische Akademie der Wissenschaften*, 22:261, 1924.

[15] Enrico Fermi. Sulla quantizzazione del gas perfetto monoatomico. *Rend. Lincei*, 3:145–149, 1926.

[16] P. A. M. Dirac. On the theory of quantum mechanics. *Proceedings of the Royal Society of London Series A*, 112(762):661–677, oct 1926.

[17] William D. Phillips. Laser cooling and trapping of neutral atoms. *Reviews of Modern Physics*, 70(3):721–741, July 1998.

[18] C. Cohen-Tannoudji and W. D. Phillips. Atoms in a light trap. *Physics Today*, 43(10):33–40, 1990.

[19] Rudolf Grimm, Matthias Weidemüller, and Yurii B. Ovchinnikov. Optical dipole traps for neutral atoms. *Advances In Atomic, Molecular, and Optical Physics*, 42:95–170, 2000. Max-Planck-Institut für Kernphysik, 69029 Heidelberg, Germany; National Institute of Standards and Technology, PHY B167, Gaithersburg, MD 20899, USA.

[20] E. L. Raab, M. Prentiss, A. Cable, S. Chu, and D. E. Pritchard. Trapping of neutral sodium atoms with radiation pressure. *Physical Review Letters*, 59(23):2631–2634, 1987.

[21] M. H. Anderson, J. R. Ensher, M. R. Matthews, C. E. Wieman, and E. A. Cornell. Observation of bose-einstein condensation in a dilute atomic vapor. *Science*, 269(5221):198–201, 1995.

[22] K. B. Davis, M.-O. Mewes, M. R. Andrews, N. J. van Druten, D. S. Durfee, D. M. Kurn, and W. Ketterle. Bose–einstein condensation in a gas of sodium atoms. *Phys. Rev. Lett.*, 75:3969–3973, 1995.

[23] B. DeMarco and D. S. Jin. Onset of fermi degeneracy in a trapped atomic gas. *Science*, 285(5434):1703–1706, September 1999.

[24] Andrew G. Truscott, Kevin E. Strecker, William I. McAlexander, Guthrie B. Partridge, and Randall G. Hulet. Observation of fermi pressure in a gas of trapped atoms. *Science*, 291(5513):2570–2572, March 2001.

[25] Z. Hadzibabic, C. A. Stan, K. Dieckmann, S. Gupta, M. W. Zwierlein, A. Görlitz, and W. Ketterle. Two-species mixture of quantum degenerate bose and fermi gases. *Physical Review Letters*, 88(16):160401, April 2002.

[26] K. M. O'Hara, S. L. Hemmer, M. E. Gehm, S. R. Granade, and J. E. Thomas. Observation of a strongly interacting degenerate fermi gas of atoms. *Science*, 298(5601):2179–2182, December 2002.

[27] Immanuel Bloch, Jean Dalibard, and Sylvain Nascimbene. Quantum simulations with ultracold quantum gases. *Nature Physics*, 8(4):267–276, 2012.

[28] Panagiotis Christodoulou, Maciej Gałka, Nishant Dogra, Raphael Lopes, Julian Schmitt, and Zoran Hadzibabic. Observation of first and second sound in a BKT superfluid. *Nature*, 594:191–194, 2021.

[29] Y.-Q. Zou, É. Le Cerf, B. Bakkali-Hassani, C. Maury, G. Chauveau, P. C. M. Castilho, R. Saint-Jalm, S. Nascimbène, J. Dalibard, and J. Beugnon. Optical control of the density and spin spatial profiles of a planar bose gas. *J. Phys. B: At. Mol. Opt. Phys.*, 54:08LT01, 2021.

[30] S. Eckel, A. Kumar, T. Jacobson, I. B. Spielman, and G. K. Campbell. A rapidly expanding bose-einstein condensate: An expanding universe in the lab. *Phys. Rev. X*, 8:021021, Apr 2018.

[31] P. A. M. Dirac. The quantum theory of the electron. *Proceedings of the Royal Society of London A: Mathematical, Physical and Engineering Sciences*, 117(778):610–624, 1928.

[32] Fritz Sauter. Über das verhalten eines elektrons im homogenen elektrischen feld nach der relativistischen theorie diracs. *Zeitschrift für Physik*, 69(11):742–764, Nov 1931.

[33] W. Heisenberg. Bemerkungen zur diracschen theorie des positrons. *Zeitschrift für Physik*, 90(3):209–231, Mar 1934.

[34] W. Heisenberg and H. Euler. Folgerungen aus der diracschen theorie des positrons. *Zeitschr. Phys.*, 98(714), 1936.

[35] Julian Schwinger. On gauge invariance and vacuum polarization. *Phys. Rev.*, 82:664–679, Jun 1951.

[36] A. M. Pineiro, D. Genkina, Mingwu Lu, and I B Spielman. Sauter–schwinger effect with a quantum gas. *New J. Phys.*, 21:083035, 2019.

[37] Mingwu Lu, G. H. Reid, A. R. Fritsch, A. M. Piñeiro, and I. B. Spielman. Floquet engineering topological dirac bands. *Phys. Rev. Lett.*, 129:040402, Jul 2022.

[38] Christopher J Foot. *Atomic physics*. OUP, Oxford, 2004.

[39] Daniel A. Steck. Rubidium 87 d line data. http://steck.us/alkalidata, 2001. Revision 2.2.2, 9 July 2021.

[40] Enrico Fermi. Über die magnetischen momente der atomkerne. *Zeitschrift für Physik*, 60:320–333, 1930.

[41] L. Jr. Armstrong. *Theory of the Hyperfine Structure of Free Atoms*. John Wiley Sons, Inc., NewYork, 1971.

[42] Ennio Arimondo, M. Inguscio, and P. Violino. Experimental determinations of the hyperfine structure in the alkali atoms. *Reviews of Modern Physics*, 49(1):31–75, 1977.

[43] Gregory Breit and I. I. Rabi. Measurement of nuclear spin. *Physical Review*, 38(11):2082–2083, 1931.

[44] I. I. Rabi. Space quantization in a gyrating magnetic field. *Physical Review*, 51(8):652–654, April 1937.

[45] Christopher J. Foot. *Atomic Physics*. Oxford University Press, 2005.

[46] Daniel A. Steck. Quantum and atom optics. http://steck.us/teaching, 2007. Revision 0.13.15, 28 July 2022.

[47] Harold J. Metcalf and Peter van der Straten. *Laser Cooling and Trapping*. Springer, New York, 1999.

[48] Nouredine Zettili. *Quantum Mechanics: Concepts and Applications*. Wiley, 2nd edition, 2009.

[49] L. P. Pitaevskii and S. Stringari. *Bose-Einstein Condensation*. Clarendon Press, Oxford, 2003.

[50] Christopher Pethick and Henrik Smith. *Bose-Einstein Condensation in Dilute Gases*. Cambridge University Press, Cambridge, New York, 2008.

[51] W. Ketterle, D. S. Durfee, and D. M. Stamper-Kurn. Making, probing and understanding bose-einstein condensates. In M. Inguscio, S. Stringari, and C. E. Wieman, editors, *Proceedings of the International School of Physics "Enrico Fermi"*, volume 140, pages 67–176. IOS Press, 1999.

[52] Y.-J. Lin, A. R. Perry, R. L. Compton, I. B. Spielman, and J. V. Porto. Rapid production of ^{87}rb bose–einstein condensates in a combined magnetic and optical potential. *Physical Review A*, 79(6):063631, 2009.

[53] Mehran Kardar. *Statistical Physics of Particles*. Cambridge University Press, 2007.

[54] R. K. Pathria and Paul D. Beale. *Statistical Mechanics*. Academic Press, Boston, 2011.

[55] Silvio R. A. Salinas. *Introduction to Statistical Physics*. Springer, New York, 2001.

[56] James Sethna. *Statistical Mechanics: Entropy, Order Parameters, and Complexity*. Oxford University Press, Oxford, New York, 2006.

[57] J. J. Sakurai. *Modern Quantum Mechanics*. Benjamin/Cummings, Menlo Park, Calif, 1985.

[58] E.G.M. van Kempen, S.J.J.M.F. Kokkelmans, D.J. Heinzen, and B.J. Verhaar. Interisotope determination of ultracold rubidium interactions from three high-precision experiments. *Phys. Rev. Lett.*, 88:093201, 2002.

[59] Artur Widera, Fabrice Gerbier, Simon Fölling, Tim Gericke, Olaf Mandel, and Immanuel Bloch. Precision measurement of spin-dependent interaction strengths for spin-1 and spin-2 ^{87}rb atoms. *New J. Phys.*, 8:152, 2006.

[60] N.N. Klausen, J.L. Bohn, and C.H. Greene. Nature of spinor bose-einstein condensates in rubidium. *Phys. Rev. A*, 64:053602, 2001.

[61] Michael Tinkham. *Group Theory and Quantum Mechanics*. Dover Publications, 2003.

[62] E. P. Gross. Structure of a quantized vortex in boson systems. *Il Nuovo Cimento*, 20(3):454–477, 1961.

[63] L. P. Pitaevskii. Vortex lines in an imperfect bose gas. *Zh. Eksp. Teor. Fiz.*, 40:646, 1961.

[64] Eugene P. Gross. Hydrodynamics of a superfluid condensate. *Journal of Mathematical Physics*, 4(2):195–207, 1963.

[65] Y. Castin and R. Dum. Bose-einstein condensates in time dependent traps. *Physical Review Letters*, 77(27):5315–5319, 1996.

[66] Franco Dalfovo, Stefano Giorgini, Lev P. Pitaevskii, and Sandro Stringari. Theory of bose-einstein condensation in trapped gases. *Reviews of Modern Physics*, 71(3):463–512, 1999.

[67] Elliott H. Lieb, Robert Seiringer, and Jakob Yngvason. Bosons in a trap: A rigorous derivation of the gross-pitaevskii energy functional. *Physical Review A*, 61(4):043602, March 2000.

[68] Andika Putra. *Magnetized Plane Wave and Stripe-Ordered Phases in Spin-Orbit-Coupled Bose Gases*. Ph.d. dissertation, University of Maryland, College Park, 2018.

[69] László Erdős, Benjamin Schlein, and Horng-Tzer Yau. Derivation of the gross–pitaevskii equation for the dynamics of bose–einstein condensate. *Annals of Mathematics*, 172(1):291–370, 2010.

[70] C. J. Pethick and H. Smith. *Bose–Einstein Condensation in Dilute Gases*. Cambridge University Press, Cambridge, 2nd edition, 2008.

[71] L J LeBlanc, K Jiménez-García, R A Williams, M C Beeler, W D Phillips, and I B Spielman. Gauge matters: observing the vortex-nucleation transition in a bose condensate. *New Journal of Physics*, 17(6):065016, jun 2015.

[72] Richard J. Fletcher, Airlia Shaffer, Cédric C. Wilson, Parth B. Patel, Zhenjie Yan, Valentin Crépel, Biswaroop Mukherjee, and Martin W. Zwierlein. Geometric squeezing into the lowest Landau level. *Science*, 372(6548):1318–1322, 2021.

[73] Biswaroop Mukherjee, Airlia Shaffer, Parth B. Patel, Zhenjie Yan, Cédric C. Wilson, Valentin Crépel, Richard J. Fletcher, and Martin W. Zwierlein. Crystallization of bosonic quantum hall states in a rotating quantum gas. *Nature*, 601(7891):58–62, 2022.

[74] Hale F. Trotter. On the product of semi-groups of operators. *Proceedings of the American Mathematical Society*, 10(4):545–551, 1959.

[75] Masuo Suzuki. Generalized trotter's formula and systematic approximants of exponential operators and inner derivations with applications to many-body problems. *Communications in Mathematical Physics*, 51:183–190, 1976.

[76] Gilbert Strang. On the construction and comparison of difference schemes. *SIAM Journal on Numerical Analysis*, 5(3):506–517, 1968.

[77] Haruo Yoshida. Construction of higher order symplectic integrators. *Physics Letters A*, 150(5–7):262–268, 1990.

[78] Masuo Suzuki. General decomposition theory of ordered exponentials. *Proceedings of the Japan Academy, Series B*, 69(7):161–166, 1993.

[79] Karina Jiménez-García. *Artificial Gauge Fields for Ultracold Neutral Atoms*. Ph.d. dissertation, Joint Quantum Institute, NIST and University of Maryland, 2012.

[80] Lauren Moïse Aycock. *Topological Excitations in an Atomic Bose Gas and Sexual Harassment Reported by Undergraduate Physicists*. Ph.d. dissertation, Cornell University, 2016.

[81] Dina Genkina. *Measuring Topology of BECs in a Synthetic Dimensional Optical Lattice*. Ph.d. dissertation, University of Maryland, College Park, 2019.

[82] Graham Reid. *Topology from Quantum Dynamics of Ultracold Atoms*. Ph.d. dissertation, University of Maryland, College Park, 2023.

[83] Harold J. Metcalf and Peter van der Straten. Laser cooling and trapping of atoms. *Journal of the Optical Society of America B*, 20(5):887–908, 2003.

[84] William D. Phillips and Harold J. Metcalf. Laser deceleration of an atomic beam. *Phys. Rev. Lett.*, 48:596, 1982.

[85] Jean Dalibard and Claude Cohen-Tannoudji. Laser cooling below the doppler limit by polarization gradients: simple theoretical models. *J. Opt. Soc. Am. B*, 6(11):2023–2025, 1989.

[86] E. L. Raab, M. Prentiss, A. Cable, S. Chu, and D. E. Pritchard. Trapping of neutral sodium atoms with radiation pressure. *Phys. Rev. Lett.*, 59:2631, January 1987.

[87] Philip Thomas Starkey, Christopher James Billington, Shaun Phillip Johnstone, Martijn Jasperse, K. Helmerson, Lincoln David Turner, and Russell Paul Anderson. A scripted control system for autonomous hardware-timed experiments. *Review of Scientific Instruments*, 84(8):085111, 2013.

[88] A. R. Fritsch, Mingwu Lu, G. H. Reid, A. M. Piñeiro, and I. B. Spielman. Creating solitons with controllable and near-zero velocity in bose-einstein condensates. *Phys. Rev. A*, 101:053629, May 2020.

[89] G. H. Reid, Mingwu Lu, A. R. Fritsch, A. M. Piñeiro, and I. B. Spielman. Dynamically induced symmetry breaking and out-of-equilibrium topology in a 1d quantum system. *Phys. Rev. Lett.*, 129:123202, Sep 2022.

[90] H.-I. Lu, M. Schemmer, L. M. Aycock, D. Genkina, S. Sugawa, and I. B. Spielman. Geometrical pumping with a bose-einstein condensate. *Physical Review Letters*, 116(20):200402, 2016.

[91] Dina Genkina, Lauren M Aycock, Hui-I Lu, Mingwu Lu, Alina M Pineiro, and Ian B Spielman. Imaging topology of hofstadter ribbons. *New Journal of Physics*, 21(5):053021, 2019.

[92] Q.-Y. Liang, D. Trypogeorgos, A. Valdés-Curiel, J. Tao, M. Zhao, and I. B. Spielman. Coherence and decoherence in the harper-hofstadter model. *Physical Review Research*, 3(2):023058, 2021.

[93] R. P. Anderson, D. Trypogeorgos, A. Valdés-Curiel, Q.-Y. Liang, J. Tao, M. Zhao, T. Andrijauskas, G. Juzeliūnas, and I. B. Spielman. Realization of a deeply subwavelength adiabatic optical lattice. *Physical Review Research*, 2(1):013149, February 2020.

[94] A. Valdés-Curiel, D. Trypogeorgos, Q.-Y. Liang, R. P. Anderson, and I. B. Spielman. Topological features without a lattice in Rashba spin-orbit coupled atoms. 12(1):593, January 2021.

[95] Y. J. Lin, R. L. Compton, K. Jiménez-García, J. V. Porto, and I. B. Spielman. Synthetic magnetic fields for ultracold neutral atoms. *Nature*, 462(7273):628–632, 2009.

[96] Y-J. Lin, R. L. Compton, K. Jiménez-García, W. D. Phillips, J. V. Porto, and I. B. Spielman. A synthetic electric force acting on neutral atoms. *Nature Physics*, 7(7):531–534, 2011.

[97] L. J. LeBlanc, M. C. Beeler, K. Jiménez-García, A. R. Perry, S. Sugawa, R. A. Williams, and I. B. Spielman. Direct observation of zitterbewegung in a bose–einstein condensate. *New Journal of Physics*, 15:073011, 2013.

[98] E. Gvozdiovas A. M. Piñeiro W. D. Phillips Q. Zhou I.B. Spielman E.D. Mercado-Gutierrez, W. Xu. Near-perfect absorption in a non-hermitian synthetic lattice. *Under Preparation*, 2026.

[99] Ana Valdés Curiel. *Topological Dispersion Relations in Spin-Orbit Coupled Bose Gases*. Ph.d. dissertation, University of Maryland, College Park, 2019.

[100] Q.-Y. Liang E. D. Mercado-Gutierrez A. M. Piñeiro J. Tao D. Trypogeorgos M. Zhao I.B. Spielman E. Gvozdiovas, A. Valdés-Curiel. In situ magnetic field stabilization in quantum gas experiments. *Review of Scientific Instruments*, 2026.

[101] A. Putra, D. L. Campbell, R. M. Price, S. De, and I. B. Spielman. Optimally focused cold atom systems obtained using density-density correlations. *Review of Scientific Instruments*, 85(1):013110, 2014.

[102] E. Altuntas and I. B. Spielman. Self-bayesian aberration removal via constraints for ultracold atom microscopy. *Physical Review Research*, 3(4):043087, 2021.

[103] E.G. Loewen and E. Popov. *Diffraction Grating Handbook*. Newport Corporation, 5th edition, 1997.

[104] N. L. Smith. *The tilting mode and two dimensional confinement of a Bose-Einstein condensed gas*. Phd thesis, University of Oxford, 2005.

[105] N. W. Ashcroft and N. D. Mermin. *Solid State Physics*. W. B. Saunders Company, 1976.

[106] G. Grosso and G. P. Parravicini. *Solid State Physics*. Elsevier, 2014.

[107] H. Hellmann and R. P. Feynman. Hellmann–feynman theorem. H. Hellmann, *Einführung in die Quantenchemie* (Franz Deuticke, Leipzig, 1937); R. P. Feynman, Phys. Rev. **56**, 340 (1939).

[108] M. B. Dahan, E. Peik, J. Reichel, Y. Castin, and C. Salomon. Bloch oscillations of atoms in an optical potential. *Physical review letters*, 76:4508, 1996.

[109] Y. B. Ovchinnikov, J. H. Muller, M. R. Doery, E. J. D. Vredenbregt, K. Helmerson, S. L. Rolston, and W. D. Phillips. Diffraction of a released bose-einstein condensate by a pulsed standing light wave. *Phys. Rev. Lett.*, 83:284–287, 1999.

[110] Maxime Ben Dahan, Ekkehard Peik, Jakob Reichel, Yvan Castin, and Christophe Salomon. Bloch oscillations of atoms in an optical potential. *Phys. Rev. Lett.*, 76:4508–4511, Jun 1996.

[111] M. Greiner, O. Mandel, T. Esslinger, T. W. Hänsch, and I. Bloch. Quantum phase transition from a superfluid to a mott insulator in a gas of ultracold atoms. *Nature*, 415:39–44, 2002.

[112] M. Aidelsburger, M. Atala, M. Lohse, J. T. Barreiro, B. Paredes, and I. Bloch. Realization of the hofstadter hamiltonian with ultracold atoms in optical lattices. *Phys. Rev. Lett.*, 111:185301, 2013.

[113] Stepan S. Bulanov, Timur Zh. Esirkepov, Alexander G. R. Thomas, James K. Koga, and Sergei V. Bulanov. Schwinger limit attainability with extreme power lasers. *Phys. Rev. Lett.*, 105:220407, Nov 2010.

[114] Nikodem Szpak and Ralf Schützhold. Quantum simulator for the schwinger effect with atoms in bichromatic optical lattices. *Phys. Rev. A*, 84:050101, Nov 2011.

[115] N Szpak and Ralf Schützhold. Optical lattice quantum simulator for quantum electrodynamics in strong external fields: spontaneous pair creation and the sauter–schwinger effect. *New Journal of Physics*, 14(3):035001, mar 2012.

[116] V. Kasper, F. Hebenstreit, M.K. Oberthaler, and J. Berges. Schwinger pair production with ultracold atoms. *Physics Letters B*, 760:742 – 746, 2016.

[117] V Kasper, F Hebenstreit, F Jendrzejewski, M K Oberthaler, and J Berges. Implementing quantum electrodynamics with ultracold atomic systems. *New Journal of Physics*, 19(2):023030, 2017.

[118] Danielle Allor, Thomas D. Cohen, and David A. McGady. Schwinger mechanism and graphene. *Phys. Rev. D*, 78:096009, Nov 2008.

[119] Balázs Dóra and Roderich Moessner. Nonlinear electric transport in graphene: Quantum quench dynamics and the schwinger mechanism. *Phys. Rev. B*, 81:165431, Apr 2010.

[120] F. Fillion-Gourdeau and S. MacLean. Time-dependent pair creation and the schwinger mechanism in graphene. *Phys. Rev. B*, 92(3):035401, 2015.

[121] M. I. Katsnelson and G. E. Volovik. Quantum electrodynamics with anisotropic scaling: Heisenberg-euler action and schwinger pair production in the bilayer graphene. *Pis'ma ZhETF*, 95:457–461, 2012.

[122] M. A. Zubkov. Schwinger pair creation in multilayer graphene. *Pis'ma v Zh. Èksper. Teoret. Fiz.*, 95(9):540–543, 2012.

[123] I. Akal, R. Egger, C. Müller, and S. Villalba-Chávez. Low-dimensional approach to pair production in an oscillating electric field: Application to bandgap graphene layers. *Phys. Rev. D*, 93:116006, Jun 2016.

[124] L. Hrivnák. Relativistic analogies in direct-gap semiconductors. *Progress in Quantum Electronics*, 17(3):235 – 271, 1993.

[125] S. A. Smolyansky, A. V. Tarakanov, and M. Bonitz. Vacuum particle creation: Analogy with the bloch theory in solid state physics. *Contrib. Plasma Phys.*, 49:575, 2009.

[126] Malte F. Linder, Axel Lorke, and Ralf Schützhold. Analog sauter-schwinger effect in semiconductors for spacetime-dependent fields. *Phys. Rev. B*, 97:035203, Jan 2018.

[127] L. D. Landau. Zur theorie der energieübertragung. ii. *Physikalische Zeitschrift der Sowjetunion*, 2:46–51, 1932.

[128] C. Zener. Non-adiabatic crossing of energy levels. *Proceedings of the Royal Society of London A: Mathematical, Physical and Engineering Sciences*, 137(833):696–702, 1932.

[129] R. Gerritsma, G. Kirchmair, F. Zahringer, E. Solano, R. Blatt, and C. F. Roos. Quantum simulation of the dirac equation. *Nature*, 463:68–71, 2010.

[130] S. Kling, T. Salger, C. Grossert, and M. Weitz. Atomic bloch-zener oscillations and stückelberg interferometry in optical lattices. *Phys. Rev. Lett.*, 105:215301, 2010.

[131] T. Salger, C. Grossert, S. Kling, and M. Weitz. Klein tunneling of a quasirelativistic bose-einstein condensate in an optical lattice. *Phys. Rev. Lett.*, 107:240401, 2011.

[132] Y-J Lin, AR Perry, RL Compton, IB Spielman, and JV Porto. Rapid production of $\hat{8}$7rb bose-einstein condensates in a combined magnetic and optical potential. *Phys. Rev. B*, 79:063631, 2009.

[133] Gretchen K. Campbell, Jongchul Mun, Micah Boyd, Erik W. Streed, Wolfgang Ketterle, and David E. Pritchard. Parametric amplification of scattered atom pairs. *Phys. Rev. Lett.*, 96:020406, Jan 2006.

[134] A. Kastberg, W. D. Phillips, S. L. Rolston, R. J. C. Spreeuw, and P. S. Jessen. Adiabatic cooling of cesium to 700 nk in an optical lattice. *Phys. Rev. Lett.*, 74:1542–1545, Feb 1995.

[135] Markus Greiner, Immanuel Bloch, Olaf Mandel, Theodor W. Hänsch, and Tilman Esslinger. Exploring phase coherence in a 2d lattice of bose-einstein condensates. *Phys. Rev. Lett.*, 87:160405, Oct 2001.

[136] Michael Köhl, Henning Moritz, Thilo Stöferle, Kenneth Günter, and Tilman Esslinger. Fermionic atoms in a three dimensional optical lattice: Observing fermi surfaces, dynamics, and interactions. *Phys. Rev. Lett.*, 94:080403, Mar 2005.

[137] Immanuel Bloch, Jean Dalibard, and Wilhelm Zwerger. Many-body physics with ultracold gases. *Rev. Mod. Phys.*, 80:885–964, Jul 2008.

[138] Jan R. Rubbmark, Michael M. Kash, Michael G. Littman, and Daniel Kleppner. Dynamical effects at avoided level crossings: A study of the landau-zener effect using rydberg atoms. *Phys. Rev. A*, 23:3107–3117, Jun 1981.

[139] T. Oka and H. Aoki. Ground-state decay rate for the zener breakdown in band and mott insulators. *Phys. Rev. Lett.*, 95:137601, Sep 2005.

[140] Q. Niu and M. G. Raizen. How landau-zener tunneling takes time. *Phys. Rev. Lett.*, 80:3491–3494, 1998.

[141] L. D. Turner. Holographic imaging of cold atoms. *PhD Thesis*, page University of Melbourne, 2004.

[142] L. D. Turner, K. P. Weber, D. Paganin, and R. E. Scholten. Off-resonant defocus- contrast imaging of cold atoms. *Opt. Lett.*, 29(3):232–234, 2004.

[143] A. Putra, D. L. Campbell, R. M. Price, S. De, and I. B. Spielman. Optimally focused cold atom systems obtained using density-density correlations. *Rev. Sci. Instr.*, 85:013110, 2014.

[144] A. R. Bell and J. G. Kirk. Possibility of prolific pair production with high-power lasers. *Phys. Rev. Lett.*, 101:200403, Nov 2008.

[145] Matthias Ruf, Guido R. Mocken, Carsten Müller, Karen Z. Hatsagortsyan, and Christoph H. Keitel. Pair production in laser fields oscillating in space and time. *Phys. Rev. Lett.*, 102:080402, Feb 2009.

[146] J. G. Kirk, A. R. Bell, and I. Arka. Pair production in counter-propagating laser beams. *Plasma Phys. Control. Fusion*, 51:085008, 2009.

[147] W. T. Hill and L. Roso. Probing the quantum vacuum with petawatt lasers. *Journal of Physics: Conference Series*, 869:012015, 2017.

[148] E. A. Martinez, C. A. Muschik, P. Schindler, D. Nigg, A. Erhard, M. Heyl, P. Hauke, M. Dalmonte, T. Monz, P. Zoller, and R. Blatt. Real-time dynamics of lattice gauge theories with a few-qubit quantum computer. *Nature*, 534:516, 2010.

[149] W. P. Su, J. R. Schrieffer, and A. J. Heeger. Solitons in polyacetylene. *Phys. Rev. Lett.*, 42:1698, 1979.

[150] M. J. Rice and E. J. Mele. Elementary excitations of a linearly conjugated diatomic polymer. *Phys. Rev. Lett.*, 49:1455, 1982.

[151] G Juzeliūnas and I.B Spielman. Flux lattices reformulated. *New Journal of Physics*, 14(12):123022, 2012.

[152] J. Sebby-Strabley, B. L. Brown, M. Anderlini, P. J. Lee, W. D. Phillips, J. V. Porto, and P. R. Johnson. Preparing and probing atomic number states with an atom interferometer. *Phys. Rev. Lett.*, 98:200405, May 2007.

[153] S. Trotzky, P. Cheinet, S. Fölling, M. Feld, U. Schnorrberger, A. M. Rey, A. Polkovnikov, E. A. Demler, M. D. Lukin, and I. Bloch. Time-resolved observation and control of superexchange interactions with ultracold atoms in optical lattices. *Science*, 319(5861):295–299, 2008.

[154] R. C. Brown, R. Wyllie, S. B. Koller, E. A. Goldschmidt, M. Foss-Feig, and J. V. Porto. Two-dimensional superexchange-mediated magnetization dynamics in an optical lattice. *Science*, 348(6234):540–544, 2015.

[155] Jan Carl Budich, Ying Hu, and Peter Zoller. Helical floquet channels in 1d lattices. *Phys. Rev. Lett.*, 118(10):105302, 2017.

[156] J. Dalibard, F. Gerbier, G. Juzeliūnas, and P. Öhberg. Colloquium: Artificial gauge potentials for neutral atoms. *Reviews of Modern Physics*, 83(4):1523–1543, 2011.

[157] N. Goldman and J. Dalibard. Periodically driven quantum systems: Effective hamiltonians and engineered gauge fields. *Phys. Rev. X*, 4:031027, 2014.

[158] N. R. Cooper. Rapidly rotating atomic gases. *Advances in Physics*, 57(6):539–616, 2008.

[159] A. L. Fetter. Rotating trapped bose–einstein condensates. *Reviews of Modern Physics*, 81(2):647–691, 2009.

[160] M. R. Matthews, B. P. Anderson, P. C. Haljan, D. S. Hall, C. E. Wieman, and E. A. Cornell. Vortices in a bose-einstein condensate. *Physical Review Letters*, 83(13):2498–2501, 1999.

[161] K. W. Madison, F. Chevy, W. Wohlleben, and J. Dalibard. Vortex formation in a stirred bose-einstein condensate. *Physical Review Letters*, 84(5):806–809, 2000.

[162] J. R. Abo-Shaeer, C. Raman, J. M. Vogels, and W. Ketterle. Observation of vortex lattices in bose-einstein condensates. *Science*, 292(5516):476–479, 2001.

[163] Y.-J. Lin, R. L. Compton, A. R. Perry, W. D. Phillips, J. V. Porto, and I. B. Spielman. Bose-einstein condensate in a uniform light-induced vector potential. *Phys. Rev. Lett.*, 102:130401, Mar 2009.

[164] Y. Aharonov and D. Bohm. Significance of electromagnetic potentials in the quantum theory. *Physical Review*, 115(3):485–491, 1959.

[165] Monika Aidelsburger, Marcos Atala, Sylvain Nascimbène, Stefan Trotzky, Yu-Ao Chen, and Immanuel Bloch. Experimental realization of strong effective magnetic fields in an optical lattice. *Physical Review Letters*, 107(25):255301, 2011.

[166] K. Jiménez-García, L. J. LeBlanc, R. A. Williams, M. C. Beeler, A. R. Perry, and I. B. Spielman. The peierls substitution in an engineered lattice potential. *Physical Review Letters*, 108(22):225303, 2012.

[167] J. Struck, C. Ölschläger, M. Weinberg, P. Hauke, J. Simonet, A. Eckardt, M. Lewenstein, K. Sengstock, and P. Windpassinger. Tunable gauge potential for neutral and spinless particles in driven optical lattices. *Physical Review Letters*, 108(22):225304, 2012.

[168] Monika Aidelsburger, Marcos Atala, Michael Lohse, Julio T Barreiro, Belén Paredes, and Immanuel Bloch. Realization of the hofstadter hamiltonian with ultracold atoms in optical lattices. *Physical Review Letters*, 111(18):185301, 2013.

[169] Benjamin K Stuhl, Hui-I Lu, Lauren M Aycock, Dajana Genkina, and Ian B Spielman. Visualizing edge states with an atomic bose gas in the quantum hall regime. *Science*, 349(6255):1514–1518, 2015.

[170] Anatoly A. Svidzinsky and Alexander L. Fetter. Stability of a vortex in a trapped bose-einstein condensate. *Phys. Rev. Lett.*, 84:5919–5923, Jun 2000.

[171] Alexander L. Fetter. Rotating trapped bose-einstein condensates. *Rev. Mod. Phys.*, 81:647–691, May 2009.

[172] L. B. Taylor, R. M. W. van Bijnen, D. H. J. O'Dell, N. G. Parker, S. J. J. M. F. Kokkelmans, and A. M. Martin. Synthetic magnetohydrodynamics in bose-einstein condensates and routes to vortex nucleation. *Phys. Rev. A*, 84:021604, Aug 2011.

[173] P. W. Anderson. Absence of diffusion in certain random lattices. *Physical Review*, 109(5):1492–1505, 1958.

[174] P. W. Anderson, D. J. Thouless, E. Abrahams, and D. S. Fisher. New method for a scaling theory of localization. *Physical Review Letters*, 42:673–676, 1979.

[175] G. Roati, C. D'Errico, L. Fallani, M. Fattori, C. Fort, M. Zaccanti, G. Modugno, M. Modugno, and M. Inguscio. Anderson localization of a non-interacting bose–einstein condensate. *Nature*, 453:895–898, 2008.

[176] J. Billy, V. Josse, Z. Zuo, A. Bernard, B. Hambrecht, P. Lugan, D. Clément, L. Sanchez-Palencia, P. Bouyer, and A. Aspect. Direct observation of anderson localization of matter waves in a controlled disorder. *Nature*, 453:891–894, 2008.

[177] B. L. Altshuler, A. G. Aronov, and P. A. Lee. Interaction effects in disordered fermi systems in two dimensions. *Physical Review B*, 22(11):5142–5159, 1980.

[178] S. Hikami, A. I. Larkin, and Y. Nagaoka. Spin-orbit interaction and magnetoresistance in the two dimensional random system. *Progress of Theoretical Physics*, 63(2):707–710, 1980.

[179] Y. Aharonov and D. Bohm. Significance of electromagnetic potentials in the quantum theory. *Physical Review*, 115(3):485–491, 1959.

[180] V. Galitski. Magnetoresistance in two-dimensional electron systems. *Physical Review B*, 72(21):214201, 2005.

[181] A. A. Abrikosov. Electron scattering on magnetic impurities in metals and anomalous resistivity effects. *Physics*, 2(1):5–20, 1965. Received 17 February 1965.

[182] I. B. Spielman. Raman processes and effective gauge potentials. *Phys. Rev. A*, 79:063613, Jun 2009.